



저작자표시-비영리-변경금지 2.0 대한민국

이용자는 아래의 조건을 따르는 경우에 한하여 자유롭게

- 이 저작물을 복제, 배포, 전송, 전시, 공연 및 방송할 수 있습니다.

다음과 같은 조건을 따라야 합니다:



저작자표시. 귀하는 원저작자를 표시하여야 합니다.



비영리. 귀하는 이 저작물을 영리 목적으로 이용할 수 없습니다.



변경금지. 귀하는 이 저작물을 개작, 변형 또는 가공할 수 없습니다.

- 귀하는, 이 저작물의 재이용이나 배포의 경우, 이 저작물에 적용된 이용허락조건을 명확하게 나타내어야 합니다.
- 저작권자로부터 별도의 허가를 받으면 이러한 조건들은 적용되지 않습니다.

저작권법에 따른 이용자의 권리는 위의 내용에 의하여 영향을 받지 않습니다.

이것은 [이용허락규약\(Legal Code\)](#)을 이해하기 쉽게 요약한 것입니다.

[Disclaimer](#)

이학박사 학위논문

**Field-Driven Domain-Wall Dynamics Related  
with Dzyaloshinskii-Moriya Interactions and  
Magnetic Bubblecade Memory**

드잘로신스키 모리아 상호작용 현상과 관련된 자기장  
인가 자구벽 동역학과 자기 버블케이드 메모리

2016년 2월

서울대학교 대학원

물리천문학부

김 덕 호

**Field-Driven Domain-Wall Dynamics Related  
with Dzyaloshinskii-Moriya Interactions and  
Magnetic Bubblecade Memory**

**Duck-Ho Kim**

Supervised by  
**Professor Sug-Bong Choe**

A Dissertation in Physics

Submitted to the Faculties of  
Seoul National University  
in Partial Fulfillment of the Requirements for the Degree of  
Doctor of Philosophy

February 2016

*Department of Physics and Astronomy  
College of Natural Sciences  
Seoul National University*

# Abstract

For application as a data storage entitled to magnetic hard disk drives, the magnetic domains are widely used. Each domain represents unit of stored information, and the region between domains is known as domain walls (DWs). For the promising memory and logic devices, it has been proposed to shift the information by coherent moving these DWs through a magnetic nanowire, called racetrack memory. This concept has led to the establishment of a quickly evolving new research field which investigates the mechanisms moving the DWs. This mechanism is operated by the use of an externally applied magnetic field, or injecting an electric currents through the nanowire in which the DWs reside. Recently, perpendicularly magnetized anisotropy (PMA) materials are not only particularly interesting for these applicational devices, but also new physics is being found in these materials since finding DW motion driven by spin-orbit-torque and chiral DW by the Dzyaloshinskii-Moriya interaction (DMI).

This thesis contains several contributions which are right at the heart of recent developments on DW physics in PMA materials such as Pt/Co/Pt. The first part of the thesis focuses on maximizing the motion of DWs by adjustment of thickness of metal (upper and bottom Pt layers) contacted by magnetic layer. In particular, it is shown that by changing the each Pt thickness, the PMA is altered in such a way that DW speed is affected. This phenomena is successfully explained by the creep law with scaling law between PMA and DW speed. So this results offer a method of maximizing the DW speed without changing the thickness of the magnetic Co layer.

In the second part of the thesis, it deals with topic of fast DW motion

called, the flow regime. This regime has been widely studied since 1950. All of the study have been performed the relation between DW speed and driving force (applied external field). In this thesis, main topic is the DW speed with respect to in-plane magnetic field (changing the DW energy related DW profile) with fixed out-of-plane magnetic field (driving force). Based on the 1-dimensional model, analytic solution is suggested and the result from analytic solution is well-satisfied with micromagnetic simulation. Furthermore, this analytic result is well-explaining experimental result, qualitatively: variation of the speed. Important point is the minimum speed at compensating the field induced by DMI, and so it can be quantitatively determined the DMI-induced field.

The third part suggests new technique to measure the DMI. This is advanced technique to overcome such field-strength limit. The core idea is to utilize the dependence of minimum speed on the tilting angle of the DWs with respect to the direction of the in-plane magnetic field. The present idea can be also demonstrated to other lms (Pt/Co/AlOx and Pt/Co/MgO), where DMI induced field is even much larger than the field-strength limit of equipment, and thus enables the development of an advanced DMI meter based on asymmetric DW motion.

The final part of the thesis is composed of application device by use of magnetic-field oscillation. For this application, unidirectional motion of magnetic DWs is the key concept underlying next-generation DW-mediated memory and logic devices. In this part, new scheme is suggested and it utilizes the recently discovered chiral DWs, which exhibit asymmetry in their speed with respect to magnetic fields. Because of this asymmetry, an alternating magnetic field results in the coherent motion of the DWs in one direction. Such coherent unidirectional motion is achieved even for an array of magnetic bubble domains, enabling the design of a new device prototype—magnetic bubblecade memory—with two-dimensional data-storage capability. And then the study about

the optimization of magnetic bubblecade speed is performed. In the operation of the magnetic bubblecade memory, two major control factors were found to play the decisive role in determination of the bubblecade speed strength and tilting angle of the magnetic field. Here, the relation of bubble speed with respect to strength and tilting angle of the magnetic field and obtain the analytic solution from the creep scaling law is examined. The proposed analytic equation thus offers the way to predict the optimization condition for the maximum bubblecade speed in the operation of the magnetic bubblecade memory.

**Keywords:** Domain Wall, Dzyaloshinskii-Moriya Interaction, Flow regime, Creep regime, Magneto-Optical Kerr Effect Microscope

**Student Number:** 2011-30121

# Contents

<b>Abstract</b>	<b>i</b>
<b>Chapter 1 Introduction</b>	<b>1</b>
1.1 Energy . . . . .	1
1.1.1 Magnetostatic Energy . . . . .	2
1.1.2 Exchange Energy . . . . .	3
1.1.3 Anisotropy Energy . . . . .	4
1.1.4 Zeeman Energy . . . . .	6
1.2 Types of the Domain Wall: Bloch and Néel Walls . . . . .	6
1.3 Dzyaloshinskii-Moriya Interaction and Chiral Domain Wall . . . . .	7
<b>Chapter 2 DW Dynamics in Creep regime</b>	<b>11</b>
2.1 Maximizing DW Speed via Magnetic Anisotropy Adjustment in Pt/Co/Pt Films . . . . .	11
2.1.1 Introduction . . . . .	12
2.1.2 Sample Preparation & Experimental Methods . . . . .	12
2.1.3 Result.1: Large Enhancement of the DW Speed by 50 Times	14
2.1.4 Result.2: DW Speed & Creep Scaling Constant in Pt/Co/Pt Films . . . . .	15

2.1.5	Analysis & Discussion & Conslusions . . . . .	16
<b>Chapter 3</b>	<b>DW Dynamics &amp; Asymmetric DW Motion in Flow Regime</b>	<b>20</b>
3.1	Broken chirality governing asymmetric domain-wall motion in the flow regime . . . . .	21
3.1.1	Steadt-State Flow & Walker Breakdown . . . . .	22
3.1.2	Precession Flow . . . . .	24
3.1.3	Numerical Calculation . . . . .	26
3.1.4	Micromagnetic Simulation . . . . .	26
3.1.5	Comparision between Experimental Result and Analytic solution . . . . .	27
3.1.6	Conclusion . . . . .	29
3.2	Universality of Chiral-Domain-Wall Motion by the Dzyaloshinskii-Moriya Interaction in the Creep and Flow Regimes . . . . .	30
<b>Chapter 4</b>	<b>DMI meter 2.0</b>	<b>33</b>
4.1	DMI meter 1.0: Asymmetric Magnetic Domain-Wall Motion by the Dzyaloshinskii-Moriya Interaction . . . . .	33
4.2	DMI meter 2.0: Measuring the Dzyaloshinskii-Moriya Interaction based on Angular Dependence of Asymmetric Magnetic DW Motion . . . . .	34
4.2.1	Result.1: Angular Dependence of Asymmetric Magnetic DW Motion in Pt/Co/Pt . . . . .	34
4.2.2	Result.2 Angular Dependence of Asymmetric Magnetic DW Motion in Pt/Co/Pt, Pt/Co/AlOx, and Pt/Co/MgO . . . . .	35
<b>Chapter 5</b>	<b>Applicaiton Device: Magnetic Bubblecade Memory</b>	<b>38</b>

5.1	Magnetic Bubblecade Memory based on Chiral Domain Walls . . .	38
5.1.1	Introduction . . . . .	39
5.1.2	Sample Preparation & Experimental Methods . . . . .	40
5.1.3	Result.1: Single Bubble Motion . . . . .	42
5.1.4	Result.2: Speed of Bubble Motion . . . . .	44
5.1.5	Result.3: Bubble Radius Variation . . . . .	46
5.1.6	Result.4: Bubblecade and Memory Operation . . . . .	47
5.1.7	Discussion & Conclusions . . . . .	49
5.2	Magnetic Bubblecade Motion in Creep Regime . . . . .	50
5.3	Optimization of Magnetic Bubblecade Speed via Strength and Angle of Magnetic Field Adjustments . . . . .	55
 <b>Chapter 6 Temperature Dependence of DW Motion in Creep Regime</b>		 <b>58</b>
6.1	A Method for Compensating the Joule-Heating Effects in Current- Induced Domain Wall Motion . . . . .	58
6.1.1	Introduction . . . . .	59
6.1.2	Sample Preparation & Experimental Methods . . . . .	60
6.1.3	Results & Discussion . . . . .	63
6.1.4	Conclusions . . . . .	67
 <b>Chapter 7 Other Works</b>		 <b>68</b>
7.1	Distinct Universality Classes of DomainWall Roughness in Two- Dimensional Pt/Co/Pt Films . . . . .	68
7.2	Determination of Magnetic Domain-Wall Types Using Dzyaloshin- skii– Moriya-Interaction-Induced Domain Patterns . . . . .	70
 <b>References</b>		 <b>71</b>

<b>Author's Biography</b>	<b>78</b>
<b>Awards</b>	<b>80</b>
<b>Publication Lists (SCI &amp; SCIE)</b>	<b>82</b>
<b>Presentation Lists (International Conferences)</b>	<b>85</b>
<b>Presentation Lists (Domestic Conferences)</b>	<b>92</b>
<b>초록</b>	<b>99</b>
<b>Acknowledgements</b>	<b>102</b>

# List of Figures

Figure 1.1	DMI from symmetry arguments. (a) In a symmetric system, a left-handed spin configuration (top) can be transformed to a right-handed configuration without changing the energy. (b) Applying the same transformations to a system including a symmetry-breaking third ion, it is not possible to transform the handedness without changing the relative position of this ion, hence the energy can depend on the chirality. . . . .	9
Figure 2.1	(a) Schematic layer structure of the samples. (b) Image of the expansion of circular domains under an external magnetic field (3.5 mT). This image was obtained by combining several domain images that were captured sequentially with a constant time step (350 ms) using a MOKE microscope. . . . .	13
Figure 2.2	Measured $v$ with respect to $H$ for Sample I ( $t_d=1.5$ nm and $t_u=2.5$ nm) and Sample II ( $t_d=2.5$ nm and $t_u=1.5$ nm). . . . .	15

Figure 2.3	Creep-scaling plot of $v$ with respect to $H^{-1/4}$ for several samples with different values of $t_d$ and $t_u$ as denoted in the figure. The solid lines represent the best fits using Eq. (2.1). . . . .	17
Figure 2.4	Correlation plot of $a$ with respect to $K$ . All values of $\alpha$ and $K$ are identical to those presented in Tables I and II. The dashed lines represent the proportionality given by Eq. (2.2). . . . .	19
Figure 3.1	Analytic result: Domain wall speed with respect to the $H_z$ for various $H_x$ . . . . .	27
Figure 3.2	Micromagnetic Simulation: Domain wall speed (a) with respect to the $H_z$ for various $H_x$ and (b) with respect to the $H_x$ at fixed $H_z=50$ mT . . . . .	28
Figure 3.3	(a) Measured domain wall speed with respect to the $H_x$ at fixed $H_z=51$ mT and (b) Normalized domain wall speed both experimental result and analytic result . . . .	28
Figure 3.4	DW speed $v$ with respect to the in-plane magnetic field $H_x$ at fixed out-of-plane magnetic field (a) $H_z=1.7$ mT for creep and (b) 51 mT for flow. . . . .	31
Figure 3.5	(a) Difference between DW speeds $v$ with respect to the in-plane magnetic field $H_x$ (b) DW speed $v$ with respect to the in-plane magnetic field $H_x$ at fixed out-of-plane magnetic field $H_z= 51$ mT for flow. . . . .	32

Figure 4.1	(a) the DW displacements for each $\theta$ . (b) Speed $v_{\perp}$ normal to the DW with respect to the in-plane magnetic field $H_x$ for various DW tilting angle $\theta$ ( $0^\circ$ , $30^\circ$ , $60^\circ$ , and $90^\circ$ ). The red lines are the best fit with the equation in Ref. 5 and the blue arrows indicate $H_{shift}$ . The strength of the out-of-plane magnetic field $H_z$ is 8 mT. . . . .	35
Figure 4.2	Measured $H_{shift}$ with respect to $\theta$ . The red line is the best fit with $\cos\theta$ . . . . .	36
Figure 4.3	Measured $H_{shift}$ with respect to $\theta$ (a) Pt/Co/Pt, (b) Pt/Co/AlOx, and (c) Pt/Co/MgO. The red lines are the best fit with $\cos\theta$ . . . . .	37
Figure 5.1	Schematic descriptions of the unidirectional bubble motion. (a) Illustration of a bubble domain (bright circle) and the DW (grey ring), surrounded by a domain of opposite magnetization (dark area). The red symbols and arrows indicate the direction of the magnetization inside the DW and domains. (b) Asymmetric DW-energy distribution under an in-plane magnetic field $+H_x$ (green arrow), as visualized by the color contrast of the arrows on the DW according to the scale bar at the bottom. (c) Asymmetric DW expansion under a magnetic field $H(= (+H_x, +H_z))$ with a tilting angle $\theta$ . (d) Asymmetric DW-energy distribution under the reversed in-plane magnetic field $-H_x$ . (e) Asymmetric DW shrinkage under the reversed magnetic field $(-H_x, -H_z)$ . The dashed circles represent the previous DW positions. . . . .	43

Figure 5.2 Experimental verification of the unidirectional bubble motion from Pt/Co/Pt film. (a) MOKE image of the initial bubble domain (bright circle) surrounded by a domain of opposite magnetization (dark area). The red symbols indicate the direction of the magnetization in the domains. The inset illustrates the expected  $\hat{m}_{DW}$  (red arrows) in the right-handed chiral DW configuration. (b) The expanded bubble domain after application of a  $(+H_x, +H_z)$  pulse ( $H_x=30$  mT,  $H_z=4$  mT,  $\Delta t=100$  ms), where  $\Delta t$  is the pulse duration time. The blue arrow indicates the DW displacement  $V_{\parallel}(H_z, H_x)\Delta t$ . The dashed circle represents the initial DW position. (c) The shrunken bubble domain after application of a  $(-H_x, -H_z)$  pulse. The blue arrow indicates the DW displacement  $V_{\parallel}(-H_z, -H_x)\Delta t$ . The dashed circles represent the previous DW positions. (d) Measured  $V_B$  with respect to  $H_x$  for several  $H_z$ . The error bars correspond to the standard deviation from data obtained by sampling 10 times. 45

Figure 5.3 Frequency dependence of bubble motions. Accumulated MOKE images acquired during bubble motion for various  $f$  values, 10 Hz (a), 20 Hz (b), and 50 Hz (c), respectively. Alternating sinusoidal magnetic field was applied with an amplitude 3.7 mT and a tilting angle  $34^\circ$ , and the accumulation time was fixed to 3 s for all images. The red (blue) circle represents the smallest (largest) bubble observed during the motion. The blue arrows indicate  $\Delta r_B$  between the largest and smallest bubbles. The red arrows indicate the displacement of the bubble center between the initial and final positions (white dashed circles) over the accumulation time.  $\tilde{V}_B$  is then determined by the ratio of the displacement over the accumulation time. Since these images were captured over the same accumulation time, almost the same displacements indicate that  $\tilde{V}_B$  nearly unchanged irrespective of  $f$ . (d), Measured  $\Delta r_B$  and  $\tilde{V}_B$  values with respect to  $f$ . The error bars correspond to the standard deviation from data obtained by sampling 10 times. . . . . 46

Figure 5.4 Experimental demonstration of ‘bubblecade’, the two-dimensional coherent unidirectional motion of multiple bubbles. MOKE images of an arbitrary  $5 \times 5$  array of bubbles, (a) initially written on the leftmost side of the film and taken after application of (b) 32, (c) 64, (d) 96, and (e) 127 pulse sets. Each pulse set is composed of alternating square magnetic field pulses ( $H = \pm 106$  mT,  $\theta = 71^\circ$ ,  $\Delta t = 20$  ms). (f) The operation timetable of 4-bit magnetic bubblecade memory. The top panel presents the alternating magnetic field pulses ( $H = \pm 106$  mT,  $\theta = 71^\circ$ ,  $\Delta t = 20$  ms) that act as the operation clock. The next four panels show the pulses for the thermomagnetic writing of the bubbles on each bit in the writing section. The last four panels show the signals from the CCD pixels corresponding to each bit of the reading section. The inset presents the device structure, with the writing (blue box) and reading (red box) sections indicated. . . . 48

Figure 5.5  $V_B$  in Pt/Co/MgO film, with respect to  $H_x$  for several  $H_z$ . The inset illustrates the expected  $\hat{m}_{DW}$  (red arrows) with the left-handed chiral DW configuration. The dashed lines show the best linear fit from Eq. (S9). . . 53

Figure 5.6	Asymmetric DW speed $V_{\parallel}$ with respect to $H_x$ for several $H_z$ . Data were obtained under the same condition employed to measure Fig. 2d. The asymmetry with respect to $H_x$ is known to be caused by a finite DMI[25,26]. For the condition (with $H_z=68$ mT and $H_x= 40$ mT) of the maximum $V_B$ shown in Fig. 2d, the forward and backward DW speeds are measured as $V_{\parallel}(H_z, H_x)= 3.7$ m/s and $V_{\parallel}(-H_z, -H_x)=-V_{\parallel}(H_z, -H_x)=-1.6$ m/s. These speeds are accordant to the measured maximum $V_B(=1$ m/s) in Fig. 2d via the relation $V_B = [V_{\parallel}(H_z, H_x) + V_{\parallel}(-H_z, -H_x)]/2$ . This maximum $V_B$ is approximately 46% of $V_{\parallel}(H_z, 0)(=2.2$ m/s). . . . .	54
Figure 5.7	Bubble speed $v$ with respect to the tilting angle of the magnetic field $\theta$ for various field strength $H$ . . . . .	56
Figure 5.8	2 dimensional Bubble speed $v$ with respect to the tilting angle of the magnetic field $\theta$ and field strength $H_{ext}$ . . . . .	57
Figure 6.1	Sequential images of the DW motion measured by the MOKE microscope with a constant time step (700 ms). The directions of the current density $J$ , the magnetic field $H$ , and the magnetization $M$ are denoted in the inset. . . . .	61
Figure 6.2	(a) Normalized resistivity $\rho/\rho_0$ with respect to $J$ for the 5- m-wide wire. The solid line is the best quadratic fit. (b) Normalized resistivity $\rho/\rho_0$ with respect to the temperature $\Delta T$ measured in a cryostat. The solid line is the best linear fit. . . . .	62

Figure 6.3 (a)  $v$  vs.  $H^{-1/4}$  at different temperatures as denoted in the figure. (b)  $\alpha$  with respect to  $T$ . (c)  $v_0$  with respect to  $T$ . Note that  $\alpha$  and  $v_0$  are obtained by the best linear fit for the data shown in (a) based on (1). (d) with respect to  $H^{-1/4}$ . All at different collapses onto a single universal curve. The solid line shows the best linear fit for all the data. . . . . 64

Figure 6.4 (a) Universal curve of the virtual speed  $v^*$  with respect to  $(H^*)^{-1/4}$  at all various  $J$  as denoted in the figure. For comparison, the raw data  $v$  (b), the normalized speed  $v^\dagger$  based on the Arrhenius law (c), and the virtual speed  $v^*$  based on the present method (d) are plotted with respect to  $(H^*)^{-1/4}$ . . . . . 66

# List of Tables

Table 2.1	PMA constant $K$ of the Si/SiO <sub>2</sub> /5.0-nm Ta/ $t_d$ Pt/0.3-nm Co/ $t_u$ Pt films with different $t_d$ and $t_u$ . . . . .	14
Table 2.2	Creep scaling constant $\alpha$ of the Si/SiO <sub>2</sub> /5.0-nm Ta/ $t_d$ Pt/0.3-nm Co/ $t_u$ Pt films with different $t_d$ and $t_u$ . . . . .	18

# Chapter 1

## Introduction

In this chapter, basic notions about the energy by use of formation of the domain and domain wall are described. At first, part of the energy is composed of magnetostatic energy, exchange energy, anisotropy energy (cubic, volume, surface, and interface anisotropies), and Zeeman energy. Second part, introduction of types of the domain wall is described, Bloch and Neel Walls. At the end of this chapter, the Dzyaloshinskii–Moriya interaction is explained, which is another exchange interaction forming the chiral system. Throughout, SI units are used.

### 1.1 Energy

In ferromagnetic materials, magnetic domains are formed in order to minimize the sum of energy terms, such as the magnetostatic, the exchange, the anisotropy, and the Zeeman energies. For example, the ferromagnetic film has infinite lateral extension, which is aligned uniform magnetization in the film

plane, the magnetostatic energy is zero. If the film has a finite size, however, the surface charging has to be taken into account, which leads to a demagnetizing field. Due to the demagnetizing field, the film is separated into domains with different orientations of magnetization (different area) to reduce the magnetostatic energy which is long range magnetic interaction. It naturally creates the boundary between these domains, and it is called the magnetic domain wall (DW). Inside the wall, the magnetizations, spins, are gradually rotated, and leads to a certain width of the DW. the DW width is mainly determined by the competition between two energy terms, the exchange energy and the anisotropy energy. The role of the exchange energy between neighboring spins is to increase the wall width. It is natural from the its physical origin. This means that a larger rotation of spins between two neighbors causes a higher exchange energy. However, when the DW width is a wider, it induces a higher anisotropy energy, because inside the DW the direction of magnetization is away from the easy axis of magnetization. Therefore these two energies lead to short range interactions, order of nm range.

### 1.1.1 Magnetostatic Energy

The magnetostatic energy is magnetic dipole energy, and it depends on the magnetization  $M$ , which is the magnetic-dipole moment per volume, arising from the alignment of atomic magnetic dipoles. The dipoles arise primarily from electron spins in a solid. Although the orbital motion of electrons is usually less contribution to the dipole strength, it plays a important role for the magnetic anisotropy.

The magnetic domains is formed as a consequence of energy minimization [1]. A single domain with finite specimen has associated with it a large magnetostatic energy. The breakup of the magnetization into localized regions (domains)

can reduce the magnetostatic energy. If the decrease in magnetostatic energy is greater than the energy needed to form magnetic domain walls, then multi-domain specimens will arise. For example, it is the case of an infinitely extended magnetic film with uniform magnetization along the normal to the surface, for which the magnetostatic energy can be easily derived. The magnetic dipoles in the film,  $\vec{M}$ , can create the stray field,  $\vec{H}_{stray}$ . However, due to the surface charging, there exists the field which has the same amplitude as  $\vec{H}_{stray}$  inside the film, but directs opposite to  $\vec{M}$ , the so called demagnetizing field,  $H_d$ . So the magnetostatic energy, which has the same amplitude to the demagnetizing energy in this case, will be described with  $\vec{M}$  and  $\vec{H}_d$  as

$$K_d = -\mu_0 \int_V \vec{M} \cdot \vec{H}_d dV = -\mu_0 \int_V \vec{M} \cdot \frac{\vec{H}}{2} dV = \mu_0 M_S^2 \quad (1.1)$$

, where  $\vec{M}$  is exchanged to the saturation magnetization,  $M_S$ , and  $\vec{H}$  is a sum of  $H_{stray}$  and  $H_d$ , will have the same field as  $M_S$ .

### 1.1.2 Exchange Energy

The energy related with cooperative magnetic ordering is the exchange interaction. The exchange interaction energy,  $E_{ex}$ , between two spins,  $S_i$  and  $S_j$ , scales with the exchange integral,  $J$  (dimension; J),

$$E_{ex} = - \sum_{i,j} J_{i,j} \vec{S}_i \cdot \vec{S}_j \quad (1.2)$$

where  $\vec{S}_i$  and  $\vec{S}_j$  are the unit vectors of interacting spins on two atoms. The exchange interaction is a manifestation of the Coulomb interaction between electron charges and the Pauli principle.

If one estimates the exchange energy in a magnetic domain wall, it will be convenient to take all spins together, i.e., a continuous model of spin rotation

in a one-dimensional domain wall, the total  $E_{ex}$  inside the wall is,

$$E_{ex} = A \left( \frac{d\theta}{dx} \right)^2, \quad (1.3)$$

where  $A = s^2 a_L^2 J N_V / 2$  is the exchange stiffness constant (J/m), and is temperature dependent.  $s$  is the spin quantum number ( $= 1/2$ ), and  $a_L$  is the lattice constant.  $N_V$  indicates the number of nearestneighbor atoms per unit volume.  $q$  is the angle with respect to the easy axis of magnetization. For simple cubic (SC) and body centered cubic (BCC),  $J$  will be

$$J = 0.54 k_B T_C \quad \text{for SC and,} \quad (1.4)$$

$$J = 0.34 k_B T_C \quad \text{for BCC,} \quad (1.5)$$

where  $k_B$  and  $T_C$  are the Boltzmann constant and the Curie temperature, respectively.

It should be noted that the exchange energy plays a role to make a magnetic DW as wide as possible. Because the exchange energy decreases with decreasing angle between spins on neighboring atoms inside the DW, the spins gradually rotate and lead to a certain width of the magnetic DW.

### 1.1.3 Anisotropy Energy

It depends on the orientation of the magnetization with respect to the crystallographic axes of the material. This energy term is called the magnetic anisotropy energy. Basically, it is the result from spin-orbit interaction. Many kinds of ferromagnetic films have a uniaxial anisotropy, whether they are polycrystalline or single crystal, elements or alloys. When it is undisturbed crystal, the anisotropy energy will be minimized along certain crystal axes. However, anisotropy can be induced by symmetry breaking of the crystal structure at the interface and surface, by anisotropic modulation of atoms, or by alignment of surface/interface defects.

## Cubic anisotropy

The cubic anisotropy is magnetocrystalline in nature, and arises from the interaction of the atomic magnetic moments with the intrinsic symmetry of their crystalline environment via a spin-orbit interaction. The cubic anisotropy energy density is basically expressed by

$$E_C = K_1 (m_x^2 m_y^2 + m_x^2 m_z^2 + m_y^2 m_z^2) + K_2 m_x^2 m_y^2 m_z^2 + \dots, \quad (1.6)$$

where  $m_x$ ,  $m_y$  and  $m_z$  are the magnetization along x, y and z crystal axes, respectively.  $K_i$  is the  $i$ th order anisotropy. Although the second order term and other higher order terms can be mostly neglected at room temperature, they are important at low temperature.

## Volume and surface/interface anisotropies

Making the magnetic ultrathin films, surface and interface anisotropies have to be considered, because of missing of neighbor atoms [2]. Surprisingly, a much stronger anisotropy was found for mono atomic transition metal films compared with bulk materials [3]. In the case the magnetic film with out-of-plane uniaxial anisotropy (along the z axis), the energy is symmetric in the film plane. Then the surface anisotropy energy density is

$$E_S = K_S \sin^2 \theta, \quad (1.7)$$

where  $\theta$  is the angle between the magnetization and the z axis, and  $K_S$  the surface anisotropy.

The volume anisotropy is also not negligible for magnetic thin films. Hexagonal or tetragonal crystals (for example, a (0001)-hcp Co [4] or an epitaxially grown Ni film on a Cu(001) surface [5], respectively) show a uniaxial volume

anisotropy ( $K_u$ ) normal to the film plane for a certain thickness range. The volume anisotropy energy density can be written as

$$E_V = K_{u1} \sin^2 \theta + K_{u2} \sin^4 \theta, \quad (1.8)$$

where  $\theta$  is the angle between anisotropy axis and magnetization. Because of time inversion symmetry, the odd powers do not appear.

The total anisotropy energy density in a magnetic thin film is the following (with  $d$  the film thickness),

$$E = E_V + \frac{E_S}{d}, \quad (1.9)$$

#### 1.1.4 Zeeman Energy

Zeeman energy is the interaction energy of the magnetization vector field  $\vec{M}$  with an external magnetic field  $\vec{H}_{Ext}$ . Then the Zeeman energy is

$$E_Z = \mu_0 \int_V \vec{M} \cdot \vec{H}_{ext} dV, \quad (1.10)$$

## 1.2 Types of the Domain Wall: Bloch and Néel Walls

As mentioned above the magnetic domain boundaries have a certain width. There are two main types of spin structures inside the domain walls, Bloch and Néel types. Besides many other kinds of domain walls exist. One of them is called the cross-tie wall, which is an intermediate state between Bloch and Néel walls, and it is composed of a mixture of Bloch and Néel walls [1],[6]. The spin structures of Bloch and Néel walls are shown. The Bloch wall is usually preferable in bulk materials. Spins rotate in the plane parallel to the wall plane. The wall width of a 180° Bloch wall is most commonly defined by  $\pi\sqrt{\frac{A}{K}}$ , where  $A$  and  $K$  are the exchange constant and anisotropy energy, respectively [1]. Then the wall profile basically follows a sine law. In thin films, however, a

Bloch wall induces surface charges by its stray field. Then the Néel wall become more favorable when the film thickness becomes smaller than the wall width. In a Néel wall, spins rotate in the film plane. The width and profile of the Néel wall are difficult to define. The Néel wall has a narrow core and  $\mu\text{m}$ -long tails on both sides. The core width is of the order of the exchange length  $[=\sqrt{A/K_d}$  (nm scale)], where  $K_d$  is the demagnetizing energy. The Néel wall profile is well explained in [1].

### 1.3 Dzyaloshinskii-Moriya Interaction and Chiral Domain Wall

Recently, the Dzyaloshinskii–Moriya interaction (DMI), which plays a role as antisymmetric exchange coupling, has attracted great interest. The origin of the DMI is the spin-orbit scattering of electrons in an inversion asymmetric crystal field, and it appears in systems with broken inversion symmetry such as at the surface (or interface) of magnetic layer(s) and in specific metallic alloys. The existence of the DMI can induce chiral spin structures such as skyrmion and chiral domain walls.

Spin-dependent energy arising from the Pauli exclusion principle is modeled as a spin interaction in a vector model. Energy of the Heisenberg exchange interaction can be written by [7],[8]

$$E_{ex} = - \sum_{i,j} J_{i,j} \vec{S}_i \cdot \vec{S}_j \quad (1.11)$$

, where  $J_{i,j}$  ( $\sim J$ ) denotes the magnetic exchange coupling between local spin moments  $S_i$  and  $S_j$  on arbitrary lattice sites  $i$  and  $j$ , respectively. This expression is universally known as the Heisenberg Hamiltonian, called as the Heisenberg exchange interaction. It is favor parallel spin orientation for  $J > 0$ , whereas antiparallel spin orientation for  $J < 0$ . By denoting this mechanism,

this may lead to a variety of magnetic structures, from the ferromagnetic and antiferromagnetic state to complex, non-collinear spin textures. Though the ferromagnetic or antiferromagnetic state can be dominated by a nearest neighbor exchange interaction, complex magnetic structures often reflect a situation of competing magnetic interactions.

Contrasted with the Heisenberg exchange interaction (the symmetric energy term), the Dzyaloshinskii-Moriya interaction (DMI) links the spins via a vector product and can be written by [8],

$$E_{DMI} = - \sum_{i,j} \vec{D}_{i,j} \cdot (\vec{S}_i \times \vec{S}_j) \quad (1.12)$$

, where  $\vec{D}_{i,j}$  ( $\sim \vec{D}$ ) denotes the Dzyaloshinskii vector. Equation(1.12) explains the antisymmetric energy term arising from the spin-orbit scattering of electrons in an inversion asymmetric crystal field, and it appears in systems with broken inversion symmetry such as at the surface (or interface) of magnetic layer(s) and in specific metallic alloys. It prefers a 90-spin spiral feature and the sign of  $\vec{D}$  determine the rotational sense. So it leads to spin structures with a certain chirality being favored over the opposite chirality. To easily understand, consider a highly symmetric system of two spins, as sketched in the top of Figure 1.1(a). Going from the left to the right spin, the magnetization rotates counterclockwise. We perform two energy-conserving symmetry operations: rotation around the x-axis and spin inversion. The result is the same system, but now with a clockwise rotation of the magnetization. Hence, the clockwise and counterclockwise configurations have the same energy. This is to be expected from direct, isotropic exchange: the exchange energy simply depends on the relative orientation of the spins.

However, the situation changes when the exchange between the two sites is mediated through spin-orbit coupling by a third site, for example a Pt ion, that

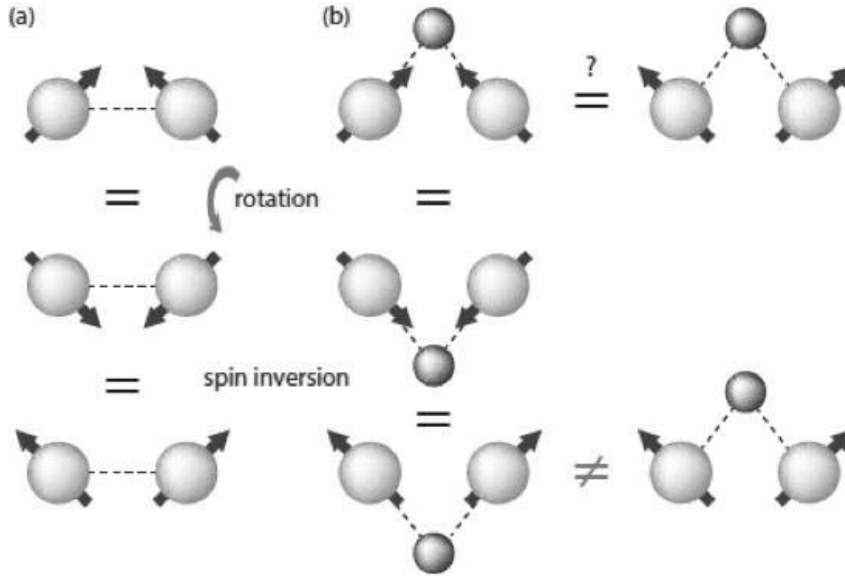


Figure 1.1 DMI from symmetry arguments. (a) In a symmetric system, a left-handed spin configuration (top) can be transformed to a right-handed configuration without changing the energy. (b) Applying the same transformations to a system including a symmetry-breaking third ion, it is not possible to transform the handedness without changing the relative position of this ion, hence the energy can depend on the chirality.

is situated above the original sites, as shown in Figure 1.1(b). Clearly, this system has a reduced symmetry compared to the initial situation. In this situation, the same symmetry operations can be used to transform from a counterclockwise to a clockwise rotation, but now the Pt ion is situated below rather than above the spins, hence represents a ‘sample’ different from the original one. Therefore, within the original sample, symmetry allows for a different energy of the two chiralities, because of the different orientation of the spins with respect

to the third ion.

The reason, why the DMI favors Néel walls rather than Bloch walls, can be understood by using (1.12) in terms of magnetization gradients in a 2D ultrathin film, [9]

$$E_{DMI} = D \left[ m_z \frac{\partial m_x}{\partial x} - m_x \frac{\partial m_z}{\partial x} + m_z \frac{\partial m_y}{\partial y} - m_y \frac{\partial m_z}{\partial y} \right] \quad (1.13)$$

If we think about the case of a 1-dimensional nanostrip with a confined width, it can assume that there are no gradients along the y direction and therefore the last two terms in (1.13) vanish.

Then, it is easily seen that the energy within the DW depends on its orientation in the x direction: if we invert  $m_x$ , both energy terms change sign.

The same goes for an inversion of  $m_z$ . Therefore, assuming a positive  $D$ , if  $m_z$  rotates from up-to-down the DW minimizes its energy by orienting itself along -x, whereas in a down-to-up configuration the DW energy is minimal along +x. This way, the sense of rotation (left-handed versus right-handed) should always be the same when DMI is present. However, the strength of  $D$  has to be strong enough to overcome the DW shape anisotropy  $H_K$  which favors Bloch walls.

## Chapter 2

# DW Dynamics in Creep regime

### 2.1 Maximizing DW Speed via Magnetic Anisotropy Adjustment in Pt/Co/Pt Films

We report an experimental observation that indicates that a direct relation exists between the speed of the magnetic domain-wall (DW) motion and the magnitude of the perpendicular magnetic anisotropy (PMA) in Pt/Co/Pt films. It is found that by changing the thicknesses of the nonmagnetic Pt layers, the PMA magnitude can be varied significantly and the field-driven DW speed can also be modified by a factor of up to 50 under the same magnetic field. Interestingly, the DW speed exhibits a clear scaling behavior with respect to the PMA magnitude. A theory based on the DW creep criticality successfully explains the observed scaling exponent between the DW speed and the PMA magnitude. The presented results offer a method of maximizing the DW speed in DW-mediated nanodevices without altering the thickness of the magnetic Co layer.

### 2.1.1 Introduction

The dynamics of the magnetic domain wall (DW) has been actively studied in recent years because of the interesting physical phenomena related to it and its promising applications in next-generation memory and logic devices [10],[11],[12],[13]. For high performance in these applications, it is essential to achieve a high DW speed, and many studies have been devoted to this purpose [14],[15],[16]. It has been reported that the DW speed is very sensitive to the thickness of the magnetic layer, and that in general, a thinner magnetic layer provides a faster DW speed [17]. Here, to further enhance the speed even in films with the thinnest feasible magnetic layer, we examined the effect of the thicknesses of the nonmagnetic layers adjacent to the magnetic layer. Interestingly, the DW speed was found to be strongly affected by the thicknesses of the nonmagnetic layers. To clarify the origin of this effect, a quantitative analysis based on the creep-scaling law was adopted, and the correlation between the analysis results and the magnetic properties is discussed.

### 2.1.2 Sample Preparation & Experimental Methods

#### Sample Preparation

For this study, a series of Pt/Co/Pt films with perpendicular magnetic anisotropy (PMA) with various thicknesses of the upper and lower Pt layers,  $t_u$  and  $t_d$ , was prepared via dc magnetron sputtering. The detailed sample structure is Si/SiO<sub>2</sub>/5.0-nm Ta/ $t_d$  Pt/0.3-nm Co/ $t_u$  Pt, as shown in Figure 2.1(a);  $t_d$  varies in the range between 1.5 and 3.0 nm in 0.5-nm intervals, and  $t_u$  varies in the range between 1.0 and 3.0 nm in 0.5-nm intervals. Using a vibrating sample magnetometer, the saturated magnetization  $M_S$  was found to remain nearly constant at  $(1.3 \pm 0.3) \times 10^6$  A/m among all samples. The uniaxial

anisotropy constant  $K$  ( $=H_k M_S/2$ ) was also determined from the measurement of the anisotropy field  $H_k$  based on an extraordinary-Hall-voltage measurement scheme [18]. The values of  $K$  are summarized in Table 2.1. The positive values of  $K$  indicate that all samples have PMA.

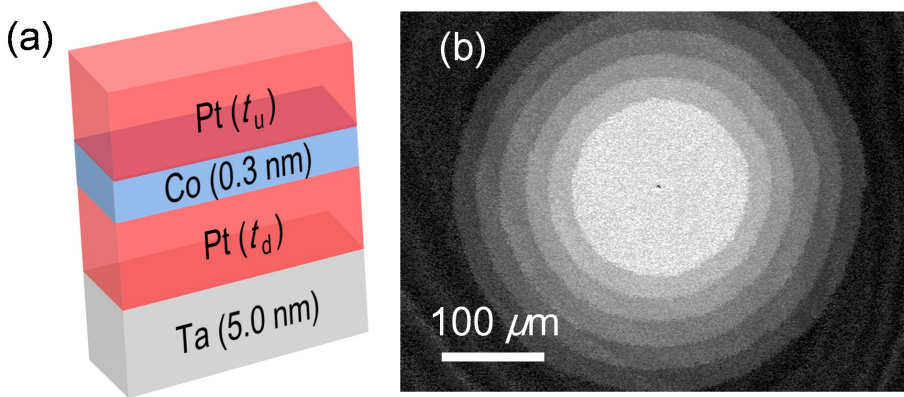


Figure 2.1 (a) Schematic layer structure of the samples. (b) Image of the expansion of circular domains under an external magnetic field (3.5 mT). This image was obtained by combining several domain images that were captured sequentially with a constant time step (350 ms) using a MOKE microscope.

## Experimental Methods

The domain images were captured using a magneto-optical Kerr effect (MOKE) microscope with a field of view of  $500 \mu\text{m} \times 375 \mu\text{m}$ . This microscope is equipped with an out-of-plane electromagnet that produces a magnetic field within the range of  $\pm 0.2$  T by means of a bipolar power supply. In a field-driven DW motion experiment, a reversed domain is initially created in the form of a circular domain via the thermomagnetic writing technique [19],[20]. A constant magnetic field  $H$  is then applied, and a series of domain images with a constant

(unit:  $10^5 \text{ J/m}^3$ )

	$t_u=1.0 \text{ nm}$	1.5 nm	2.0 nm	2.5 nm	3.0 nm
$t_d=1.5 \text{ nm}$	6.0±0.9	6.1±0.9	8.0±1.2	4.0±0.6	4.4±0.7
2.0 nm	6.8±1.0	9.3±1.4	5.3±0.8	8.0±1.2	8.1±1.2
2.5 nm	10.4±1.6	7.5±1.1	9.3±1.4	8.4±1.3	6.7±1.0
3.0 nm	10.1±1.5	7.9±1.2	6.6±1.0	7.0±1.1	6.9±1.0

Table 2.1 PMA constant  $K$  of the Si/SiO<sub>2</sub>/5.0-nm Ta/ $t_d$  Pt/0.3-nm Co/ $t_u$  Pt films with different  $t_d$  and  $t_u$ .

time interval is simultaneously captured. Figure 2.1(b) provides an example of successive circular-domain images of field-driven DW motion under an external magnetic field (3.5 mT) with a constant time step (350 ms) for a sample with  $t_d=2.5$  nm and  $t_u=1.5$  nm. This image was constructed by combining several successively acquired images, and thus, each single image shows several DWs expanding in time. From these circular DW images, one can measure the DW speed  $v$  from the change in radius with a constant time step. In the present experiment,  $v$  was determined from 10 repeated measurements for each  $H$  and for each sample. It was also confirmed that for the same  $v$ , identical behavior was observed for both domain polarities after the strength of the external magnetic field was carefully calibrated.

### 2.1.3 Result.1: Large Enhancement of the DW Speed by 50 Times

Figure 2.2 shows the plot of the measured  $v$  with respect to  $H$  for Sample I, with  $t_d=1.5$  nm and  $t_u=2.5$  nm, and Sample II, with  $t_d=2.5$  nm and  $t_u=1.5$  nm. Although these two samples are nearly identical except for the fact that the thicknesses of the upper and lower Pt layers are reversed, they exhibit very distinct behavior. Sample I exhibits a DW speed of up to approximately 10

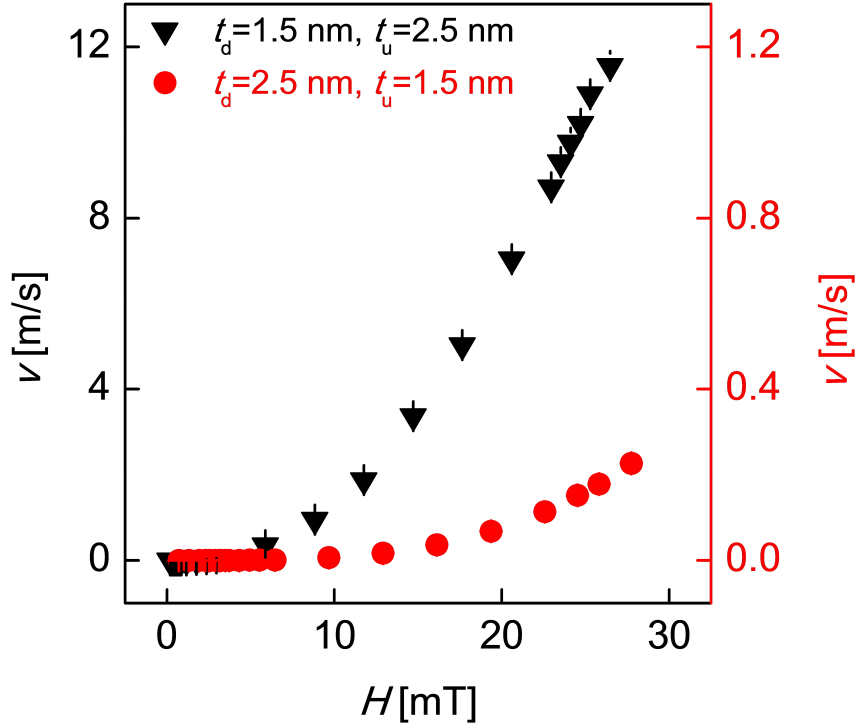


Figure 2.2 Measured  $v$  with respect to  $H$  for Sample I ( $t_d=1.5$  nm and  $t_u=2.5$  nm) and Sample II ( $t_d=2.5$  nm and  $t_u=1.5$  nm).

m/s, whereas Sample II exhibits a DW speed of less than 0.2 m/s under the same magnetic field. Note that the speed is enhanced by more than a factor of 50 in Sample I compared to Sample II.

#### 2.1.4 Result.2: DW Speed & Creep Scaling Constant in Pt/Co/Pt Films

To quantitatively analyze these contrasting DW-motion behaviors,  $v$  is plotted with respect to  $H^{-1/4}$  in Figure 2.3 for samples with several different values of  $t_d$  and  $t_u$ . It is clear from the figure that the speed  $v$  for each sample follows

the creep-scaling law [17],[21],[22]

$$v = v_0 \exp\left[-\frac{\alpha}{k_B T} H^{-1/4}\right], \quad (2.1)$$

where  $v_0$  is the characteristic speed,  $\alpha$  is the creep-scaling constant,  $k_B$  is the Boltzmann constant, and  $T$  is the temperature. It was confirmed that this creep-scaling behavior was observed in all samples in this study. Note that all analyses were performed in the creep regime, where the DW speed is slower than a few mm/s. From the best fit with Eq. (2.1),  $\alpha$  was determined and summarized with respect to  $t_d$  and  $t_u$  in Table 2.2. The table clearly illustrates that  $\alpha$  is sensitive to both  $t_d$  and  $t_u$ . The largest value of  $\alpha$  corresponds to the sample with the largest  $t_d$  and the smallest  $t_u$ , whereas the smallest value of  $\alpha$  is seen for the sample with the smallest  $t_d$  and the largest  $t_u$ .

## 2.1.5 Analysis & Discussion & Conclusions

### Analysis & Discussion

It is interesting to note that the PMA constant  $K$  also exhibits a similar dependence on  $t_d$  and  $t_u$ , as seen in Table 2.1. Although the values of  $K$  are somewhat scattered, there exists the general trend that  $K$  increases as  $t_d$  increases and/or  $t_u$  decreases. The dependence on  $t_d$  can be easily understood, as a 1.5-nm bottom Pt layer is not sufficiently thick to fully induce PMA at the Pt/Co interface and the crystalline structure in the bottom Pt layer becomes enhanced as its thickness increases from 1.5 nm to 3.0 nm [23]. The influence of  $t_u$  might be attributable to the interdiffusion at the upper Co/Pt interface [24],[25]. For a more quantitative comparison, the correlation between  $K$  and  $\alpha$  is plotted in Figure 2.4. Surprisingly, all values ( $K, \alpha$ ) lie on a single curve, indicating a direct relation between  $K$  and  $\alpha$ .

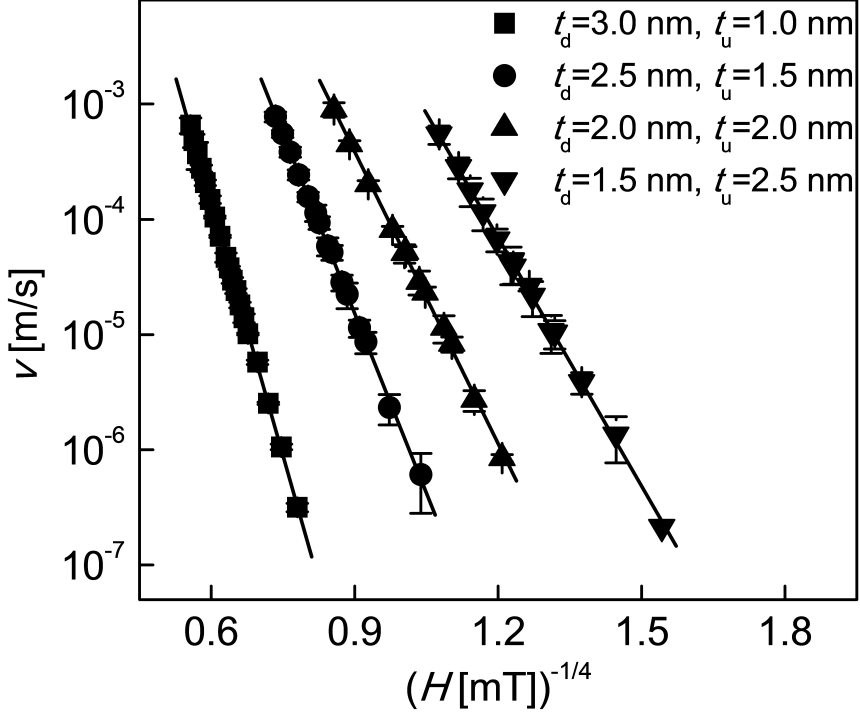


Figure 2.3 Creep-scaling plot of  $v$  with respect to  $H^{-1/4}$  for several samples with different values of  $t_d$  and  $t_u$  as denoted in the figure. The solid lines represent the best fits using Eq. (2.1).

To understand the relation between  $K$  and  $\alpha$ , we adopt here the creep-scaling law proposed in Ref. [22]. The definition of  $\alpha$  in this creep-scaling law yields the proportionality  $\alpha \propto (U_C H_{crit})^{1/4}$ , where  $U_C$  and  $H_{crit}$  are the scaling energy constant and the critical field, respectively. According to Ref. [22], the quantities  $U_C$  and  $H_{crit}$ , in turn, exhibit the proportionalities  $U_C \propto (f_{pin}^2 \sigma_{DW})^{1/3}$  and  $H_{crit} \propto (f_{pin}^4 / \sigma_{DW})^{1/3}$ , where  $f_{pin}$  and  $\sigma_{DW}$  are the local pinning force and the DW energy density per unit area, respectively. Note that  $f_{pin}$  is inversely proportional to the DW width  $\delta_{DW}$  [22]. In ferromagnetic materials with a uni-

(unit:  $10^{-20} \text{ JT}^{1/4}$ )

	$t_u=1.0 \text{ nm}$	1.5 nm	2.0 nm	2.5 nm	3.0 nm
$t_d=1.5 \text{ nm}$	1.34±0.10	1.32±0.20	1.46±0.10	1.21±0.10	1.03±0.20
2.0 nm	1.48±0.20	1.82±0.10	1.42±0.10	1.65±0.10	1.65±0.10
2.5 nm	2.42±0.10	1.75±0.10	1.97±0.10	1.77±0.10	1.57±0.10
3.0 nm	2.46±0.10	1.97±0.20	1.79±0.20	1.78±0.10	1.75±0.10

Table 2.2 Creep scaling constant  $\alpha$  of the Si/SiO<sub>2</sub>/5.0-nm Ta/ $t_d$  Pt/0.3-nm Co/ $t_u$  Pt films with different  $t_d$  and  $t_u$ .

axial magnetic anisotropy  $K$ , it is well known [26] that  $\sigma_{DW}$  and  $\delta_{DW}$  follow the relations  $\sigma \propto K^{1/2}$  and  $\delta_{DW} \propto K^{-1/2}$ , respectively. Thus, one can finally obtain the relation:

$$\alpha \propto K^{5/8}. \quad (2.2)$$

The dotted lines in Figure 2.4 represent the proportionality given by Eq. (2.2). The good conformity between this proportionality and the experimental data supports the validity of the above theory in describing the relation between  $\alpha$  and  $K$ . Note that the presented analysis was performed in the creep regime for slow motion under a small magnetic field. Under a large field, the DW exhibits rapid motion that belongs to the flow regime. Although such rapid motion in the flow regime is not directly analyzed in this study, a relation similar to that found in the creep regime is expected in the flow regime, as the DW speed undergoes a smooth transition between the two regimes [17], and thus, the DW speed of Sample I remains faster than that of Sample II even in the flow regime, as seen in Figure 2.2.

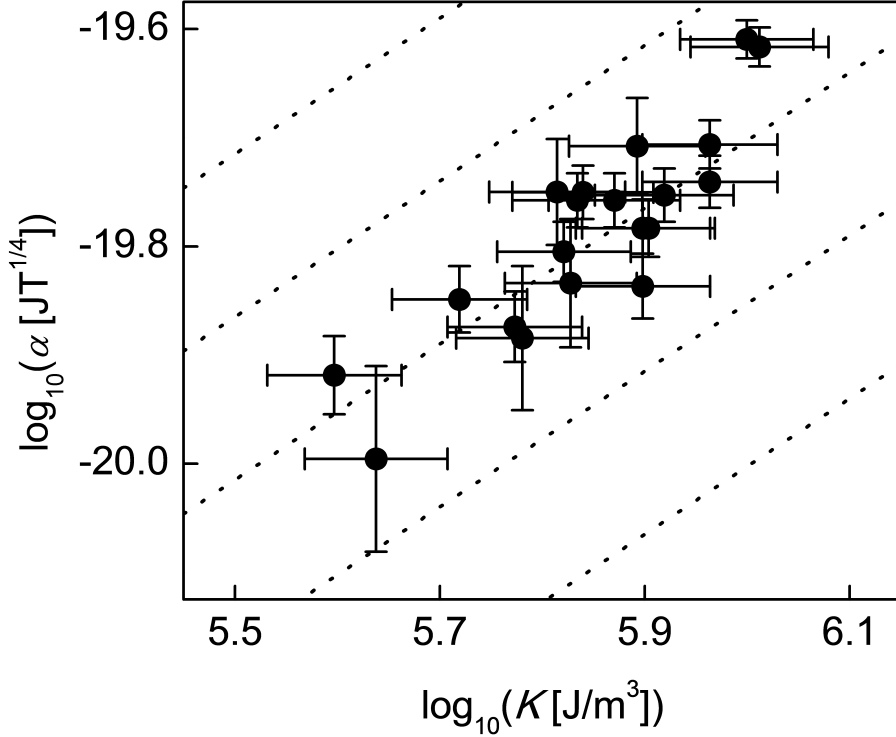


Figure 2.4 Correlation plot of  $\alpha$  with respect to  $K$ . All values of  $\alpha$  and  $K$  are identical to those presented in Tables I and II. The dashed lines represent the proportionality given by Eq. (2.2).

## Conclusions

In summary, we observed that the DW speed is sensitive to the thicknesses of the nonmagnetic Pt layers in Pt/Co/Pt films. Based on a quantitative analysis, it was revealed that the primary origin of this dependence can be attributed to the variation of the uniaxial PMA. The DW speed varied by a factor of more than 50 among the investigated samples under the same magnetic field. Our results offer a method of maximizing the DW speed without changing the thickness of the magnetic Co layer.

## Chapter 3

# DW Dynamics & Asymmetric DW Motion in Flow Regime

The magnetic domain-walls (DWs) motion induced by spin-polarized current and magnetic field has proposed novel concepts for memory and logic devices [10],[11]. Recently, many interesting physical phenomena on the chiral DW have been reported with perpendicular magnetic anisotropy [12]. When applying the in-plane magnetic field on the DW, it modifies DW structure, forms chiral DW, and then affects direction of the DW motion as well as magnitude of its speed [27]. Many researches related with a chiral DW, both current-driven and field-driven DW motion, have been performed experimentally, calculated numerically, and carried out micromagnetic simulation [9]. In the current-driven DW motion which is governed by spin-Hall effect (damping-like torque), once applying the in-plane magnetic field, DW structure can be formed as right-handed or left-handed Néel wall, (between them it can be formed as Bloch wall), and then the direction of the DW motion and magnitude of its speed can be altered in accordance with the types of the DW. Although this explanation

can suggest a good physical intuition for comprehending the current-driven DW motion, in real situation, it is quite difficult to understand due to the presence of many other effects which are spin-transfer torques and field-like spin-orbit torque, related with the Rashba effects. In the field-driven DW motion, after applying the in-plane magnetic field, DW structure is also able to be varied, and then only the magnitude of the DW speed is changed. Recently, there exists experimental demonstration in creep regime and it can be explained successfully by the DW energy model [27]. In this model, in-plane field as the Zeeman energy competes with the DW anisotropy energy for minimizing the DW energy which determines the DW angle, and as a consequently DW speed is varied. This is also similar interpretation in the case of current-driven DW motion as understanding the phenomenon based on the transition from Néel to Bloch DW. Similar experimental results are also reported in the flow regime [12]. In this paper, although they try to interpret this phenomenon caused by the variation of the DW width from applying to the in-plane magnetic field [28], it cannot explain well because the simulation cannot realize the experimental result as well as the discrepancy exists between DW width's variation and DW speed's variation in the simulation. So it is not fully understood the role of the in-plane magnetic field affecting DW motion in flow regime. In this paper, we investigate the origin of DW speed variation in flow regime by use of the 1-dimensional q-phi model based on the LLG equation.

### **3.1 Broken chirality governing asymmetric domain-wall motion in the flow regime**

We now consider the effects of in-plane magnetic field and DMI, which is affected as effective in-plane field, in 1-dimensional magnetic DW. These contributions

are added to the Landau-Lifshitz-Gilbert (LLG) equation, which describes the time evolution of the magnetization  $M$ . We use the generalized 1-dimensional DW motion by constituted by the Slonczewski [29], and then two collective dynamics equations coupled  $q$  and  $\phi$  are

$$\alpha/\Delta\dot{q} + \dot{\phi} = \gamma_0 H_z, \quad (3.1)$$

$$1/\Delta\dot{q} - \alpha\dot{\phi} = \gamma_0 [(H_x + H_{DMI}) \sin \phi - H_k \sin \phi \cos \phi], \quad (3.2)$$

where  $\alpha$  is a damping constant,  $\Delta$  is a DW width,  $\dot{q}$  is the DW speed,  $\dot{\phi}$  is angular speed,  $\gamma_0$  is the gyromagnetic ratio,  $H_z$  is the out-of-plane magnetic field,  $H_x$  is the in-plane magnetic field,  $H_{DMI}$  is the DMI-induced field,  $H_k$  is the wall-anisotropic field, and  $\phi$  is the DW angle from the Bloch wall.

### 3.1.1 Steadt-State Flow & Walker Breakdown

From the Ref. [29], DW energy  $\sigma$  density is described by,

$$\sigma = \frac{2A}{\Delta} + 2K_{eff}\Delta + 2K_D\Delta \cos^2 \phi - \pi M_s (H_x + H_{DMI}) \Delta \cos \phi, \quad (3.3)$$

where  $A$  is the exchange stiffness constant,  $K_{eff}$  is the effective anisotropy energy,  $M_s$  is the saturated magnetization. By using the Eq.(3.3), to find the minimum condition of DW energy with respect to the DW width, solve the  $d\sigma/d\Delta=0$ , and then the equilibrium DW width  $\Delta^*$  can be obtained as,

$$\Delta^* = \sqrt{\frac{A}{K_{eff}}} \sqrt{\frac{1}{1 + \frac{K_D}{K_{eff}} \cos^2 \phi - \frac{\pi M_s (H_x + H_{DMI})}{2K_{eff}} \cos \phi}}, \quad (3.4)$$

To determine the equilibrium DW width, we should obtain the equilibrium angle  $\phi^*$ . By use of the Eqs. (3.1) and (3.2), we eliminate  $q$  and obtain the relation for  $\phi$  only,

$$\dot{\phi} = \gamma_0 \frac{1}{1 + \alpha^2} [H_z - \alpha ((H_x + H_{DMI}) \sin \phi - H_k \sin \phi \cos \phi)], \quad (3.5)$$

In the steady-state flow regime, where DW angle is fixed (it means  $\dot{\phi}=0$ ), DW speed from Eq.(3.1) is

$$\dot{q} = \gamma_0 \frac{\Delta^*}{\alpha} H_z \quad (3.6)$$

And  $\phi^*$  can be easily obtained from the Eq.(3.5) for condition,  $\dot{\phi}=0$ . Because this is the biquadratic with respect to  $\cos^*$ , it can be calculated numerically. In this regime called steady-state flow, it is easily to see that all of the in-plane fields ( $H_x + H_{DMI}$ ) affect the DW speed as variation of the DW width. This, which is already reported simulation in previous report [27], explains the DW speed variation by DW width variation. To estimate the DW speed variation in this regime, we consider the well-known magnetic parameters [9]. Comparing  $H_x=0$  mT and  $H_x=200$  mT, the variation of DW width is 60%, as a consequently the possible variation of the DW speed is also ???. It cannot be shown 500% percent of DW width variation, so it cannot explain about the recent progressed experimental result.

It is widely known that when we increase  $H_z$ , the transition appear from the steady-state flow into precession flow regime where the dynamics of DW at high  $H_z$  is quite distinct phenomena previous regime. From the Eq.(3.5) considering  $(H_x + H_{DMI})=0$ , when  $H_z$  is much higher than the DW anisotropy field  $H_k$ , there exists a condition of  $\dot{\phi} \neq 0$  which means the situation just rotating the DW magnetization. This transition point about  $H_z$  is called as walker breakdown field  $H_W$ . From the Eq. (3.5), the  $H_W$  means the maximum value of Hz at  $\dot{\phi}=0$ . So  $H_W$  can be derivative by,

$$H_W = \alpha (H_x + H_{DMI}) \sin \phi_W - \alpha H_k \sin \phi_W \cos a \phi_W, \quad (3.7)$$

where  $\phi_W$  is the critical angle at walker breakdown and is given by  $\cos \phi_W = \frac{(H_x + H_{DMI}) \pm \sqrt{(H_x + H_{DMI})^2 + 8H_k^2}}{4H_k}$ . From this equation, the more  $H_x$  increases, the

high  $H_W$  is determined. It means that walker breakdown is suppressed by in-plane magnetic field.

### 3.1.2 Precession Flow

Next above walker breakdown, it is called precession flow regime where there coexists the rotational and translational DW motions. Due to the rotating DW in this regime, it cannot define the DW position by steady-state point of view. So we consider the average speed of DW by use of the period of precession. From the Eq.(3.5), the period can be derived by

$$T = \frac{1 + \alpha^2}{\gamma_0} \int_0^{2\pi} \frac{d\phi}{H_z - \alpha(H_x + H_{DMI}) \sin \phi + \alpha H_k \sin \phi \cos \phi}. \quad (3.8)$$

In order to arrange the simple form, we estimate each value of the parameter. Because  $H_k$  is related by  $N_x M_s \sim$  tens of mT [?], we can estimate  $\alpha H_k \sim$  a few mT, and then this term is quite small compared with  $H_z - \alpha(H_x + H_{DMI}) \sin a\phi$ . Therefore, we can rewrite the Eq.(3.7),

$$T = \frac{1 + \alpha^2}{\gamma_0} \int_0^{2\pi} \frac{1}{H_z - \alpha(H_x + H_{DMI}) \sin \phi} \left[ \frac{1}{1 + \frac{\alpha H_k \sin \phi \cos \phi}{H_z - \alpha(H_x + H_{DMI}) \sin \phi}} \right] d\phi. \quad (3.9)$$

From the condition of  $H_z - \alpha(H_x + H_{DMI}) \sin \phi \geq \alpha H_k \sin \phi \cos \phi$ , it is possible to use the Taylor expansion,

$$T \cong \frac{1 + \alpha^2}{\gamma_0} \int_0^{2\pi} \frac{1}{H_z - \alpha(H_x + H_{DMI}) \sin \phi} \left( 1 - \frac{\alpha H_k \sin \phi \cos \phi}{H_z - \alpha(H_x + H_{DMI}) \sin \phi} \right) d\phi. \quad (3.10)$$

It can be separated by

$$T \cong \frac{1 + \alpha^2}{\gamma_0} \left[ \int_0^{2\pi} \frac{1}{H_z - \alpha(H_x + H_{DMI}) \sin \phi} d\phi - \int_0^{2\pi} \frac{\alpha H_k \sin \phi \cos \phi}{H_z - \alpha(H_x + H_{DMI}) \sin \phi} d\phi \right]. \quad (3.11)$$

From the integration table, the second term is zero. So first term is dominated for precession and the result is  $T \cong \frac{1 + \alpha^2}{\gamma_0} \frac{2\pi}{\sqrt{H_z^2 - [\alpha(H_x + H_{DMI})]^2}}$ . By the definition

of the the angular speed  $\langle \dot{\phi} \rangle = 2\pi/T$ , it is possible to write,

$$\langle \dot{\phi} \rangle = \frac{2\pi}{T} \cong \frac{\gamma_0}{1 + \alpha^2} \sqrt{H_z^2 - [\alpha(H_x + H_{DMI})]^2}. \quad (3.12)$$

From Eq.(3.12), when the  $H_x$  is increased, the angular speed is decreased where it means energy consumption for rotating motion is decreased. In the precession flow regime, we should consider the average over one period of the Eq.(3.1). So average DW speed is,

$$\langle \dot{q} \rangle = \frac{\Delta}{\alpha} \left( \gamma_0 H_z - \langle \dot{\phi} \rangle \right) \cong \frac{\Delta}{\alpha} \left( \gamma_0 H_z - \frac{\gamma_0}{1 + \alpha^2} H_z \sqrt{1 - \left[ \frac{\alpha(H_x + H_{DMI})}{H_z} \right]^2} \right). \quad (3.13)$$

For easy to understand Eq.(3.13), we consider the condition,  $\left[ \frac{\alpha(H_x + H_{DMI})}{H_z} \right]^2 \leq 1$  where Taylor expansion can be used,

$$\langle \dot{q} \rangle = \frac{\Delta}{\alpha} \left( \gamma_0 H_z - \langle \dot{\phi} \rangle \right) \cong \frac{\Delta}{\alpha} \left( \gamma_0 H_z - \frac{\gamma_0}{1 + \alpha^2} H_z \left[ 1 - \frac{1}{2} \left[ \frac{\alpha(H_x + H_{DMI})}{H_z} \right]^2 \right] \right). \quad (3.14)$$

$$\langle \dot{q} \rangle = \frac{\Delta}{\alpha} \left( \gamma_0 H_z - \langle \dot{\phi} \rangle \right) \cong \frac{\Delta}{\alpha} \gamma_0 H_z \left( 1 - \frac{\gamma_0}{1 + \alpha^2} \right) + \Delta \frac{\alpha \gamma_0}{1 + \alpha^2} \frac{(H_x + H_{DMI})^2}{2H_z}. \quad (3.15)$$

Equation (3.15) is constructed by the two different terms. The 1st term is the similar to the steady-state flow equation factored by  $\left( 1 - \frac{1}{1 + \alpha^2} \right)$  and the 2nd term is effect of  $H_x$ . From the 2nd term, we can easily obtain the minimum DW speed at  $H_x = H_{DMI}$ , which means  $H_{DMI}$  is the symmetric axis in the precession flow regime, similar to the creep regime [27]. And the minimum DW speed is determined only  $H_z$ . It is also found that DW speed is the quadratic form with respect to the  $H_x + H_{DMI}$ . This quadratic form is come from the rotating DW period, so the cause of DW speed enhancement in the precession regime is come from the increasing the DW period.

### 3.1.3 Numerical Calculation

Taking all of the analytic solutions in the flow regime, we can calculate the DW speed numerically. Material parameter is  $A=10\times 10^{-12}$  J/m,  $K_{eff}=6.5\times 10^5$  J/m<sup>3</sup>,  $M_s=1.3\times 10^6$  A/m,  $H_z$  from 0 to 100 mT,  $H_x$  from 0 to 100 mT, and  $H_{DMI}=0$  mT (because DMI is only the symmetric axis shift, we do not consider this term). Figure 3.1 shows that DW speed with respect to the  $H_z$  for various  $H_x$ . In the low  $H_z$  regime, it is clearly show that DW speed is linear relation as a function of the out-of-plane magnetic field. At the end of the steady-state flow regime, there exist the walker breakdowns for each  $H_x$ , which is as a function of  $H_x$  as shown inset of Fig. 3.1. It shows that  $H_W$  is increased when the in-plane magnetic field is increased and independent of the sign of  $H_x$ . Above the steady-state flow regime, it shows precession flow regime.

### 3.1.4 Micromagnetic Simulation

In the previous section, we derive the analytic solution of both flow regimes. To check the realization of this phenomenon and be compared with analytic form, we carry out the micromagnetic simulations. Material parameter is same as numerical calculation as denoted previous section. To compare the both flow regimes' DW speed variation, we carry out the simulations at both regimes. Figure 3.2(a) shows DW speed with respect to the  $H_z$  for various  $H_x$ . More specifically, we divide the DW dynamics two ragnes. Figure 3.2(b), which shows the DW speed with respect to the  $H_x$  at fixed  $H_z=50$  mT. One with  $H_x \leq 60$  mT is precession flow regime, which incsesres quite large and the other with  $H_x \geq 60$  mT is steady-state flow regime, which increase quite small compared with precession regime. From the Fig. 3.1 and 3.1, thess graphs show the good agreement of analytic form with the simulation. Note that the variation of the enhance-

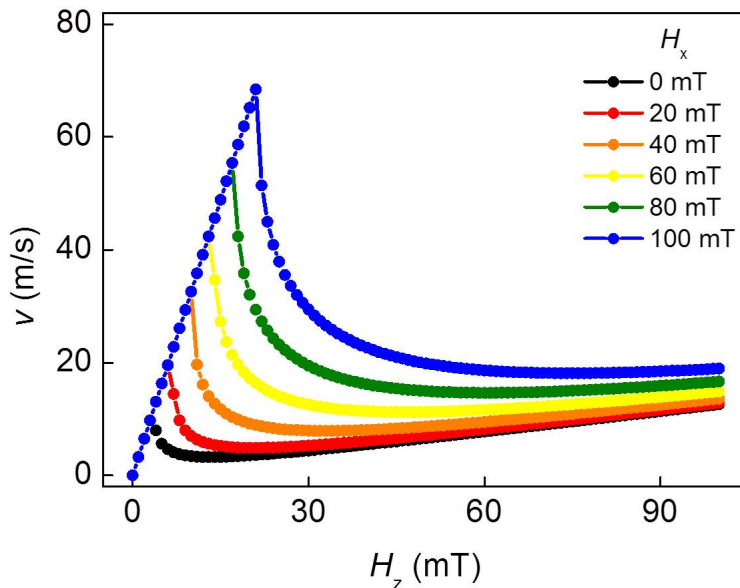


Figure 3.1 Analytic result: Domain wall speed with respect to the  $H_z$  for various  $H_x$

ment of DW speed is about 50% at steady-state flow, whereas enhancement of DW speed is more than 6 times at precession flow. This also demonstrates that the high enhancement of the DW speed happen in the precession regime.

### 3.1.5 Comparision between Experimental Result and Analytic solution

Finally, we perform the experiment and then compare the results with analytic explanation. For this, we choose the Pt/Co/Pt film with PMA film [27],[30]. To check the high DW speed about 10 m/s at  $H_z=51$  mT without  $H_x$ , we think this is the flow regime. And then, at fixed  $H_z=51$  mT, we measure the DW speed with respect to the in-plane magnetic field as shown in Fig. 3.3(a).

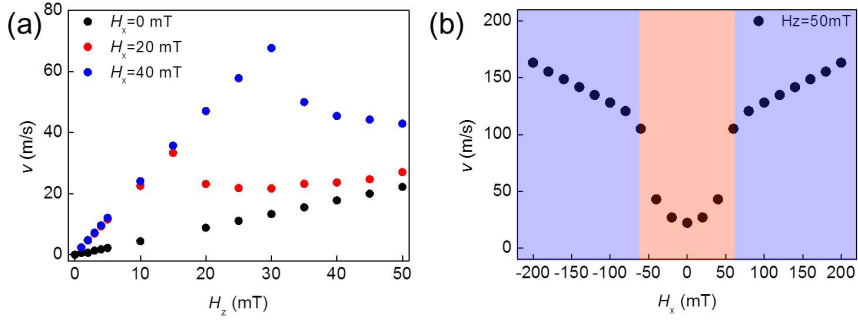


Figure 3.2 Micromagnetic Simulation: Domain wall speed (a) with respect to the  $H_z$  for various  $H_x$  and (b) with respect to the  $H_x$  at fixed  $H_z=50$  mT

It clearly shows that the symmetric axis appear at  $H_x=-60$  mT, which means DMI-induced field. The DW speed at  $H_x=150$  mT is 6 times compared with the speed at  $H_x=-60$  mT. From the Eq.(3.15), it should be check the rate of increase of the DW speed. Due to  $\alpha^2 \leq 1$ , we can also apply to the Taylor expansion from Eq.(3.15) and then derive,

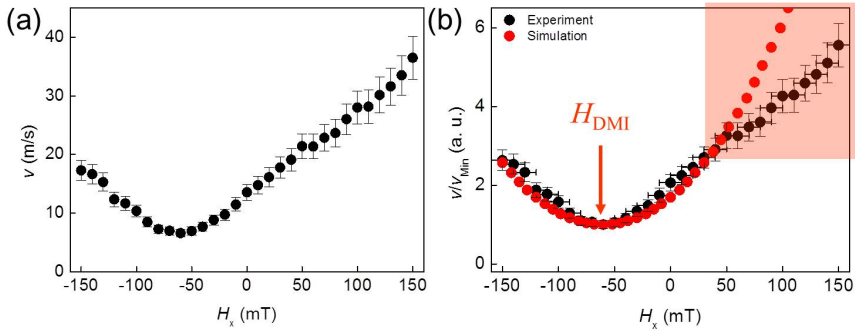


Figure 3.3 (a) Measured domain wall speed with respect to the  $H_x$  at fixed  $H_z=51$  mT and (b) Normalized domain wall speed both experimental result and analytic result

$$\langle \dot{q} \rangle = \frac{\Delta}{\alpha} \left( \gamma_0 H_z - \langle \dot{\phi} \rangle \right) \cong \Delta \alpha \gamma_0 H_z + \Delta \frac{\alpha \gamma_0}{1 + \alpha^2} \frac{(H_x + H_{DMI})^2}{2H_z}. \quad (3.16)$$

Variation is related with  $\frac{(H_x + H_{DMI})^2}{2(H_z)^2} \cong 6$  ( $H_z=51$  mT,  $H_x=150$  mT, and  $H_{DMI}=60$  mT). It is successfully explain the DW speed variation. To fit the experimental result from the analytic solution, we use the magnetic parameters from the Ref. [30]. Figure 3.3(b) shows the analytic result from the best fitting at fixed these values. Although this result has discrepancy of experimental result, the tendency of the DW speed variation can be explained qualitatively. In order to account quantitatively as well as qualitatively, it should be considered the real situations that the DW motion has the transition regime from creep, depinning, flow regimes and that other factors will be considered (2-dimensional effect). Nonetheless this result can suggest the physical intuition that the variation of DW speed is come from the precession flow regime.

### 3.1.6 Conclusion

In conclusion, we show the experimental result that varies DW speed as a function of the in-plane field in Pt/Co/Pt. The reason is come from the walker breakdown suppression from the in-plane field, as a consequently the angular period is increased by in-plane field in the precession regime, which explain well the experimental result. We can also suggest the analytic solution for precession flow regime. This analytic form is successfully explain the DW speed variation is directly related with  $H_x + H_{DMI}$  and the minimum DW speed is determined at  $H_x = H_{DMI}$ .

### 3.2 Universality of Chiral-Domain-Wall Motion by the Dzyaloshinskii-Moriya Interaction in the Creep and Flow Regimes

The phenomena related with the chiral domain walls (DWs) induced by the Dzyaloshinskii-Moriya interaction (DMI) have been widely reported for its interesting physical properties and promising technical applications [10],[11]. When an in-plane magnetic field  $H_x$  is applied in these DWs, it modifies the DW structure and consequently, results in an asymmetric DW motion with a finite DMI [27]. Recently, there are many studies about this asymmetric motion in the creep regime, explained by symmetric and asymmetric effects with respect to the DMI-induced effective field  $H_{DMI}$ ; the former is caused by the variation of the DW energy density [27],[31],[32] and the latter is caused by the chiral damping (or other mechanism)[31],[32]. In order to extend our understanding on such asymmetric DW motion, we examine the asymmetric DW motion in the creep and flow regimes. For this study, we prepared 2.0-nm Pt/0.3-nm Co/2.0-nm Pt films that exhibit a perpendicular magnetic anisotropy. The DW speed  $v$  was then measured with respect to  $H_x$  at a fixed out-of-plane magnetic field  $H_z$ , by use of a magneto-optical Kerr effect microscope. In the creep regime, the asymmetric DW motion can be explained by the combination between the symmetric and asymmetric effects. According to the method proposed in ref. [5],  $H_{DMI}$  was quantified as  $60\pm 5$  mT in creep regime. Interestingly, similar but a little bit different behavior was observed in the flow regime. Figure 3.4 shows  $v$  with respect to  $H_x$  at fixed  $H_z$ , (a) 1.7 mT for creep and (b) 51 mT for flow. The figure 3.4(b), at flow regime, clearly shows that the asymmetric effect is significantly suppressed. By using the method proposed in ref. [5], difference between DW speed in creep regime has only the symmetric effect, and so the

symmetric effect has the symmetric axis exactly the same with  $H_{DMI}$  in the creep regime as shown in Fig. 3.5. From this result, it is clearly shown that the effect from  $H_{DMI}$  is universal feature irrespective of the creep and dynamic regimes. Detail analysis will be discussed in the presentation.

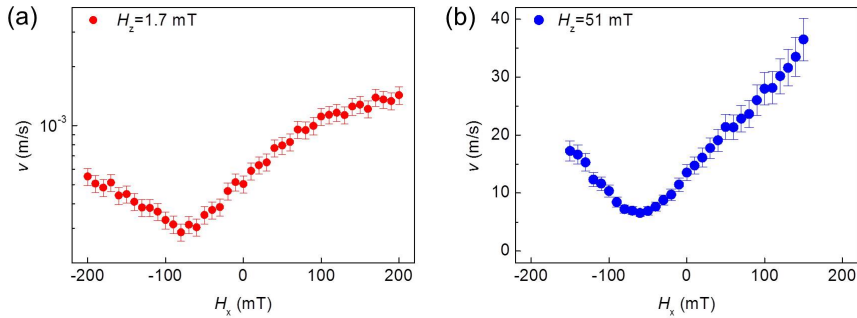


Figure 3.4 DW speed  $v$  with respect to the in-plane magnetic field  $H_x$  at fixed out-of-plane magnetic field (a)  $H_z=1.7$  mT for creep and (b) 51 mT for flow.

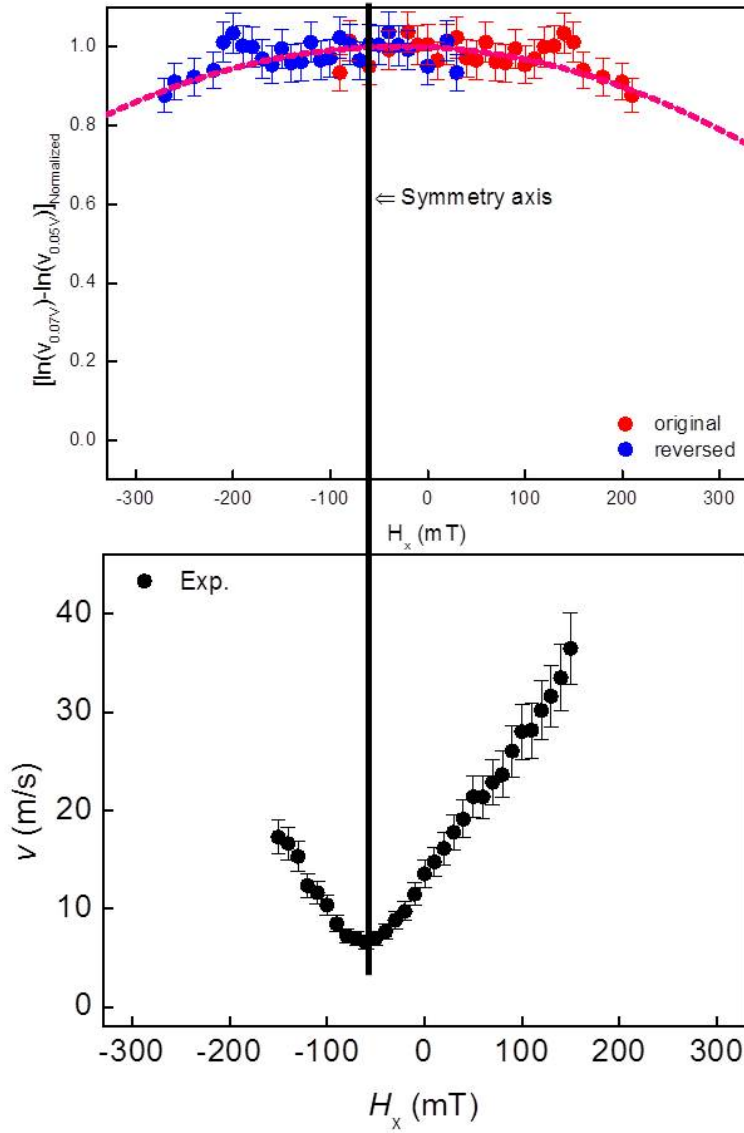


Figure 3.5 (a) Difference between DW speeds  $v$  with respect to the in-plane magnetic field  $H_x$  (b) DW speed  $v$  with respect to the in-plane magnetic field  $H_x$  at fixed out-of-plane magnetic field  $H_z = 51$  mT for flow.

# Chapter 4

## DMI meter 2.0

### 4.1 DMI meter 1.0: Asymmetric Magnetic Domain-Wall Motion by the Dzyaloshinskii-Moriya Interaction

We demonstrate here that ultrathin ferromagnetic Pt/Co/Pt films with perpendicular magnetic anisotropy exhibit a sizable Dzyaloshinskii-Moriya interaction (DMI) effect. Such a DMI effect modifies the domain-wall (DW) energy density and consequently, results in an asymmetric DW expansion driven by an out-of-plane magnetic field under an in-plane magnetic field bias. From an analysis of the asymmetry, the DMI effect is estimated to be strong enough for the DW to remain in the Néel-type configuration in contrast to the general expectations of these materials. Our findings emphasize the critical role of the DMI effect on the DW dynamics as the underlying physics of the asymmetries that are often observed in spin-transfer-related phenomena. In contrast to the general expectation that an in-plane magnetic field does not induce any force on the

domain walls to move, an asymmetric FIDWM is observed with respect to the in-plane magnetic field. This asymmetric FIDWM is found to be caused by a sizeable DMI. The direction, helicity, and magnitude of the DMI are quantitatively analyzed and will be discussed.

## 4.2 DMI meter 2.0: Measuring the Dzyaloshinskii-Moriya Interaction based on Angular Dependence of Asymmetric Magnetic DW Motion

Recently, much attention has focused on the Dzyaloshinskii-Moriya interaction (DMI) in ferromagnetic systems for magnetic-skyrmion-racetrack memory. In order to form a skyrmion state, it is needed to have the large DMI value  $D$  about  $3.5 \text{ mJ/m}^2$  which can be converted into the DMI-induced magnetic field  $H_{DMI}=636 \text{ mT}$ , where DW width is  $5 \text{ nm}$  and saturated magnetization is  $1.1 \times 10^6 \text{ A/m}$ . Recently, the measuring DMI technique based on asymmetric DW motion has been proposed. In this technique,  $H_{DMI}$  can be directly quantified by observing the shift  $H_{shift}$  of the symmetric axis in the DW speed  $v(H_x)$  measurement with respect to the in-plane magnetic field  $H_x$ . However, in material with skyrmion state where  $H_{DMI}$  is too large ( $>600 \text{ mT}$ ), it cannot be applicable due to limitation of the maximum strength  $H_{max}$  of the applied in-plane magnetic field.

### 4.2.1 Result.1: Angular Dependence of Asymmetric Magnetic DW Motion in Pt/Co/Pt

In this study, we propose an advanced technique to overcome such field-strength limit. The core idea is to utilize the dependence of  $H_{shift}$  on the tilting angle  $\theta$  of the DWs with respect to the direction of the in-plane magnetic field as show in Fig. 4.1(a). Figure 4.1(b) shows the  $H_{shift}$  measurements for the

tilted DWs with various  $\theta$  ( $0^\circ$ ,  $30^\circ$ ,  $60^\circ$ , and  $90^\circ$ ) for Pt/Co/Pt film. It is clear from the figure that  $H_{shift}$  is very sensitive to  $\theta$ , following a simple relation  $H_{shift}=H_{DMI}\cos\theta$  as demonstrated by Fig. 4.2 where the red line shows the best fit with  $\cos\theta$ . Therefore, with a large  $\theta$ ,  $H_{shift}$  becomes much reduced possibly less than  $H_{max}$ . The present idea can be also demonstrated to other films (Pt/Co/AlO<sub>x</sub> and Pt/Co/MgO), where  $H_{DMI}$  is even much larger than the field-strength limit of equipment, and thus enables the development of an advanced DMI meter based on asymmetric DW motion.

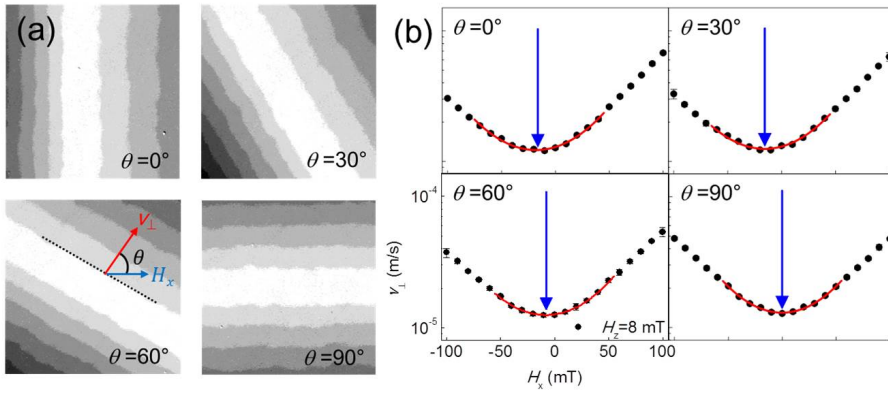


Figure 4.1 (a) the DW displacements for each  $\theta$ . (b) Speed  $v_\perp$  normal to the DW with respect to the in-plane magnetic field  $H_x$  for various DW tilting angle  $\theta$  ( $0^\circ$ ,  $30^\circ$ ,  $60^\circ$ , and  $90^\circ$ ). The red lines are the best fit with the equation in Ref. 5 and the blue arrows indicate  $H_{shift}$ . The strength of the out-of-plane magnetic field  $H_z$  is 8 mT.

#### 4.2.2 Result.2 Angular Dependence of Asymmetric Magnetic DW Motion in Pt/Co/Pt, Pt/Co/AlO<sub>x</sub>, and Pt/Co/MgO

To check the generality, we prepare the 3 different PMA films: Pt/Co/Pt, Pt/Co/AlO<sub>x</sub>, and Pt/Co/MgO. Figure 4.3 shows that  $H_{shift}$  is also very sen-

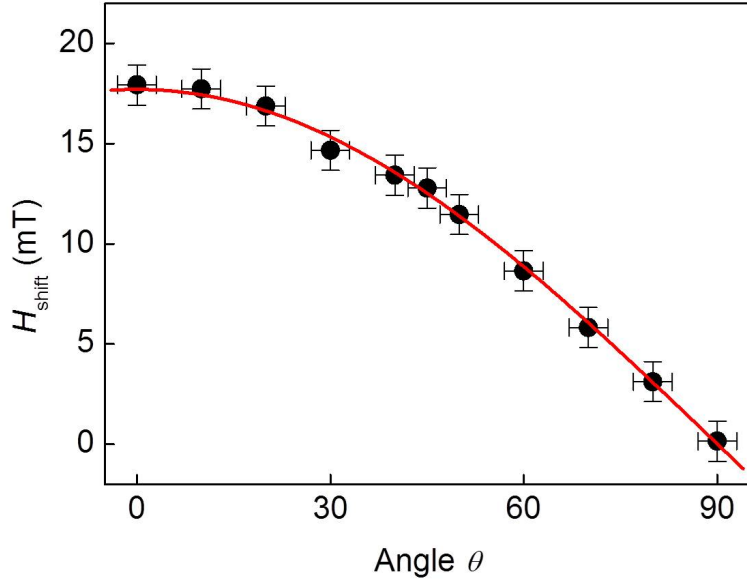


Figure 4.2 Measured  $H_{\text{shift}}$  with respect to  $\theta$ . The red line is the best fit with  $\cos \theta$ .

sitive to  $\theta$  for each sample. Especially, this method is also well-applied in Pt/Co/MgO with high symmetric-breaking along the z-direction with large DMI as shown in Fig. 4.3(c). So we demonstrate that the present idea (DMI meter 2.0) can be well-operated on other samples, where  $H_{DMI}$  is even much larger than the field-strength limit of equipment. Therefore we develop and demonstrate an advanced DMI meter based on asymmetric DW motion.

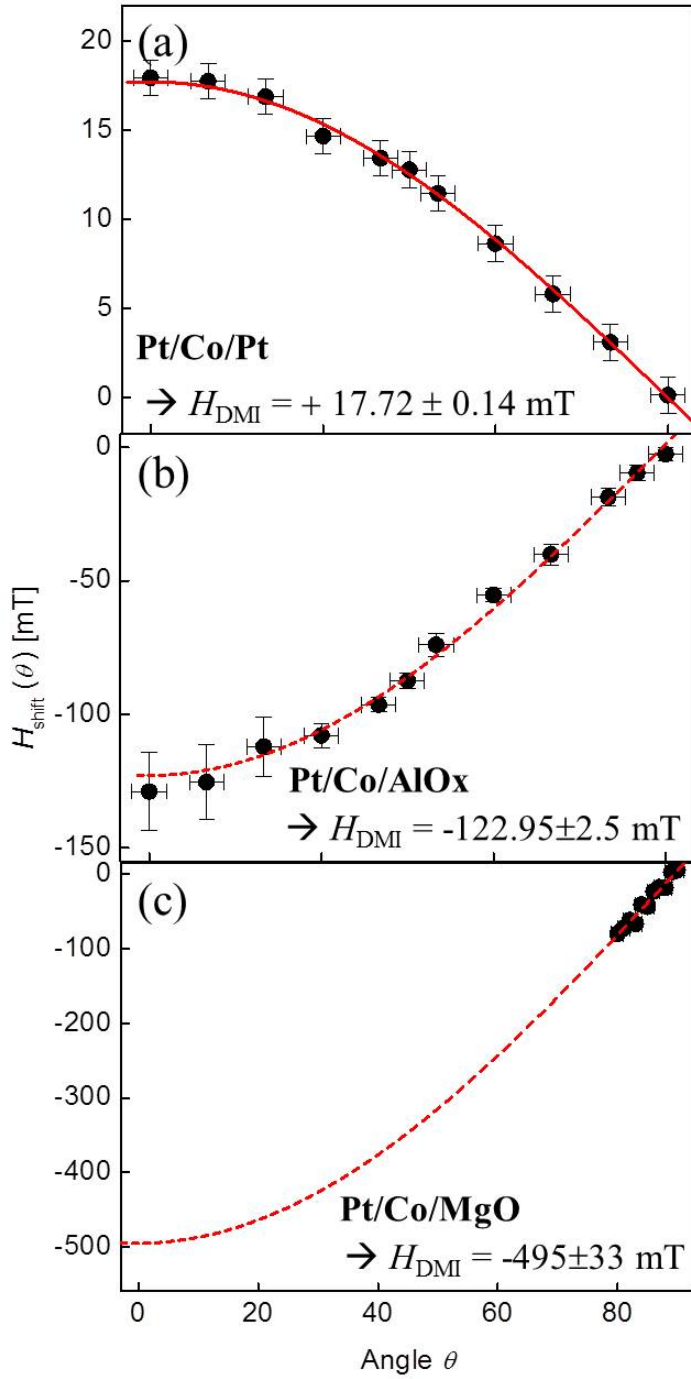


Figure 4.3 Measured  $H_{\text{shift}}$  with respect to  $\theta$  (a) Pt/Co/Pt, (b) Pt/Co/AlOx, and (c) Pt/Co/MgO. The red lines are the best fit with  $\cos \theta$ .

## Chapter 5

# Application Device: Magnetic Bubblecade Memory

### 5.1 Magnetic Bubblecade Memory based on Chiral Domain Walls

Unidirectional motion of magnetic domain walls is the key concept underlying next-generation domain-wall-mediated memory and logic devices. Such motion has been achieved either by injecting large electric currents into nanowires or by employing domain-wall tension induced by sophisticated structural modulation. Herein, we demonstrate a new scheme without any current injection or structural modulation. This scheme utilizes the recently discovered chiral domain walls, which exhibit asymmetry in their speed with respect to magnetic fields. Because of this asymmetry, an alternating magnetic field results in the coherent motion of the domain walls in one direction. Such coherent unidirectional motion is achieved even for an array of magnetic bubble domains, enabling the design of a new device prototype—magnetic bubblecade memory—with two-

dimensional data-storage capability.

### 5.1.1 Introduction

Recent progress in the control of magnetic domain walls (DWs) has suggested a number of prospective opportunities for next-generation DW-mediated devices [33],[34],[35],[36],[37]. Among these, coherent unidirectional DW motion has been proposed to replace the mechanical motion of magnetic media in hard-disk drives, thereby enabling the creation of a solid-state nonvolatile data-storage device—so-called racetrack memory—with high storage capacity, low power, and high mechanical stability[33]. Such coherent unidirectional motion was first achieved by injecting current into magnetic nanowires[36],[37],[38]. In this scheme, current-induced spin-transfer[38] and spin-orbit torques[39],[40] exert forces on DWs by transferring electron spins to the local magnetic moment, resulting in DW motion along the direction of force. It is therefore possible to realize the unidirectional motion of multiple DWs, leading to the recent development of DW shift registers[36],[37]. Such DW motion, however, requires a high threshold current, which is inevitably accompanied by high Joule heating that may cause severe artifacts. Structural modulation of the nanowires has therefore been proposed to reduce the threshold current by introducing DW tension[42]. With wedge-shaped modulation, the DW tension exerts a force on the DWs to reduce the tension energy and consequently, facilitates the DW motion toward the apex edge[43]. It has been revealed that periodic structural modulation allows DW-tension-induced unidirectional motion to be solely driven by the magnetic field without any current injection, as demonstrated by magnetic-ratchet shift registers[44]. It has also been demonstrated that vertical composition modulation leads to unidirectional DW motion along the vertical direction[45]. These schemes are, however, extremely sensitive to tiny

structural irregularities in the devices and thus, require highly sophisticated nanofabrication processes. The magnetic bubble memory[46] commercialized in 1970s also utilizes the unidirectional motion of magnetic bubble domains, but it requires tiny magnetic guide patterns onto the films to attract and repel the bubble domains under rotating magnetic field. Here, we demonstrate a new scheme for unidirectional DW motion based on skyrmion-like magnetic bubble domains[47]. This scheme is applicable even to unpatterned films in the absence of any current injection or structural modulation. The magnetic skyrmion[47],[48],[49],[50],[51],[52] is a topological object in which the internal spins whirl around the core in all directions and thus, shield the core spins from outer spins of the opposite orientation. Magnetic skyrmions have been observed in several helical magnets, where the helical spin alignment is caused by the Dzyaloshinskii-Moriya interaction (DMI)[53],[54]. Recently, it has been observed that metallic ferromagnetic multilayer films also exhibit finite DMI because of their asymmetric layer structure, resulting in skyrmion-like magnetic bubble domains with a Néel DW configuration[55],[56].

## 5.1.2 Sample Preparation & Experimental Methods

### Sample Preparation

For this study, metallic ferromagnetic Ta/Pt/Co/Pt films were deposited on Si substrates with 100-nm-thick SiO<sub>2</sub> layer by means of the dc-magnetron sputtering. The thicknesses of the Ta and Co layers are fixed to 5.0 and 0.3 nm, respectively, and the thicknesses of the upper and lower Pt layers are adjusted from 1.0 to 3.0 nm to tune the magnetic properties[63]. To enhance the sharpness of the layer interfaces, the films were deposited with a small deposition rate (0.25 Å/sec) through adjustment of the Ar sputtering pressure ( $\sim 2$  mTorr) and

power ( $\sim 10$  W). All the films exhibit clear circular domain expansion with weak pinning strength. The results in Figs. 2 and 3 were obtained from 5.0-nm Ta/2.5-nm Pt/0.3-nm Co/3.0-nm Pt film (Sample A) that shows the fastest bubble speed under the present experimental condition, possibly due to the weak coercive field (7.1 mT). The results in Fig. 4 were obtained from 5.0-nm Ta/2.5-nm Pt/0.3-nm Co/1.0-nm Pt film (Sample B) that allows regular bubble-array writing with small irregularities due to the relatively large coercive field (16.2 mT). The DMI-induced magnetic field  $H_{DMI}$  was measured to be 40 and 22 mT for Samples A and B, respectively, by analyzing the asymmetric DW motion[57],[58]. The DMI constant is then estimated to be about 0.3 and 0.1 mJ/m<sup>2</sup> for Samples A and B, respectively, by use of the saturation magnetization ( $1.3 \times 10^6$  A/m) measured by a vibrating sample magnetometer and the typical DW width (5 nm).

### **Experimental Setup and Procedure**

The magnetic domain images were observed by use of a magneto-optical Kerr effect (MOKE) microscope equipped with a charge-coupled device (CCD) camera on the focal plane[42]. To apply the magnetic field onto the films, two electromagnets and two small coils are attached to the sample stage. One of the electromagnets is used to apply the in-plane magnetic field bias up to 200 mT. The smallest coil ( $\sim 1$  mm in radius) is used to apply the out-of-plane magnetic field pulses up to 68 mT with a fast rising time ( $< 1 \mu\text{s}$ ). The combination of the in-plane electromagnet and the smallest coil was used to obtain the results shown in Fig. 2. The other coil ( $\sim 2$  mm in radius) is designed to apply the alternating sinusoidal magnetic field with adjustable tilting angle, which was used to obtain the results shown in Fig. 3. For field uniformity over the wide range ( $> 2$  mm) of the film, two electromagnets were used to apply the in-plane

and out-of-plane magnetic fields to obtain the results shown in Fig. 4.

### **Thermomagnetic Writing of Bubble Domains**

To create bubble domains, the thermomagnetic writing scheme[64],[66] is adopted. In this scheme, the magnetization of the film is first saturated by applying an out-of-plane magnetic field pulse ( $-30$  mT, 1 s). A laser beam (60 mW) is then focused on a small spot ( $\sim 1$   $\mu\text{m}$  in diameter) of the film, causing reduction of the coercive field inside the spot by increasing the temperature. At this instant, a reversed magnetic field pulse (8 mT, 12 ms) is applied. Since the strength of the reversed magnetic field is adjusted to be slightly larger than the reduced coercive field inside the spot, the magnetization reversal occurs only in the area of the spot. Consequently, a bubble-shaped reversed domain is created. By repeating this procedure with motorized sample stage, arbitrary pattern of bubble domain array can be recorded. Due to the time delay for multiple-bubble recording with stage translation, the clock pulses were interleaved in the present demonstration of the magnetic bubblecade memory operation shown in Fig. 4f. The spin-transfer torque scheme with multiple nanopillar structures will possibly provide a parallel writing capability required for real-time device operation.

#### **5.1.3 Result.1: Single Bubble Motion**

We demonstrate that a sequence of applying magnetic fields leads to a unidirectional motion of magnetic bubble domains. Figure 1a illustrates a skyrmion-like bubble domain with a Néel DW configuration, where the magnetization  $\hat{m}_{DW}$  (red arrows) inside the DW is oriented radially outward in all directions. Because of the rotational symmetry with respect to the center of the bubble, the present bubble expands or shrinks circularly under an out-of-plane magnetic

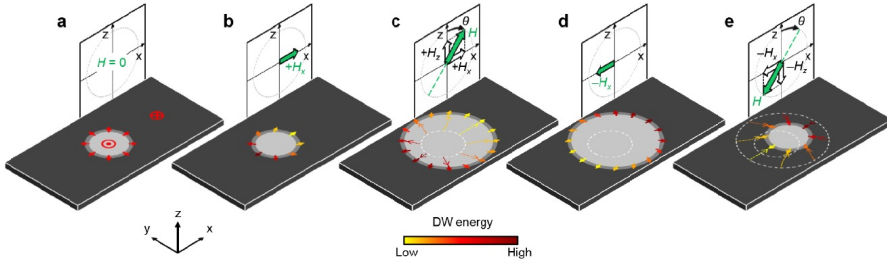


Figure 5.1 Schematic descriptions of the unidirectional bubble motion. (a) Illustration of a bubble domain (bright circle) and the DW (grey ring), surrounded by a domain of opposite magnetization (dark area). The red symbols and arrows indicate the direction of the magnetization inside the DW and domains. (b) Asymmetric DW-energy distribution under an in-plane magnetic field  $+H_x$  (green arrow), as visualized by the color contrast of the arrows on the DW according to the scale bar at the bottom. (c) Asymmetric DW expansion under a magnetic field  $H(= (+H_x, +H_z))$  with a tilting angle  $\theta$ . (d) Asymmetric DW-energy distribution under the reversed in-plane magnetic field  $-H_x$ . (e) Asymmetric DW shrinkage under the reversed magnetic field  $(-H_x, -H_z)$ . The dashed circles represent the previous DW positions.

field  $H_z$  (Ref. [42]). However, if one applies an in-plane magnetic field  $H_x$ ,  $\hat{m}_{DW}$  becomes tilted to the direction of  $H_x$  due to the Zeeman interaction as illustrated by the arrows in Fig. 1b and thus, the rotational symmetry is broken since  $\hat{m}_{DW}$  is not oriented radially outward in all directions. The different angle between  $\hat{m}_{DW}$  and  $H_x$  then results in different Zeeman energy contribution to the DW energy: the parallel alignment has a lower DW energy, whereas the antiparallel alignment has a higher DW energy. Such asymmetric DW energy distribution is shown by the color contrast of the arrow in Fig. 1b. This bubble domain then exhibits asymmetric expansion under  $H_z$  (Fig. 1c) because the

DW speed depends on the DW energy[57],[58],[59]. At this instant, if one reverses the polarity of the in-plane magnetic field (i.e., applies  $-H_x$ ), then the asymmetry in the DW-energy distribution is also reversed (Fig. 1d). With applying  $-H_z$ , this bubble domain shrinks toward a different location from the original position of the domain (Fig. 1e). Consequently, the center of the bubble shifts along the x axis from the original position. Such a shift of the center can be continuously generated along the same direction by repeating the process illustrated in Figs. 1c and e, in which collinear magnetic fields  $(+H_x, +H_z)$  and  $(-H_x, -H_z)$  are alternately applied. Therefore, unidirectional bubble motion can be achieved by applying an alternating magnetic field generated by a single coil that is tilted by an angle  $\theta(=\text{atan}(H_x/H_z))$  to the film normal.

The predicted behavior discussed above can be readily verified for Pt/Co/Pt films (see Supplementary Information 1). Recent studies have revealed that these films have a positive DMI and thus exhibit the right-handed chiral DW configuration[57],[58]. Figure 2a presents an image of a bubble domain captured using a magneto-optical Kerr effect (MOKE) microscope (Ref. [42] and see Supplementary Information 2). Because of the right-handed chirality,  $\hat{m}_{DW}$  is expected to be oriented outward, as illustrated in the inset. By applying an alternating magnetic field to this bubble domain, unidirectional bubble motion was successfully accomplished, as seen in Figs. 2a-c. The exact conformity of these images with Fig. 1 proves the principle of the present scheme.

#### 5.1.4 Result.2: Speed of Bubble Motion

The speed  $V_B$  of the bubble motion follows the average rate of DW motion under the alternating magnetic-field pulses. The forward and backward motions of the DW (blue arrows in Figs. 2b and c) yield the relation  $V_B=[V_{\parallel}(H_z, H_x)+V_{\parallel}(-H_z, -H_x)]/2$ , where  $V_{\parallel}$  is the DW speed at the rightmost point of the bubble[56].

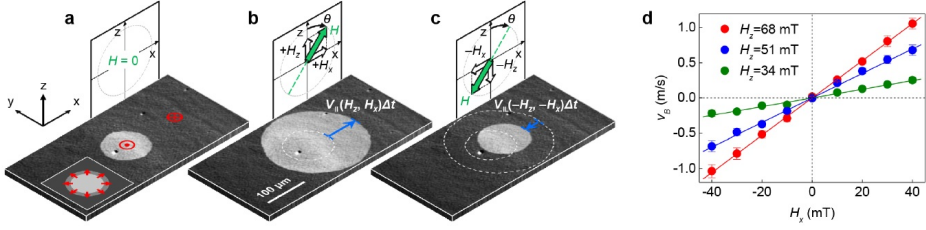


Figure 5.2 Experimental verification of the unidirectional bubble motion from Pt/Co/Pt film. (a) MOKE image of the initial bubble domain (bright circle) surrounded by a domain of opposite magnetization (dark area). The red symbols indicate the direction of the magnetization in the domains. The inset illustrates the expected  $\hat{m}_{DW}$  (red arrows) in the right-handed chiral DW configuration. (b) The expanded bubble domain after application of a  $(+H_x, +H_z)$  pulse ( $H_x=30$  mT,  $H_z=4$  mT,  $\Delta t=100$  ms), where  $\Delta t$  is the pulse duration time. The blue arrow indicates the DW displacement  $V_{\parallel}(H_z, H_x)\Delta t$ . The dashed circle represents the initial DW position. (c) The shrunken bubble domain after application of a  $(-H_x, -H_z)$  pulse. The blue arrow indicates the DW displacement  $V_{\parallel}(-H_z, -H_x)\Delta t$ . The dashed circles represent the previous DW positions. (d) Measured  $V_B$  with respect to  $H_x$  for several  $H_z$ . The error bars correspond to the standard deviation from data obtained by sampling 10 times.

The measured  $V_B$  is plotted with respect to  $H_x$  for several  $H_z$  (Fig. 2d). This plot clearly demonstrates that  $V_B$  is proportional to  $H_x$  within the experimental range of  $H_x$ , yielding the expression  $V_B\rho_1(H_z)H_x$  (see Supplementary Information 3). According to Ref. [57], the coefficient  $\rho_1(H_z)$  is given by  $C_1\ln[V_0/|V_{\parallel}(H_{z,0})|]V_{\parallel}(H_{z,0})$  in the DW creep regime[60][61], where  $C_1$  is a constant related to the Zeeman contribution to the DW energy and  $V_0$  is the characteristic speed. In the present sample,  $C_1\ln[V_0/|V_{\parallel}(H_{z,0})|]$  is estimated to be

approximately  $(86 \text{ mT})^{-1}$  for the maximum  $H_z$  (68 mT) from the present coil and thus, a  $V_B$  ( $=1 \text{ m/s}$ ) is achieved up to approximately 46% of  $V_{\parallel}(H_{z,0})$  ( $=2.2 \text{ m/s}$ ) under the maximum  $H_x$  (40 mT).

### 5.1.5 Result.3: Bubble Radius Variation

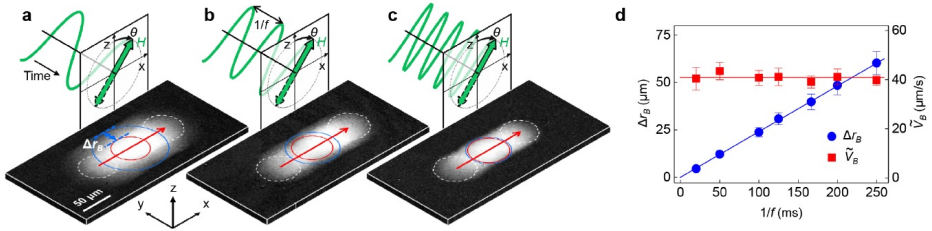


Figure 5.3 Frequency dependence of bubble motions. Accumulated MOKE images acquired during bubble motion for various  $f$  values, 10 Hz (a), 20 Hz (b), and 50 Hz (c), respectively. Alternating sinusoidal magnetic field was applied with an amplitude 3.7 mT and a tilting angle  $34^\circ$ , and the accumulation time was fixed to 3 s for all images. The red (blue) circle represents the smallest (largest) bubble observed during the motion. The blue arrows indicate  $\Delta r_B$  between the largest and smallest bubbles. The red arrows indicate the displacement of the bubble center between the initial and final positions (white dashed circles) over the accumulation time.  $\tilde{V}_B$  is then determined by the ratio of the displacement over the accumulation time. Since these images were captured over the same accumulation time, almost the same displacements indicate that  $\tilde{V}_B$  nearly unchanged irrespective of  $f$ . (d), Measured  $\Delta r_B$  and  $\tilde{V}_B$  values with respect to  $f$ . The error bars correspond to the standard deviation from data obtained by sampling 10 times.

The variation  $\Delta r_B$  in the radius of the bubble during its motion can be controlled by adjusting the frequency  $f$  of the alternating magnetic field. Fig-

ures 3a-c present images of the bubble motion driven by alternating sinusoidal magnetic field with  $f= 10$  Hz (a), 20 Hz (b), and 50 Hz (c), respectively. Note that each image was accumulated over a period of 3 s during bubble motion and thus, the length (red arrow) of the gray area represents the bubble displacement during the image-accumulation time. Additionally, the width (blue arrow) of the light-gray boundary represents  $\Delta r_B$  between the smallest (red circle) and largest (blue circle) bubbles. Figure 3d provides a plot of the measured  $\Delta r_B$  and the average bubble speed  $\tilde{V}_B$  values with respect to  $f$ . The figure clearly demonstrates that  $\Delta r_B$  is inversely proportional to  $f$ . Because  $\tilde{V}_B$  remains nearly unchanged irrespective of  $f$ , one can independently reduce  $\Delta r_B$  down to the limiting value defined by the bandwidth of the coil without changing  $\tilde{V}_B$ .

#### 5.1.6 Result.4: Bubblecade and Memory Operation

Finally, the present scheme was applied to a two-dimensional bubble array. For this purpose, an arbitrary  $5 \times 5$  array pattern of bubbles (Fig. 4a) was initially created on the film using the thermomagnetic writing method (see Supplementary Information 4). Under the application of alternating magnetic pulses, all bubbles exhibited coherent unidirectional motion, as shown by the image (Figs. 4b-e and see Supplementary Movie 1) captured during the pulses. Exactly the same bubble-array pattern was maintained even after traveling more than 1 mm (Fig. 4e). Therefore, the observed two-dimensional coherent unidirectional motion of the bubbles—hereafter referred to as the bubblecade—can be used to replace the mechanical motion of the magnetic media with respect to read and write sensors, enabling a new device prototype ‘magnetic bubblecade memory.’

The writing and reading operation schemes of bubblecade memory are also demonstrated. Figure 4f illustrates the operation timetable for a 4-bit magnetic

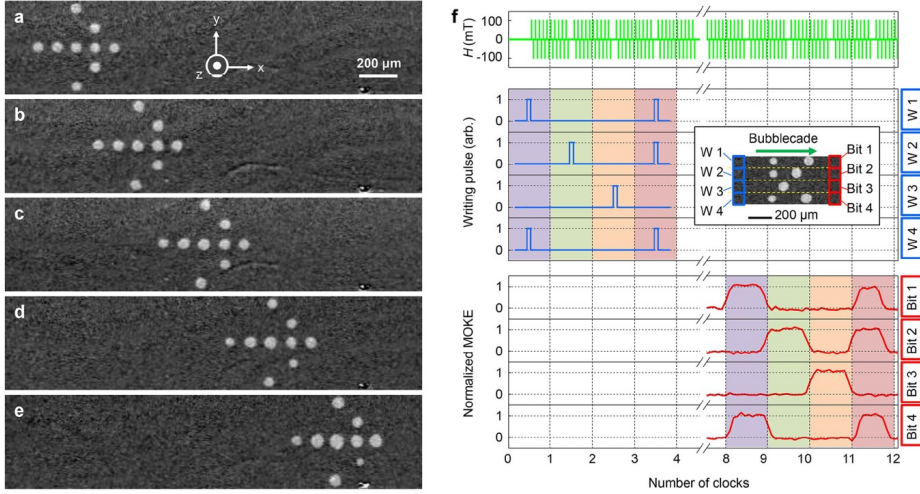


Figure 5.4 Experimental demonstration of ‘bubblecade’, the two-dimensional coherent unidirectional motion of multiple bubbles. MOKE images of an arbitrary  $5 \times 5$  array of bubbles, (a) initially written on the leftmost side of the film and taken after application of (b) 32, (c) 64, (d) 96, and (e) 127 pulse sets. Each pulse set is composed of alternating square magnetic field pulses ( $H = \pm 106$  mT,  $\theta = 71^\circ$ ,  $\Delta t = 20$  ms). (f) The operation timetable of 4-bit magnetic bubblecade memory. The top panel presents the alternating magnetic field pulses ( $H = \pm 106$  mT,  $\theta = 71^\circ$ ,  $\Delta t = 20$  ms) that act as the operation clock. The next four panels show the pulses for the thermomagnetic writing of the bubbles on each bit in the writing section. The last four panels show the signals from the CCD pixels corresponding to each bit of the reading section. The inset presents the device structure, with the writing (blue box) and reading (red box) sections indicated.

bubblecade memory. The top panel shows the alternating magnetic pulses that act as the operation clock. The next four panels specify the bubble-writing pulses (see Supplementary Information 4), which are applied to each bit of the writing section (blue box) of the device depicted in the inset. At present, bubble writing is achieved using the thermomagnetic writing scheme, but it may also be possible to implement using the spin-transfer torque writing scheme with a nanopillar structure[50]. The bottom four panels illustrate the reading signal from each bit of the reading section (red box) of the device. At present, the reading signals are detected by the corresponding pixels of a charge-coupled device (CCD) camera, but it may also be possible to read out these signals using tunneling magnetoresistive sensors in the future[62]. The figure clearly shows that all written two-dimensional data bits are successively retrieved from the reading section, demonstrating shift-register-based memory operation (see Supplementary Movie 2).

### 5.1.7 Discussion & Conclusions

Further optimizing the design of the coils will enhance the operation speed of the magnetic bubblecade memory, because the present maximum of the bubblecade speed is not limited by the sample. Since it is possible to achieve the bubblecade speed to be about a half of the DW speed and the DW speed has been demonstrated to reach a few hundreds m/s (refs [36],[38]), it is expected to achieve the speed compatible to the practical operations with elaborated design of microcoils. The data rate is then governed by the bubblecade speed and the storage density. Recent discovery of the skyrmion crystals signals the possibility to enhance the storage density of the present scheme up to the packing density of the skyrmions in the skyrmion lattice[51], which is possibly optimized to be larger than a few hundreds of Gbits/in<sup>2</sup> with the typical skyrmion size

smaller than a few tens of nm (ref. [50]). Furthermore, the two-dimensional bubble operation on unpatterned films enhances the compatibility toward the three-dimensional data storage by stacking the films. For better scalability, the stray-field-induced crosstalk and the size-dependence of the bubble speed have to be further investigated by exploring the proper materials and layer combination[63] including the antiferromagnetically coupled layer structures. In summary, we present here a proof-of-principle experiment demonstrating the two-dimensional coherent unidirectional motion of multiple bubble domains, of which the speed is a significant fraction of the DW speed. Such bubble motion is attributed to the helical magnetic configuration caused by the asymmetric layer structure and therefore, further exploration of materials and layer combinations[63] together with the optimization of the coil design will further enhance the potential of this technology for various applications. The present scheme can eliminate the necessity for the mechanical motion of the media in hard-disk drives and thus, enables the development of a new prototype solid-state data-storage device, so-called the magnetic bubblecade memory.

## 5.2 Magnetic Bubblecade Motion in Creep Regime

By adopting the Taylor expansion with respect to  $H_x$ , the DW speed  $V_{\parallel}$  at the rightmost point of the bubble domain can be written as,

$$V_{\parallel}(H_z, H_x) = V_{\parallel}(H_z, 0) + \sum_{n=1}^{\infty} \rho_n(H_z) H_x^n, \quad (5.1)$$

where  $\rho_n(H_z) \equiv \frac{1}{n!} \frac{\partial^n V_{\parallel}(H_z, H_x)}{\partial H_x^n} \Big|_{H_x=0}$ . Since  $V_{\parallel}$  is an odd function with respect to  $H_x$ ,  $V_{\parallel}(-H_z, -H_x)$  is equal to  $-V_{\parallel}(H_z, -H_x)$  i.e.

$$V_{\parallel}(-H_z, -H_x) = -V_{\parallel}(H_z, 0) - \sum_{n=1}^{\infty} \rho_n(H_z) (-H_x)^n, \quad (5.2)$$

From the relation  $V_B=[V_{\parallel}(H_z,H_x)+V_{\parallel}(-H_z,-H_x)]/2$ , the speed  $V_B$  of the bubble motion can be thus expressed as

$$V_B(H_z, H_x) = \sum_{n=0}^{\infty} \rho_{2n+1}(H_z) H_x^{2n+1}, \quad (5.3)$$

The experimental observation (Fig. 2d) indicates that it is good enough to approximate Eq. (5.3) as

$$V_B(H_z, H_x) \cong \rho_1(H_z) H_x, \quad (5.4)$$

within the present experimental range of  $H_x$ , by confirming that the higher-order terms are negligible compared to the linear term.

According to Ref. 25, the DW energy density  $\sigma_{DW}$  is given by a function of  $H_x$  as

$$\sigma_{DW} = \begin{cases} \sigma_0 - \frac{\pi\lambda M_S}{2H_D} (H_x + H_{DMI})^2 & \text{for } |H_x + H_{DMI}| < H_D \\ \sigma_0 + 2K_D\lambda - \pi\lambda M_S |H_x + H_{DMI}| & \text{otherwise} \end{cases}, \quad (5.5)$$

where  $\sigma_0$  is the DW energy of the Bloch configuration,  $\lambda$  is the DW width,  $M_S$  is the saturation magnetization, and  $H_{DMI}$  is the DMI-induced effective magnetic field. Here,  $H_D (\equiv 4K_D/\pi M_S)$  is the DW anisotropy field that is required to rotate  $\hat{m}_{DW}$  from the Bloch configuration to the Néel configuration, where  $K_D$  is the DW anisotropy constant. Based on the assumption that the dependence of  $V_{\parallel}$  on  $H_x$  is solely attributed to the variation of  $\sigma_{DW}$  due to  $H_x$ , one finds the relation

$$\rho_1 \equiv \left. \frac{\partial V_{\parallel}}{\partial H_x} \right|_{H_x=0} = \left. \frac{\partial V_{\parallel}}{\partial \sigma_{DW}} \right|_{\sigma_{DW}=\sigma_{DW}(0)} \cdot \left. \frac{\partial \sigma_{DW}}{\partial H_x} \right|_{H_x=0}, \quad (5.6)$$

which is then written as

$$\rho_1 = \begin{cases} -\pi\lambda M_S \frac{H_{DMI}}{H_D} \left. \frac{\partial V_{\parallel}}{\partial \sigma_{DW}} \right|_{\sigma_{DW}=\sigma_{DW}(0)} & \text{for } |H_{DMI}| < H_D \\ -\pi\lambda M_S \text{sgn}(H_{DMI}) \left. \frac{\partial V_{\parallel}}{\partial \sigma_{DW}} \right|_{\sigma_{DW}=\sigma_{DW}(0)} & \text{otherwise} \end{cases}, \quad (5.7)$$

In the creep regime,  $V_{\parallel}$  follows the creep scaling law  $V_{\parallel}(H_z, H_x) = V_0 \exp[-\alpha(H_x)H_z^{-1/4}]$ , where  $V_0$  is a characteristic speed and  $\alpha$  is a constant related to the scaling energy constant, the critical magnetic field, and the thermal fluctuation energy[S1]. By use of the relation  $\alpha(H_x) \propto [\sigma_{DW}(H_x)]^{1/4}$  proposed in Refs. 25 and 26, one finds the relation

$$\left. \frac{\partial V_{\parallel}}{\partial \sigma_{DW}} \right|_{\sigma_{DW}=\sigma_{DW}(0)} = \frac{1}{4\sigma_{DW}(0)} V_{\parallel}(H_z, 0) \ln \left( \frac{V_0}{|V_{\parallel}(H_z, 0)|} \right). \quad (5.8)$$

Since  $|H_{DMI}| > H_D$  in the present Pt/Co/Pt films as demonstrated in Ref. 11 and  $H_{DMI} > 0$  in the present experimental condition,  $V_B$  can be finally written as

$$V_B(H_z, H_x) \cong C_1 \ln \left( \frac{V_0}{|V_{\parallel}(H_z, 0)|} \right) V_{\parallel}(H_z, 0) H_x, \quad (5.9)$$

where  $C_1 \cong \frac{\pi \lambda M_S}{4\sigma_{DW}(0)} \text{sgn}(H_{DMI})$ .

For alternating sinusoidal magnetic field  $(H_z \sin \omega t, H_x \sin \omega t)$ , the average speed  $\tilde{V}_B$  of the bubble motion can be written by

$$\tilde{V}_B(H_z, H_x) \cong \frac{C_1 \omega}{\pi} \int_0^{\pi/\omega} \ln \left( \frac{V_0}{|V_{\parallel}(H_z \sin \omega t, 0)|} \right) V_{\parallel}(H_z \sin \omega t, 0) H_x \sin \omega t dt, \quad (5.10)$$

$$\tilde{V}_B(H_z, H_x) \cong C_2 V_B(H_z, H_x), \quad (5.11)$$

where  $C_2 = \frac{1}{\pi} \int_0^{\pi} \exp \left[ \ln \left( \frac{V_0}{|V_{\parallel}(H_z, 0)|} \right) (1 - (\sin \tau)^{1/4}) \right] (\sin \tau)^{3/4} d\tau$ . Numerical evaluation reveals that  $C_2$  is a slowly-varying function of  $V_{\parallel}(H_z, 0)$  within the range from 0.3 (for  $V_{\parallel}(H_z, 0) \cong 1$  mm/s) to 0.5 (for  $V_{\parallel}(H_z, 0) \cong 100$  m/s) in the present samples.

According to Eq. (5.9), the direction of the bubble motion i.e.  $\text{sgn}(V_B)$  is given as

$$\text{sgn}(V_B) = \text{sgn}(H_{DMI} V_{\parallel}(H_z, 0) H_x). \quad (5.12)$$

Since the direction of  $V_{\parallel}$  is determined by the relative alignment of the out-plane magnetic field  $H_z$  with respect to the out-of-plane component  $m_z^{\text{bubble}}$  of

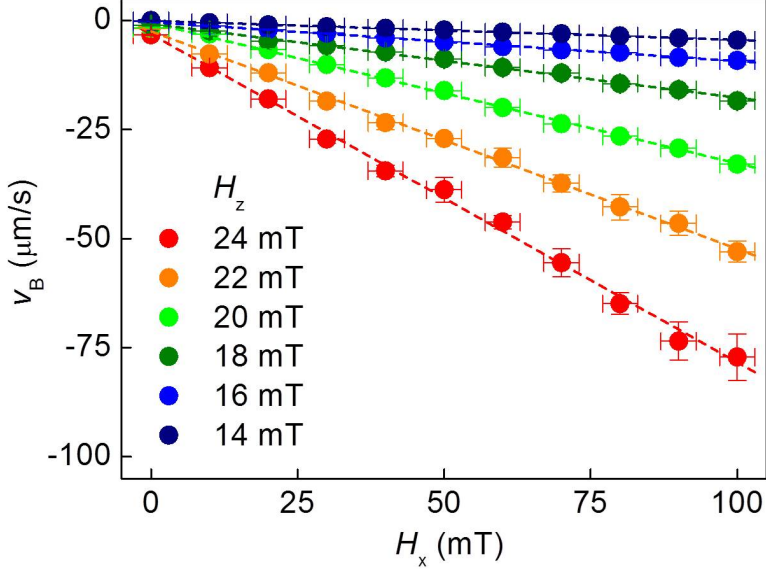


Figure 5.5  $V_B$  in Pt/Co/MgO film, with respect to  $H_x$  for several  $H_z$ . The inset illustrates the expected  $\hat{m}_{DW}$  (red arrows) with the left-handed chiral DW configuration. The dashed lines show the best linear fit from Eq. (S9).

the magnetization inside the bubble domain, one can replace  $\text{sgn}(V_{\parallel}(H_z, 0))$  by  $\text{sgn}(m_z^{bubble} H_z)$ . Then,  $\text{sgn}(V_B)$  can be rearranged as

$$\text{sgn}(V_B) = \text{sgn}(\kappa_{DMI}) \cdot \text{sgn}(\theta), \quad (5.13)$$

where the DW chirality  $\kappa_{DMI}$  is defined by  $H_{DMI} m_z^{bubble}$  inside the DW at the rightmost point of the bubble domain and the tilting angle  $\theta$  of the magnetic field is defined by  $\text{atan}(H_x/H_z)$ .

We confirmed the dependence on  $\text{sgn}(\theta)$  by a repeated experiment with opposite sign of  $\theta$  (not shown). Such dependence on  $\text{sgn}(\theta)$  can be also verified even in the present experimental results, by rotating the observation coordinate by

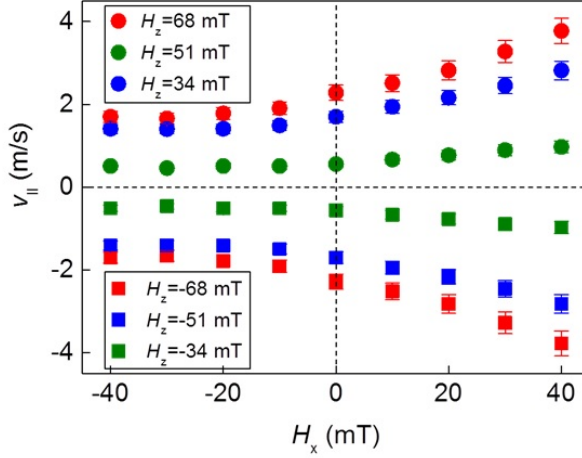


Figure 5.6 Asymmetric DW speed  $V_{\parallel}$  with respect to  $H_x$  for several  $H_z$ . Data were obtained under the same condition employed to measure Fig. 2d. The asymmetry with respect to  $H_x$  is known to be caused by a finite DMI[25,26]. For the condition (with  $H_z=68$  mT and  $H_x=40$  mT) of the maximum  $V_B$  shown in Fig. 2d, the forward and backward DW speeds are measured as  $V_{\parallel}(H_z, H_x)=3.7$  m/s and  $V_{\parallel}(-H_z, -H_x)=-V_{\parallel}(H_z, -H_x)=-1.6$  m/s. These speeds are accordant to the measured maximum  $V_B(=1$  m/s) in Fig. 2d via the relation  $V_B = [V_{\parallel}(H_z, H_x) + V_{\parallel}(-H_z, -H_x)]/2$ . This maximum  $V_B$  is approximately 46% of  $V_{\parallel}(H_z, 0)(=2.2$  m/s).

180 degree with respect to the z axis. On the other hand, to confirm the dependence on  $\kappa_{DMI}$ , we repeated the experiment by use of Pt/Co/MgO films that are known to have the left-handed chirality[S2], opposite to the right-handed chirality in the Pt/Co/Pt films[25,26]. Figure [S1] summarizes the results from the Pt/Co/MgO films. The results truly show that the direction of the bubble motion in the Pt/Co/MgO films is opposite to that of the Pt/Co/Pt films (Fig. 2), verifying Eq. (S12).

### 5.3 Optimization of Magnetic Bubblecade Speed via Strength and Angle of Magnetic Field Adjustments

Unidirectional coherent motion of magnetic domain walls (DWs) is one of the key factors for the next-generation promising memory and logic devices. Many concepts have been suggested and demonstrated by either injection of electric current into nanowires, structural modulation to induce the DW tension, or application of oscillating magnetic field to induce magnetic bubblecade [67]. Among these schemes, the magnetic bubblecade memory has been recently demonstrated [67], as shown by Fig. 5.4. In the operation of the magnetic bubblecade memory, two major control factors were found to play the decisive role in determination of the bubblecade speed  $v$ : strength  $H$  and tilting angle  $\theta$  of the magnetic field. Here, we examined the relation of  $v$  with respect to  $H$  and  $\theta$ . For this study, we prepared the 2.5-nm Pt/0.3-nm Co/1.0-nm Pt with perpendicular magnetic anisotropy film. Then,  $v$  was measured by use of a magneto-optical Kerr effect microscope. Figure 5.7 shows  $v$  versus  $\theta$  for various  $H$ . The figure clearly shows that  $v$  shows the maximum value at a critical angle  $\theta_c$  for a given  $H$ , where  $\theta_c$  slightly depends on  $H$ . A theory based on the DW creep criticality successfully explains the relation between  $\theta_c$  and  $H$ , as shown by the solid lines in the figure 5.8. The proposed analytic equation thus offers the way to predict the optimization condition of  $H$  and  $\theta$  for the maximum bubblecade speed in the operation of the magnetic bubblecade memory.

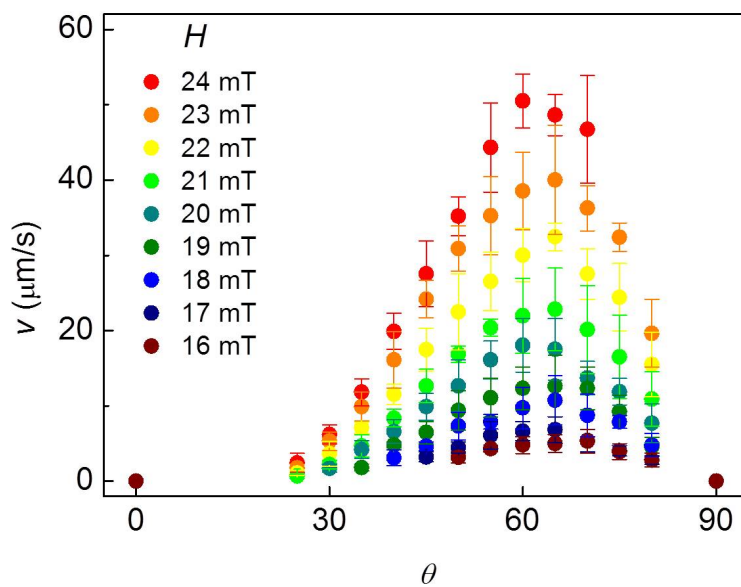


Figure 5.7 Bubble speed  $v$  with respect to the tilting angle of the magnetic field  $\theta$  for various field strength  $H$

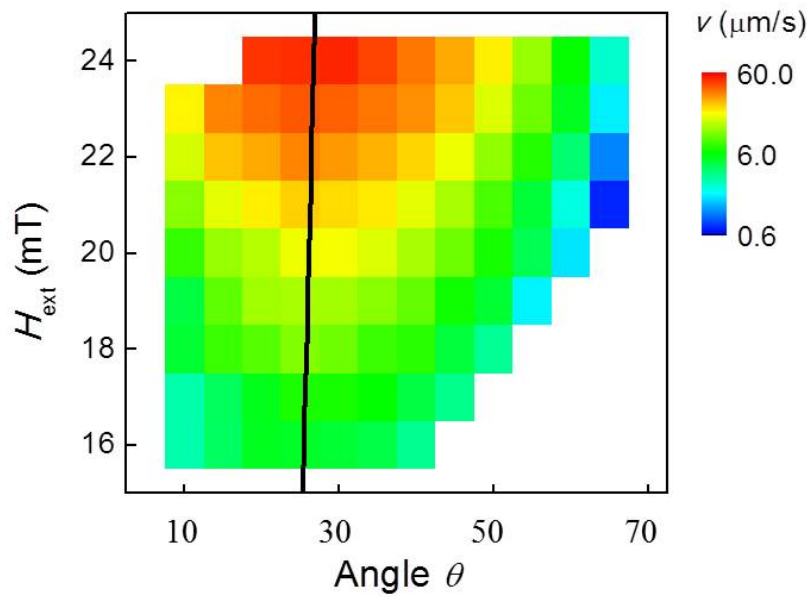


Figure 5.8 2 dimensional Bubble speed  $v$  with respect to the tilting angle of the magnetic field  $\theta$  and field strength  $H_{\text{ext}}$

## Chapter 6

# Temperature Dependence of DW Motion in Creep Regime

### 6.1 A Method for Compensating the Joule-Heating Effects in Current-Induced Domain Wall Motion

We propose here a method for compensating the Joule-heating effects in the current-induced domain wall motion (CIDWM). In CIDWM experiments, the current induces not only the spin-transfer torque (STT) effects but also the Joule-heating effects, and both effects influence the domain wall (DW) motion. It is thus desired to develop a way to compensate the Joule-heating effects, in order to determine the pure STT effects on the DW motion. Up to now, in studies of DW creeping motions, such Joule-heating effects have been eliminated based on the Arrhenius law by assuming the temperature-independent creep scaling constants. However, here we find that such scaling constants are sensitive to the temperature, from the DW creeping experiment in Pt/Co/Pt wires with temperature control in a cryostat. By accounting the temperature dependence

of the scaling constants, we demonstrate that all the DW speeds with various temperatures exactly collapse onto a single universal curve, which enables us to examine the pure STT effects on the DW motion.

### 6.1.1 Introduction

Current-induced domain wall motion (CIDWM) has been extensively studied nowadays, motivated by perspective application opportunities with abundant interesting physics [68],[69],[70],[71],[72]. Such CIDWM occurs through the spin-transfer torque (STT) effects between conduction electron spins and local magnetic moments [73],[74],[75]. For a small current, the CIDWM exhibits creeping motions [76], [77], of which the speed  $v$  follows the Arrhenius-type criticality as

$$v = v_0 \exp\left[-\frac{\alpha}{k_B T} H^{*-1/4}\right], \quad (6.1)$$

where  $v_0$  is the characteristic speed,  $\alpha$  is a constant related with the domain wall pinning energy,  $k_B$  is the Boltzmann constant, and  $T$  is the temperature. Here,  $H^*$  denotes the effective field caused by the current and magnetic field [78]. In such CIDWM, the current also induces the temperature rise due to the Joule heating, which makes it hard to resolve the pure STT effects [77],[79],[80]. Up to now, the temperature rise effects in the  $k_B T$  part have been compensated within the context of the Arrhenius law by assuming that  $v_0$  and  $\alpha$  are constant irrespective of  $T$  [77],[81],[82]. Such assumption has been used in a recent experiment on Pt/Co/Pt nanowires [77], where the temperature dependence of  $v_0$  and  $\alpha$  is ignorable due to a small temperature rise. However, for a large temperature range, it is essential to include the temperature dependence of  $v_0$  and  $\alpha$ . In this study, we propose a method to compensate the Joule-heating effects in the CIDWM with the temperature dependence of  $v_0$  and  $\alpha$ .

## 6.1.2 Sample Preparation & Experimental Methods

### Sample Preparation

For this study, metallic ferromagnetic Ta(5.0 nm)/Pt(2.0 nm)/Co(0.3 nm)/Pt(1.0 nm) films are prepared onto a 100-nm-thick SiO<sub>2</sub> layer on a Si wafer by dc-magnetron sputtering. The film exhibits a perpendicular magnetic anisotropy. By adopting a photolithography technique, magnetic wire structures with 5.0  $\mu\text{m}$  in width and 500  $\mu\text{m}$  in length are patterned. Then, 100-nm-thick Au electrodes are stacked onto both ends of the wire structure for current injection.

### Experimental Methods

The domain images are monitored by a magneto-optical Kerr effect (MOKE) microscope which has the field of view (200  $\mu\text{m} \times 150 \mu\text{m}$ ). The microscope is equipped with an electromagnet that produces a magnetic field up to 0.2 T by use of a bipolar power supply (Kepco 50-4M), as well as equipped with a current source (Keithley 6221) to inject the current up to a few  $10^{11}$  A/m<sup>2</sup> in dc. The current density  $J$  through the wire is estimated by the relation  $J=I/wt_f$ , where  $I$  is the current,  $w$  is the wire width (5  $\mu\text{m}$ ), and  $t_f$  is the total film thickness (8.3 nm). A cryostat is employed to control the temperature between the liquid helium temperature and 500 K.

Figure 6.1 shows the MOKE images of field-driven domain wall (DW) motion. A DW is initially created by the thermomagnetic writing scheme [82] with a 658-nm laser. To create a DW, the film is first saturated by a magnetic field (10 mT) and then, a laser beam (75 mW) is focused onto a small spot (5  $\mu\text{m}$  in diameter) on the wire under a reversed magnetic field (−1.6 mT) smaller than the coercive field (−8.1 mT). Once a DW is formed, the DW is pushed to a side by applying current and/or magnetic field. Each image in Fig. 6.1 is taken at

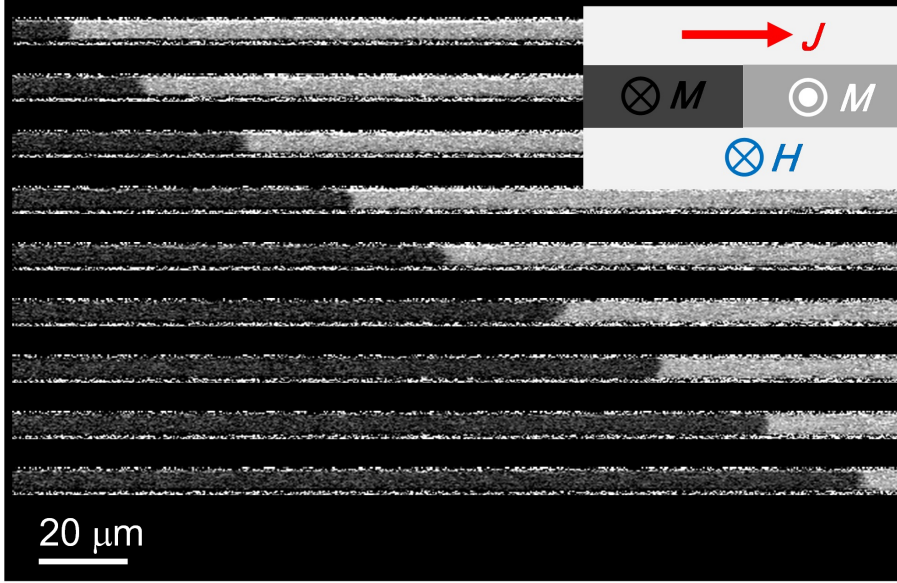


Figure 6.1 Sequential images of the DW motion measured by the MOKE microscope with a constant time step (700 ms). The directions of the current density  $J$ , the magnetic field  $H$ , and the magnetization  $M$  are denoted in the inset.

successive times with a constant time step (700 ms) under an external magnetic field ( $-3.75$  mT). It is clearly seen from the figure that the magnetic domain expands linearly with time.

The wire temperature is estimated by the temperature dependence of the electric resistivity [83]. In this method, the resistivity  $\rho$  of the wires is measured with respect to the current density  $J$  as shown by Fig. 6.2(a). Due to the Joule heating, the resistivity exhibits a quadratic dependence on  $J$  as shown by the best quadratic fit (solid line) with the equation  $\rho/\rho_0=1+\sigma_J J^2$ , where  $\rho_0$  is the resistivity at the ambient temperature  $T_0$  (297.3 K) and  $\sigma_J$  is a proportionality constant. The measured resistivity is converted to the temperature rise  $\Delta T$  by use of the relation  $\rho/\rho_0=1+\sigma_T \Delta T$  with another proportionality constant  $\Delta T$ ,

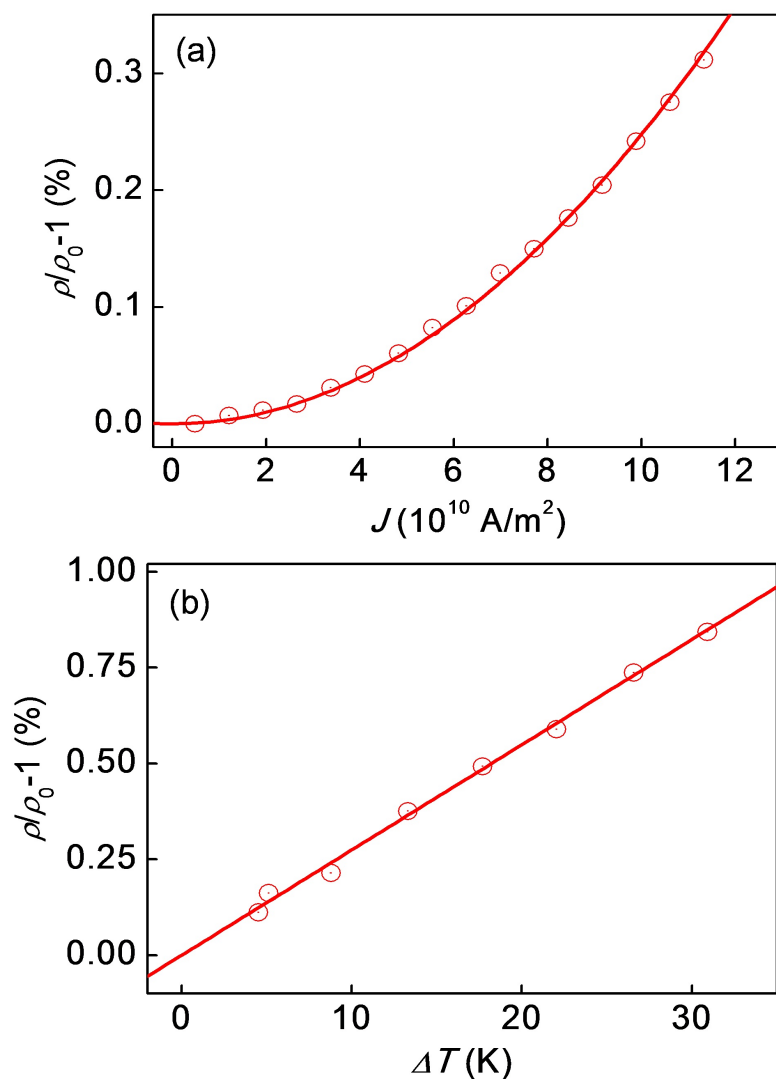


Figure 6.2 (a) Normalized resistivity  $\rho/\rho_0$  with respect to  $J$  for the 5- m-wide wire. The solid line is the best quadratic fit. (b) Normalized resistivity  $\rho/\rho_0$  with respect to the temperature  $\Delta T$  measured in a cryostat. The solid line is the best linear fit.

which is preliminarily measured with respect to the temperature  $T$  in a cryostat as shown by Fig. 6.2(b). Note that the quadratic dependence on  $J$  comes from the Joule-heating effects and the linear dependence on  $T$  generally appears for a small  $\Delta T$ . Combining these two measurements, we estimate the temperature rise as  $\Delta T = (\sigma_J / \sigma_T) J^2$ . In our experiments,  $\sigma_J$  and  $\sigma_T$  are estimated to be  $2.48 \times 10^{-23} \text{ m}^4/\text{A}^2$  and  $2.75 \times 10^{-2} \text{ K}^{-1}$ , respectively.

### 6.1.3 Results & Discussion

From the linear DW motion as exemplified in Fig. 6.1, the DW speed  $v$  can be easily measured as a function of the external magnetic field  $H$ . Note that for this case of the purely field-driven DW motion,  $H^*$  in (1) is identical to  $H$  since there is no STT effect on  $H^*$ . Figure 6.3(a) shows the creep scaling plot of  $v(H)$  with respect to  $(H)^{-1/4}$  for several different temperatures from 297.3 to 327.1 K as denoted in the figure. From the best linear fitting with (1), the creep parameters  $\alpha$  and  $v_0$  can be determined for each temperature. Figures 6.3(b) and (c) show the determined values of  $\alpha$  and  $v_0$ , respectively. Figure 6.3(b) shows that  $\alpha$  is linearly dependent on the temperature in the experimental range. The best fitting with a linear equation  $\alpha = aT + b$  determines the fitting parameters  $a$  and  $b$  as  $-(29.6 \pm 0.8) \times 10^{-23} \text{ JT}^{-3/4}$  and  $(10.6 \pm 0.2) \times 10^{-20} \text{ JT}^{1/4}$ , respectively. Similarly,  $v_0$  also shows a linear dependence as  $\log(v_0) = cT + d$  with the best fitting values  $c = -(6.9 \pm 0.2) \times 10^{-2} \text{ K}^{-1}$  and  $d = (23.8 \pm 0.5)$  in the experimental range. Since  $\alpha$  and  $v_0$  are sizably changed within the experimental range, it is necessary to generalize (6.1) as

$$v = v_0(T) \exp[-\alpha(T) \{H^*\}^{-1/4} / \{k_B T\}], \quad (6.2)$$

by replacing the constants  $\alpha$  and  $v_0$  by the temperature-dependent values  $\alpha(T)$  and  $v_0(T)$ , respectively.

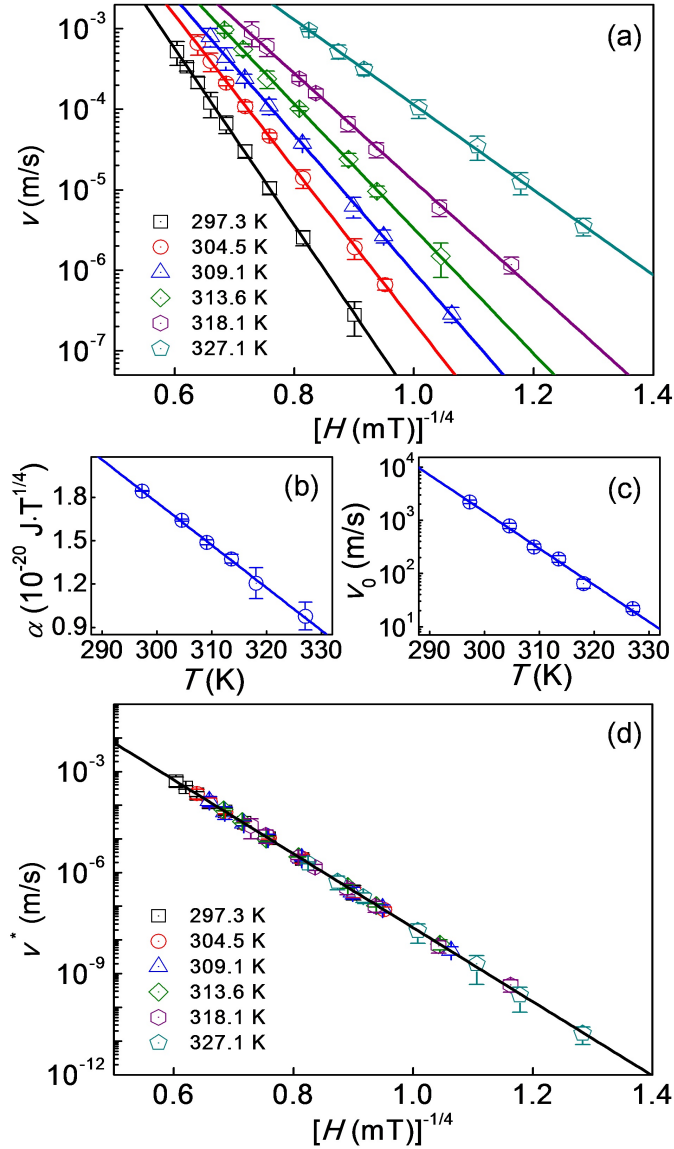


Figure 6.3 (a)  $v$  vs.  $H^{-1/4}$  at different temperatures as denoted in the figure. (b)  $\alpha$  with respect to  $T$ . (c)  $v_0$  with respect to  $T$ . Note that  $\alpha$  and  $v_0$  are obtained by the best linear fit for the data shown in (a) based on (1). (d) with respect to  $H^{-1/4}$ . All at different collapses onto a single universal curve. The solid line shows the best linear fit for all the data.

Now, if we define a virtual DW speed  $v^*$  driven by the same  $H^*$  but at the ambient temperature  $T_0$ , the virtual speed  $v^*$  is then written as

$$v^* = v_0^{RT} \exp[-\alpha_0^{RT} \{H^*\}^{-1/4} / \{k_B T_0\}], \quad (6.3)$$

where,  $v_0^{RT} = v_0(T_0)$  and  $\alpha_0^{RT} = \alpha(T_0)$ . By removing  $H^*$  in (6.3) by using (6.2),  $v^*$  is finally given by

$$v^* = v_0^{RT} \exp[\ln v / [v_0(T)] \{ \alpha_0^{RT} / \alpha(T) \} \{ T / T_0 \}], \quad (6.4)$$

Note that all the parameters in the right side of (6.4) can be experimentally determined. It is also worthwhile to notice that  $v^*$  is the DW speed as if the DW moves at a constant ambient temperature  $T_0$  without any temperature change and thus,  $v^*$  should be solely determined by  $H^*$ . Figure 6.3(d) summarizes the results by plotting  $v^*$  with respect to the  $(H^*)^{-1/4}$ . The figure clearly shows that all the speeds at different temperatures collapse onto a single universal curve, verifying the validity of the present technique to remove all the temperature effects.

To check whether the present technique is applicable to the Joule heating case, we adopt the present technique to the DW motion driven by both the current and field. In the DW creep, the effective field  $H^*$  is given by the function of  $H$  and  $J$  as  $H^* = H - \varepsilon J - \eta J^2 (H - \varepsilon J)^{1/2} + (2/5)\eta^2 J^4 + \dots$ , where  $\varepsilon$  and  $\eta$  are the STT coefficients for the nonadiabatic and adiabatic STTs, respectively [77],[78],[84],[85],[86],[87]. Following the analysis method based on the two-dimensional contour map of  $v^*$  proposed as in [77], the STT coefficients  $\varepsilon$  and  $\eta$  are estimated as  $-(1.3 \pm 0.1) \times 10^{-14} \text{ Tm}^2/\text{A}$  and  $-(2.8 \pm 0.6) \times 10^{-24} \text{ T}^{1/2} \text{m}^4/\text{A}^2$ , respectively. Figure 6.4(a) shows the reconstruction of the universal curve for the case of the DW motion driven by both the current and field for various  $J$  in the range between  $\pm 5.8 \times 10^{10} \text{ A/m}^2$ . It is clear from the figure

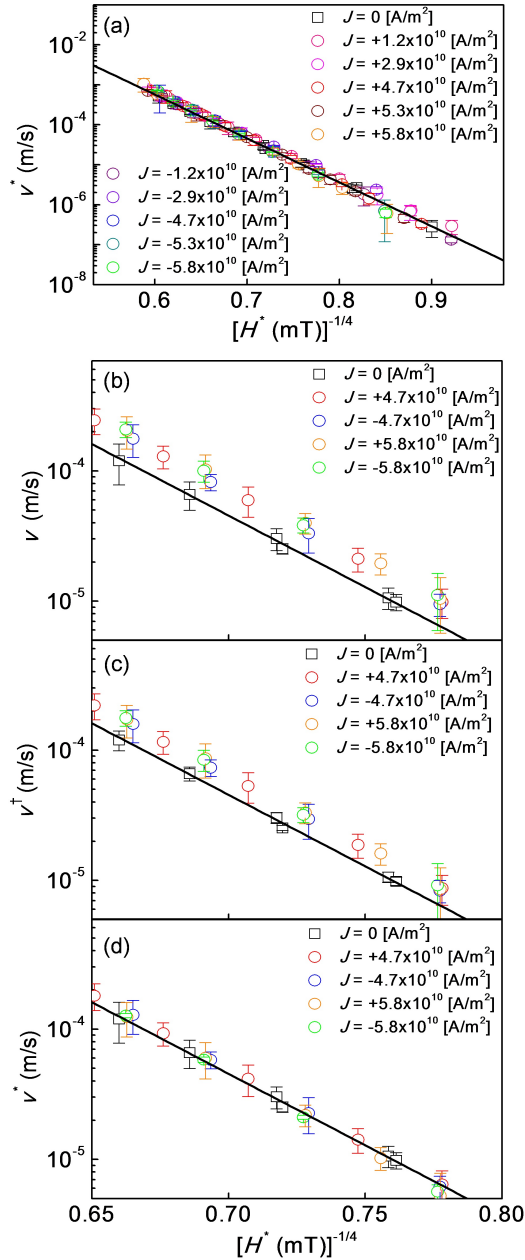


Figure 6.4 (a) Universal curve of the virtual speed  $v^*$  with respect to  $(H^*)^{-1/4}$  at all various  $J$  as denoted in the figure. For comparison, the raw data  $v$  (b), the normalized speed  $v^\dagger$  based on the Arrhenius law (c), and the virtual speed  $v^*$  based on the present method (d) are plotted with respect to  $(H^*)^{-1/4}$ .

that all the DW speeds with different  $J$  (i.e. different Joule-heating effects) collapse onto a single universal curve, which is solely given by the function of  $H^*$ . It thus verifies that the present method is applicable even for the case of the Joule heating. For comparison, the raw data of the measured speed  $v$  and another renormalized speed  $v^\dagger$  used as in [10] are plotted in Figs. 6.4(b) and (c), respectively. Here,  $v^\dagger$  is defined as  $v^\dagger = v_0^{RT} \exp[\ln\{v/(v_0^{RT})\}\{T/T_0\}]$ , where the temperature rise effect only in the  $k_B T$  part is compensated based on the Arrhenius law, by assuming the temperature-independent scaling constants  $\alpha$  and  $v_0$ . Figure 6.4(d) shows the virtual speed  $v^*$  proposed here. It is clearly seen from the figures that the present method provides the best convergence onto the single universal curve.

#### 6.1.4 Conclusions

We propose an experimental technique to compensate the Joule-heating effects on the CIDWM. By measuring the temperature dependence of the creep scaling constants  $v_0(T)$  and  $\alpha(T)$ , the Joule-heating effects can be completely removed in the DW creeping speed, resulting that all DW speeds with different  $J$  (i.e. different temperatures) collapse onto a single universal curve. Based on this method, we demonstrate that the pure STT effects and precise STT efficiencies are determined.

# Chapter 7

## Other Works

-2-Dimensional Feature of the DW Motion Driven by Current and Field (6.2)

-DMI sign and magnitude effect (DMI=0 or DMI=constant) (6.3)

### **7.1 Distinct Universality Classes of Domain Wall Roughness in Two-Dimensional Pt/Co/Pt Films**

We demonstrate here that the current-driven domain wall (DW) forms a facet roughness, distinctive to the conventional self-affine roughness induced by a magnetic field. Despite the different universality classes of those roughness, both the current- and field-driven DW creeping motions belonging to the same universality class, only with different angular dependences. Such angular dependences result in a stable facet angle, from which a single DW image can unambiguously quantify the spin-transfer torque efficiency, an essential parameter in DW-mediated nanodevices.

We studied current-induced domain wall motions (CIDWMs) in two dimensional Pt/Co/Pt films. This two dimensional researches discovered unknown features of CIDWMs. Firstly, the domain wall structure driven by the electric current forms ‘facet’ structure and the structure drastically reduces the domain wall speed converge to zero. This is contrary to the conventional field-driven domain walls which has ‘self-affine’ shape and constant speed. The origin of these differences are an opposite angular dependence of the domain wall motions with respect to the driving forces that result in opposite sign of nonlinear terms in the KPZ (Kadar-Parisi Zhang) equation. Secondly, from the quantitative measurements of the domain wall speed with respect to angles between the current and the domain wall, we found out that the speed of the domain wall motions are determined by the normal component of the current to the domain wall. Through the decomposition of the current, we established the generalized creep equation which includes fields and currents as well as arbitrary domain wall angles. Finally, we found out a new way for determining the efficiency of the current induced force. The angle is obtained when the field and the current respectively drive the domain wall in opposite direction. In order to cancel out two forces, the domain wall should have fixed angle and there is a restoring force to the angle when the domain wall angle deviates from the stable angle. From this stable facet angles, the efficiency of the current induced force is unambiguously determined. We think that all the above findings represent a milestone towards the complete understanding of the STT-induced DW motion.

## 7.2 Determination of Magnetic Domain-Wall Types Using Dzyaloshinskii–Moriya-Interaction-Induced Domain Patterns

In materials with perpendicular magnetic anisotropy, current-induced domain-wall (DW) motion has been received a great attention for technological application towards spintronic devices such as racetrack memory. Very recently, it was found that the Néel-type DW, which is stabilized by the Dzyaloshinskii–Moriya interaction (DMI), maximizes the efficiency of the current-induced DW motion. It is therefore important to get the information about the DW types and the strength of the DMI. Here, we propose an experimental technique to determine DW types (either Néel or Bloch) by analyzing the domain expansion patterns. For this study, Pt/Co/Pt (Sample I), Pt/Co/Pd (Sample II), and Pd/Co/Pd (Sample III) films were deposited on Si/SiO<sub>2</sub> substrates by use of DC-magnetron sputtering. Magnetic domains were then observed by use of magneto-optical Kerr effect microscope. The DW velocity of these three samples with respect to applied in-plane magnetic fields. According to Ref. [27], the shift of the symmetric axis shown in the figures is the direct measure of the DMI-induced effective magnetic field  $H_{DMI}$ . Since Samples I, II, and III exhibits different signs and magnitudes of  $H_{DMI}$  (+85, <-200, and 0 mT, respectively), the DW types of these samples are different with each other: right-handed Néel-type, left-handed Néel-type, and Bloch-type, respectively. Interestingly, these different DW types are closely related with the DW expansion patterns. The figures clearly show that these samples exhibit distinct domain expansion patterns: elongations parallel (Sample I), antiparallel (Sample II), and perpendicular (Sample III) to  $H_x$ , respectively. Therefore, the DW types can be determined by observing the elongation directions of the domain expansion patterns.

# References

- [1] A. Hubert and R. Schafer, *Magnetic Domains* (Springer, Berlin, 1998).
- [2] L. Neel, *J. Phys. Rad.* **15**, 376 (1954).
- [3] P. Bruno and J.-P. Renard, *Appl. Phys. A* **49**, 499 (1989).
- [4] M. Hehn, S. Padovani, K. Ounadjela, and J. P. Bucher, *Phys. Rev. B* **54**, 3428 (1996).
- [5] A. Schulz and K. Baberschke, *Phys. Rev. B* **50**, 13467 (1994).
- [6] T. Trunk, M. Redjda, A. Kakay, M. F. Ruane, and F. B. Humphrey, *J. Appl. Phys.* **89**, 7606 (2001).
- [7] I. Dzyaloshinsky, *J. Phys. Chem. Solids* **4**, 241 (1958).
- [8] T. Moriya, *Phys. Rev. Lett.* **4**, 228 (1960).
- [9] A. Thiaville, S. Rohart, E. Jué, V. Cros, and A. Fert, *Europhys. Lett.* **100**, 57002 (2012).
- [10] S. S. P. Parkin, M. Hayashi, and L. Thomas, *Science* **320**, 190 (2008).
- [11] R. Lavrijsen, J.-H. Lee, A. Fernandez-Pacheco, D. C. M. C. Petit, R. Mansell, and R. P. Cowburn, *Nature* **493**, 647 (2013).

- [12] K.-S. Ryu, L. Thomas, S.-H. Yang, and S. Parkin, *Nat. Nanotechnol.* **8**, 527 (2013).
- [13] S. Emori, U. Bauer, S.-M. Ahn, E. Martinez, and G. S. D. Beach, *Nature Mater.* **12**, 611 (2013).
- [14] I. M. Miron, T. Moore, H. Szambolics, L. D. Buda-Prejbeanu, S. Auffret, B. Rodmacq, S. Pizzini, J. Vogel, M. Bonfim, A. Schuhl, and G. Gaudin, *Nature Mater.* **10**, 419 (2011).
- [15] M. Yamanouchi, D. Chiba, F. Matsukura, T. Dietl, and H. Ohno, *Phys. Rev. Lett.* **96**, 096601 (2006).
- [16] T. Koyama, D. Chiba, K. Ueda, H. Tanigawa, S. Fukami, T. Suzuki, N. Ohshima, N. Ishiwata, Y. Nakatani, and T. Ono, *Appl. Phys. Lett.* **98**, 192509 (2011).
- [17] P. J. Metaxas, J. P. Jamet, A. Mougin, M. Cormier, J. Ferre, V. Baltz, B. Rodmacq, B. Dieny, and R. L. Stamps, *Phys. Rev. Lett.* **99**, 217208 (2007).
- [18] K.-W. Moon, J.-C. Lee, S.-B. Choe, and K.-H. Shin, *Rev. Sci. Instrum.* **80**, 113904 (2009).
- [19] K.-W. Moon, D.-H. Kim, S.-C. Yoo, C.-G. Cho, S. Hwang, B. Kahng, B.-C. Min, K.-H. Shin, and S.-B. Choe, *Phys. Rev. Lett.* **110**, 107203 (2013).
- [20] D.-H. Kim, K.-W. Moon, S.-C. Yoo, B.-C. Min, K.-H. Shin, and S.-B. Choe, *IEEE Trans. Magn.* **49(7)**, 3207 (2013).
- [21] P. Chauve, T. Giamarchi, and P. Le Doussal, *Phys. Rev. B* **62**, 6241 (2000).

- [22] S. Lemerle, J. Ferre, C. Chappert, V. Mathet, T. Giamarchi, and P. Le Doussal, *Phys. Rev. Lett.* **80**, 849 (1998).
- [23] S. Bandiera, R. C. Sousa, B. Rodmacq, and B. Dieny, *IEEE Magn. Lett.* **2**, 3000504 (2011).
- [24] G. A. Bertero and R. Sinclair, *IEEE Trans. Magn.* **31**, 3337 (1995).
- [25] S. Bandiera, R. C. Sousa, B. Rodmacq, and B. Dieny, *Appl. Phys. Lett.* **100**, 142410 (2012).
- [26] R. O’Handley, *Modern Magnetic Materials: Principles and Applications* (Wiley-Interscience, New York, 2000), p. 283.
- [27] S.-G. Je, et al., *Phys. Rev. B* **88**, 214401 (2013).
- [28] M. Vanatka, J.-C. Rojas-Sanchez, J. Vogel, M. Bonfim, A. Thiaville, and S. Pizzini, *J. Phys.: Condens. Matter* **27**, 326002 (2015).
- [29] B. Hillebrands, A. Thiaville, *Spin Dynamics in Confined Magnetic Structures III* (Springer, 2006), p. 207-303.
- [30] D.-H. Kim et al. *Appl. Phys. Lett.* **104**, 142410 (2014).
- [31] E. Jué et al., *ArXiv* 1504.04411 (2015).
- [32] C.A. Akosa, I.M. Miron, G. Gaudin, A. Manchon, *ArXiv:1507.07762v1* (2015).
- [33] S. S. P. Parkin, M. Hayashi, & L. Thomas, *Science* **320**, 190-194 (2008).
- [34] D. A. Allwood et al., *Science* **309**, 1688-1692 (2005).
- [35] D. A. Allwood et al., *Science* **296**, 2003-2006 (2002).

- [36] M. Hayashi, L. Thomas, R. Moriya, C. Rettner, & S. S. P. Parkin, *Science* **320**, 209-211 (2008).
- [37] K.-J. Kim et al., *Appl. Phys. Express* **3**, 083001 (2010).
- [38] A. Thiaville, Y. Nakatani, J. Miltat, & Y. Suzuki, *Europhys. Lett.* **69**, 990-996 (2005).
- [39] J. Kim et al., *Nat. Mater.* **12**, 240-245 (2013).
- [40] Y. Fan et al., *Nat. Mater.* **13**, 699-704 (2014).
- [41] C.-Y. You, I. M. Sung & B.-K. Joe, *Appl. Phys. Lett.* **89**, 222513 (2006).
- [42] K.-W. Moon et al., *Appl. Phys. Express* **4**, 043004 (2011).
- [43] A. Himeno, S. Kasai, & T. Ono, *J. Appl. Phys.* **99**, 08G304 (2006).
- [44] J. H. Franken, H. J.M. Swagten, & B. Koopmans, *Nat. Nanotech.* **7**, 499-503 (2012).
- [45] R. Lavrijsen et al., *Nature* **493**, 647-650 (2013).
- [46] T. C. Chen, & H. Chang, Magnetic bubble memory and logic] *Advances in computer*. Vol. 17 [Yovits, M. C. (ed.) (Academic Press, New York, 1979), p.223-282.
- [47] A. S. Kirakosyan, & V. L. Pokrovsky, *J. Magn. Magn. Mater.* **305**, 413-422 (2006).
- [48] M. Nagao et al., *Nat. Nanotech.* **8**, 325-328 (2013).
- [49] U. K. Rößler, A. N. Bogdanov, & C. Pfleiderer, *Nature* **442**, 797-801 (2006).

- [50] J. Sampaio, V. Cros, S. Rohart, A. Thiaville, & A. Fert, *Nat. Nanotech.* **8**, 839-844 (2013).
- [51] N. Nagaosa, & Y. Tokura, *Nat. Nanotech.* **8**, 899-911 (2013).
- [52] J. Li et al., *Nat. Commun.* **5**, 4704 (2014).
- [53] I. Dzyaloshinsky, *J. Phys. Chem. Solids* **4**, 241-255 (1958).
- [54] T. Moriya, *Phys. Rev.* **120**, 91-98 (1960).
- [55] G. Chen et al., *Phys. Rev. Lett.* **110**, 177204 (2013).
- [56] G. Chen et al., *Nat. Commun.* **4**, 2671 (2013).
- [57] S.-G. Je et al., *Phys. Rev. B* **88**, 214401 (2013).
- [58] A. Hrabec et al., *Phys. Rev. B* **90**, 020402 (2014).
- [59] A. Thiaville, S. Rohart, E. Jué, V. Cros, & A. Fert, *Europhys. Lett.* **100**, 57002 (2012).
- [60] P. J. Metaxas et al., *Phys. Rev. Lett.* **99**, 217208 (2007).
- [61] S. Lemerle et al., *Phys. Rev. Lett.* **80**, 849 (1998).
- [62] J. S. Moodera, L. R. Kinder, T. M. Wong, & R. Meservey, *Phys. Rev. Lett.* **74**, 3273 (1995).
- [63] D.-H. Kim et al., *Appl. Phys. Lett.* **104**, 142410 (2014).
- [64] K.-J. Kim et al., *Nature* **458**, 740-742 (2009).
- [65] S. Emori, U. Bauer, S.-M. Ahn, E. Martinez, & G. S. D. Beach, *Nat. Mater.* **12**, 611-616 (2013).

- [66] K.-W. Moon et al., Phys. Rev. Lett. **110**, 107203 (2013).
- [67] K.-W. Moon et al., Sci. Rep. **5**, 9166; DOI:10.1038/srep09166 (2015).
- [68] S. S. P. Parkin, M. Hayashi, and L. Thomas, Science, **320**, 190 (2008).
- [69] M. Yamanouchi, D. Chiba, F. Matsukura, and H. Ohno, Nature, **428**, 5392 (2004).
- [70] M. Hayashi, L. Thomas, R. Moriya, C. Rettner, and S. P. Parkin, Science, **320**, 209 (2008).
- [71] K.-J. Kim et al., Appl. Phys. Exp. **3**, 083001 (2010).
- [72] H. Tanigawa et al., Appl. Phys. Exp. **1**, 011301 (2008).
- [73] G. Tatara and H. Kohno, Phys. Rev. Lett. **92**, 086601 (2004).
- [74] S. Zhang and Z. Li, Phys. Rev. Lett. **93**, 127204 (2004).
- [75] A. Thiaville, Y. Nakatani, J. Miltat, and Y. Suzuki, Europhys. Lett. **69**, 990 (2005).
- [76] M. Yamanouchi et al., Science, **317**, 1726 (2007).
- [77] J.-C. Lee et al., Phys. Rev. Lett. **107**, 067201 (2011).
- [78] J. Ryu, S.-B. Choe, and H.-W. Lee, Phys. Rev. B, **84**, 075469 (2011).
- [79] M. Yamanouchi, D. Chiba, F. Matsukura, T. Dietl, and H. Ohno, Phys. Rev. Lett., **96**, 096601 (2006).
- [80] A. Yamaguchi et al., Appl. Phys. Lett. **86**, 012511 (2005).
- [81] L. San Emeterio Alvarez et al., Phys. Rev. Lett. **104**, 137205 (2010).

- [82] K.-J. Kim et al., IEEE Trans. Magn. **45**, 3773 (2009).
- [83] K.-J. Kim, J.-C. Lee, S.-B. Choe, and K.-H. Shin, Appl. Phys. Lett. **92**, 192509 (2008).
- [84] O. Boulle et al., Phys. Rev. Lett. **101**, 216601 (2008).
- [85] I. M. Miron et al., Phys. Rev. Lett. **102**, 137202 (2009).
- [86] L. Thomas et al., Nature, **443**, 197 (2006).
- [87] S.-W. Jung, W. Kim, T.-D. Lee, K.-J. Lee, and H.-W. Lee, Appl. Phys. Lett. **92**, 202508 (2008).

# Author's Biography

## Duck-Ho Kim

THz Magnetic Nanodevice LAB. 23-411, Department of Physics & Astronomy, Seoul National University 1 Gwanak-ro, Gwanak-gu, Seoul 08826, Republic of Korea.

Phone: +82-2-884-9254, Fax: +82-2-884-9254,

E-mail (academic): uzes@snu.ac.kr

E-mail (personal): uzes13@gmail.com

## Education

2011 – 2016, Ph. D. - Department of Physics and Astronomy, Seoul National University

2009 – 2011, M. S. - Department of Physics, INHA University

2005 – 2009, B. S. - Department of Physics, INHA University

## Biography

2013.05.12, Collaborative research discussion & Seminar, Department of Applied Physics, Technische Universiteit Eindhoven, 5600 MB Eindhoven, The Netherlands

2013.03.19 – 2013.03.24, Collaborative research discussion & Invited Talk,  
School of Physics and Astronomy, Nottingham of University, University  
Park, Nottingham NG7 2RD, United Kingdom

2010.01.06 – 2010.02.11, JSPS Support Program for Improving Graduate  
School Education, Department of Materials Engineering Science, Osaka  
University, 1-3, Machikaneyama-cho, Toyonaka city, Osaka 560-8531, Japan

# Awards

- [1] 2010.10.22: 2010 한국물리학회 가을학술논문발표회 우수발표상, Dp-III-095 Nano-Oxide층을 포함한 Py/Pd 이중층에서의 Spin-pumping 효과: 김덕호, 김홍현, 유천열(인하대)
- [2] 2010.12.07: 한국자기학회 논문상 (김덕호, 유천열)
- [3] 2011.04.14: 2011년 한국물리학회 봄학술논문발표회 최우수발표상, Dp-II-103 나노 산화층을 포함한 Pd/Ni<sub>81</sub>Fe<sub>19</sub> 이중층에서 스핀 펌핑 효과 억제 : 김덕호, 김홍현, 유천열(인하대학교, 물리학과)
- [4] 2012.12.27: 6th BK (Brain Korea) Young Physicist Workshop 우수포스터상
- [5] 2013.11.01: 2013 한국물리학회 가을학술논문발표회 우수발표상, P4-D168 Pt/Co/Pt 박막에서 이방성 에너지 변화에 따른 자구벽 이동성: 김덕호, 유상철, 문경웅, 김대연, 민병철, 최석봉
- [6] 2014.04.23: 2014 한국물리학회 봄학술논문발표회 우수발표상, P1-D003 Pt/Co/Pt 구조에서 Pt 두께에 따른 Dzyaloshinskii-Moriya Interactions 크기 변화: 김덕호, 제송근, 유상철, 민병철, 이경진, 최석봉
- [7] 2014.05.12: “Maximizing domain-wall speed via magnetic anisotropy adjustment in Pt/Co/Pt films” Appl. Phys. Lett. Editor’s Picks

- [8] 2014.09 – 2014.12: BK (Brain Korea) 21+ Scholarships
- [9] 2015.02.06: 7th BK (Brain Korea) 21+ Young Physicist Workshop 우수포스터상
- [10] 2015.04.23: 2015 한국물리학회 봄학술논문발표회 우수발표상, P3-co.001 비대칭적 자구벽 이동현상을 이용한 거대 Dzyaloshinskii–Moriya 상호작용 측정기: 김덕호, 유상철, 김대연, 민병철, 최석봉
- [11] 2015.04.24: 2015 한국물리학회 봄학술논문발표회 우수발표상, D4-06 나선형 자구벽 기반 2차원 자기 bubblecade 메모리: 김덕호, 문경웅, 유상철, 제송근, 김대연, 전병선, 김원동, 민병철, 황찬용, 최석봉
- [12] 2015.10.22: 2015 한국물리학회 가을학술논문발표회 우수발표상, E1-04 Creep과 Flow 영역에서 Dzyloshinskii-Moriya 상호작용에 의한 Chiral 자구벽 운동의 보편성: 김덕호, 유상철, 김대연, 민병철, 최석봉
- [13] 2015.10.23: 2015 한국물리학회 가을학술논문발표회 우수발표상, G6-05 자기장 각도와 세기 조절을 통한 자기 Bubblecade 속력 최적화: 김덕호, 문경웅, 유상철, 김대연, 민병철, 황찬용, 최석봉

# Publication Lists (SCI & SCIE)

- [1] **Duck-Ho Kim** and Chun-Yeol You, "Enhancement of magneto-optical Kerr signal from the nano-structure by employing anti-reflection coated substrate", J. Magnetism, **13**, 70 (2008).
- [2] **Duck-Ho Kim** and Chun-Yeol You, "Magneto-optical Kerr effect enhancement methods for nanostructure", J. Magnetism, **14**, 31 (2009).
- [3] **Duck-Ho Kim**, Hong-Hyun Kim, and Chun-Yeol You, "Suppression of the spin pumping in Pd/Ni<sub>81</sub>Fe<sub>19</sub> bilayers with nano-oxide layer", Appl. Phys. Lett. **99**, 072502 (2011).
- [4] **Duck-Ho Kim**, Hong-Hyun Kim, Chun-Yeol You, and Hyungsuk Kim, "Optimization of Ferromagnetic Resonance Spectra Measuring Procedure for Accurate Gilbert Damping Parameter in Magnetic Thin Films Using a Vector Network Analyzer", J. of Magnetism **16**, 206 (2011).
- [5] Kyoung-Woong Moon, **Duck-Ho Kim**, Sang-Cheol Yoo, Cheong-Gu Cho, Sungmin Hwang, Byungnam Kahng, Byoung-Chul Min, Kyung-Ho Shin, Sug-Bong Choe, "Distinct Universality Classes of Domain Wall Roughness in Two-Dimensional Pt/Co/Pt Films" Phys. Rev. Lett. **110**, 107203 (2013).

- [6] **Duck-Ho Kim**, Kyoung-Woong Moon, Sang-Cheol Yoo, Byoung-Chul Min, Kyung-Ho Shin, Sug-Bong Choe, “A Method for Compensating Joule-Heating Effect in Current-Induced Domain-Wall Motion” *IEEE Trans. Magn.* **49** (7), 3207 (2013).
- [7] Soong-Geun Je, **Duck-Ho Kim**, Sang-Cheol Yoo, Byoung-Chul Min, Kyung-Jin Lee, and Sug-Bong Choe, “Asymmetric Magnetic Domain-Wall Motion by the Dzyaloshinskii-Moriya Interaction” *Phys. Rev. B* **88**, 214401 (2013).
- [8] **Duck-Ho Kim**, Sang-Cheol Yoo, Dae-Yun Kim, Kyoung-Woong Moon, Soong-Geun Je, Cheong-Gu Cho, Byoung-Chul Min, and Sug-Bong Choe, “Maximizing domain-wall speed via magnetic anisotropy adjustment in Pt/Co/Pt films” *Appl. Phys. Lett.* **104**, 142410 (2014). (*Appl. Phys. Lett. Editor’s Picks*)
- [9] Kyoung-Woong Moon, **Duck-Ho Kim**, Sang-Cheol Yoo, Soong-Geun Je, Byong Sun Chun, Wondong Kim, Byoung-Chul Min, Chanyong Hwang, and Sug-Bong Choe, “Magnetic bubblecade memory based on chiral domain walls” *Sci. Rep.* **5**, 9166 (2015). (**Equally contributed**)
- [10] Dae-Yun Kim, **Duck-Ho Kim**, Joon Moon, and Sug-Bong Choe, “Determination of Magnetic Domain-Wall Types by Dzyaloshinskii-Moriya-Interaction-Induced Domain Patterns” *Appl. Phys. Lett.* **106**, 262403 (2015).
- [11] Kyoung-Woong Moon, **Duck-Ho Kim**, Soong-Geun Je, Byong Sun Chun, Wondong Kim, Z.Q. Qiu, Sug-Bong Choe, and Chanyong Hwang, “Skyrmion Motion Driven by Oscillating Magnetic Field” *Sci. Rep.* **??**, ?? (2015). Accepted

- [12] Dae-Yun Kim, **Duck-Ho Kim**, and Sug-Bong Choe, “Intrinsic Asymmetry in Chiral Domain Walls due to Dzyaloshinskii-Moriya Interaction” *Appl. Phys. Express* ??, ?? (2015). Submit
- [13] **Duck-Ho Kim**, Dae-Yun Kim, Sang-Cheol Yoo, Byoung-Chul Min, and Sug-Bong Choe, “Broken chirality governing asymmetric domain-wall motion in the flow regime” (2015). Preparing the manuscript

# Presentation Lists (International Conferences)

- [1] Chun-Yeol You and **Duck-Ho Kim**, Enhancement of magneto-optical Kerr effect signal from the nano-structure by employing anti-reflection coated substrate, InterMag 2008, AF-07, May 4-8, Madrid, Spain (2008).
- [2] **D.-H. Kim** and C.-Y. You, Magneto-optical Kerr effect Enhancement method for nanodots, Asian Magnetism Conference 2008, AR03, Dec. 10-13, Pusan, Korea (2008).
- [3] **D.-H. Kim**, H.-H. Kim, and C.-Y. You, Spin-Pumping in Py/Pd Bilayers with Nano-Oxide Layer, 2010 ICAUMS, IP14, Dec.8, Jeju, Korea (2010).
- [4] **D.-H. Kim**, H.-H. Kim, and Chun-Yeol You "Spin-pumping in Cu/Py/Pd tri-layers with nano-oxide layer", 2011 InterMag, CO14, Apr. 27, Taipei, Taiwan, (2011).
- [5] N.-H. Kim, **D.-H. Kim**, Chun-Yeol You, "Crystallization and magnetic anisotropy of CoFeB on MgO(001) substrate", 2011 InterMag, FQ12, Apr. 28, Taipei, Taiwan, (2011).
- [6] **D.-H. Kim**, K.-W. Moon, S.-C. Yoo, B.-C. Min, K.-H. Shin, and S.-B. Choe, "A Method for Compensating Joule-Heating Effect in Current-

- Induced Domain-Wall Motion”, 12th Joint MMM/Intermag conference, HP-04, Chicago, Illinois, USA, 18 Jan. (2013).
- [7] S.-C. Yoo, K.-W. Moon, **D.-H. Kim**, K.-H. Shin, B.-C. Min, and S.-B. Choe, “Opposite direction of current-induced domain-wall motion between ferromagnetic Pt/Co/Pt and Pd/Co/Pd thin films”, 12th Joint MMM/Intermag conference, HR-09, Chicago, Illinois, USA, 15 Jan. (2013).
- [8] **D.-H. Kim**, S.-C. Yoo, K.-W. Moon, B.-C. Min, K.-H. Shin, and S.-B. Choe, “Bottom-Pt-Layer Dependence of Domain Wall Mobility in Pt/Co/Pt Films”, The 8th International Symposium on Metallic Multilayers, P-49, Kyoto, Japan, 21 May (2013).
- [9] Kyoung-Woong Moon, **Duck-Ho Kim**, Sang-Cheol Yoo, Cheong-Gu Cho, Sungmin Hwang, Byungnam Kahng, Byoung-Chul Min, Kyung-Ho Shin, and Sug-Bong Choe, “Distinct Universality Classes of Domain Wall Roughness in Two-Dimensional Pt/Co/Pt Films”, 8th International Conference on Magnetic and Superconducting Materials, ??-??, Hammamet, Tunisia, 02, Sep. (2013).
- [10] **Duck-Ho Kim**, Soong-Geun Je, Sang-Cheol Yoo, Byoung-Chul Min, Kyung-Jin Lee, and Sug-Bong Choe, “Opposite Sign of the Dzyaloshinskii-Moriya-Interaction Field between Pt/Co/Pt and Pd/Co/Pd Films” ,58th Annual Conference on MMM, AU-05, Denver, Colorado, USA, 05, Nov. (2013).
- [11] **Duck-Ho Kim**, Sang-Cheol Yoo, Kyoung-Woong Moon, Byoung-Chul Min, and Sug-Bong Choe, “Control of Magnetic Domain Wall Mobility in Pt/Co/Pt systems”, 58th Annual Conference on MMM, FU-16, Denver, Colorado, USA, 07, Nov. (2013).

- [12] Kyoung-Woong Moon, **Duck-Ho Kim**, Sang-Cheol Yoo, Cheong-Gu Cho, Sungmin Hwang, Byungnam Kahng, Byoung-Chul Min, Kyung-Ho Shin, and Sug-Bong Choe, “Distinct Universality Classes of Domain Wall Roughness in Two-Dimensional Pt/Co/Pt Films”, 58th Annual Conference on MMM, FU-15, Denver, Colorado, USA, 07, Nov. (2013).
- [13] Sang-Cheol Yoo, **Duck-Ho Kim**, Byoung-Chul Min, Kyung-Ho Shin, and Sug-Bong Choe, “Control of direction of current-induced domain-wall motion in Pd/Co/Pd by inserting a thin Pt layer at Pd/Co interface”, 58th Annual Conference on MMM, FU-09, Denver, Colorado, USA, 07, Nov. (2013).
- [14] Soong-Geun Je, **Duck-Ho Kim**, Sang-Cheol Yoo, Byoung-Chul Min, Kyung-Jin Lee, and Sug-Bong Choe, “Symmetry Breaking in Field-Driven Domain-Wall Motion by the Dzyaloshinskii-Moriya Interaction”, 58th Annual Conference on MMM, DB-06, Denver, Colorado, USA, 06, Nov. (2013).
- [15] **Duck-Ho Kim**, Sang-Cheol Yoo, Kyoung-Woong Moon, Dae-Yun Kim, Cheong-Gu Cho, Byoung-Chul Min, and Sug-Bong Choe, “Magnetic Domain Wall Mobility Controlled by Anisotropy Energy in Pt/Co/Pt Films”, The 8th International Conference on Advanced Materials and Devices, FRI-SP-P11, Jeju, Korea, 13, Dec. (2013).
- [16] Soong-Geun Je, **Duck-Ho Kim**, Sang-Cheol Yoo, Byoung-Chul Min, Kyung-Jin Lee, and Sug-Bong Choe, “Asymmetry field-driven dynamics with chiral ferromagnetic domain walls”, The 8th International Conference on Advanced Materials and Devices, FRI-SP-P04, Jeju, Korea, 13, Dec. (2013).

- [17] **Duck-Ho Kim**, Soong-Geun Je, Sang-Cheol Yoo, Byoung-Chul Min, Kyung-Jin Lee, and Sug-Bong Choe, “Pt-Layer-Thickness Dependence on the Dzyaloshinskii-Moriya Interactions in Pt/Co/Pt Films”, IEEE International Magnetism Conference 2014, BR-06, Dresden, Germany, 4-8, May (2014).
- [18] Soong-Geun Je, **Duck-Ho Kim**, Sang-Cheol Yoo, Byoung-Chul Min, Kyung-Jin Lee, and Sug-Bong Choe, “Observation of Asymmetric Magnetic Domain-Wall Motion by the Dzyaloshinskii-Moriya Interaction”, The 3rd International Conference of AUMS, No.98, Haikou, China, 29, Oct. (2014).
- [19] **Duck-Ho Kim**, Sang-Cheol Yoo, Dae-Yun Kim, Kyoung-Woong Moon, Soong-Geun Je, Cheong-Gu Cho, Byoung-Chul Min, and Sug-Bong Choe, “Maximizing domain-wall speed via magnetic anisotropy adjustment in Pt/Co/Pt films”, 59th Annual Conference on MMM, GU-04, Honolulu, Hawaii, 3-7, Nov. (2014).
- [20] Dae-Yun Kim, **Duck-Ho Kim**, Joon Moon, Sang-Cheol Yoo, Byoung-Chul Min, and Sug-Bong Choe, “Control of Dzyaloshinskii-Moria interaction by adjusting asymmetric layer structure”, 59th Annual Conference on MMM, GW-09, Honolulu, Hawaii, USA, 3-7, Nov. (2014).
- [21] Sang-Jun Yun, Sang-Cheol Yoo, **Duck-Ho Kim**, Dae-Yun Kim, Hyun-Seok Whang, Byoung-Chul Min, and Sug-Bong Choe, “Correlation between Dzyaloshinskii-Moriya interaction and spin-orbit torques in Pt/Co/Pt wires”, 59th Annual Conference on MMM, GU-08, Honolulu, Hawaii, USA, 3-7, Nov. (2014).

- [22] Soong-Geun Je, Kyoung-Woong Moon, Sang-Cheol Yoo, **Duck-Ho Kim**, Joo-Sung Kim, Joon Moon, Byoung-Chul Min, Chanyong Hwang, and Sug-Bong Choe, “Significant Enhancement of Spin-Transfer Torque in Ultranarrow Domain Walls and Demonstration of Magnetic Bubblecade Memory”, KAUST 2nd International Workshop on SpinOrbit Torques, Thuwal, Saudi Arabia, 26-28, Feb. (2015).
- [23] Kyoung-Woong Moon, **Duck-Ho Kim**, Sang-Cheol Yoo, Soong-Geun Je, Byong Sun Chun, Wondong Kim, Byoung-Chul Min, Chanyong Hwang, and Sug-Bong Choe, “Magnetic Bubblecade Memory”, IEEE International Magnetics Conference, GT-14, Beijing, China, 11-15, May (2015).
- [24] Dae-Yun Kim, **Duck-Ho Kim**, Joon Moon, Sang-Cheol Yoo, Byoung-Chul Min, and Sug-Bong Choe, “Distinct domain-wall expansion patterns due to Dzyaloshinskii-Moriya interaction”, IEEE International Magnetics Conference, ??-??, Beijing, China, 11-15, May (2015).
- [25] **Duck-Ho Kim**, Sang-Cheol Yoo, Dae-Yun Kim, Byoung-Chul Min, and Sug-Bong Choe, “Advanced Dzyaloshinskii-Moriya interaction meter based on angular dependence of asymmetric magnetic domain-wall motion”, 20th International Conference on Magnetism, TH.J-P11, Barcelona, Spain, 05-10, July (2015).
- [26] Kyoung-Woong Moon, **Duck-Ho Kim**, Sang-Cheol Yoo, Soong-Geun Je, Byong Sun Chun, Wondong Kim, Byoung-Chul Min, Chanyong Hwang, and Sug-Bong Choe, “Magnetic Bubblecade Memory Based on Chiral Domain Walls”, 20th International Conference on Magnetism, TH.F-P11, Barcelona, Spain, 05-10, July (2015).

- [27] C. Cho, S. Yun, H. Whang, D. Kim, **Duck-Ho Kim**, J. Moon, S. Je, Y. Oh, and S. Choe, “Enhancement of spin-orbit torque and Dzyaloshinskii-Moriya interaction in Co films sandwiched by various 3d, 4d, and 5d transition metals”, 20th International Conference on Magnetism, TH.F-P11, Barcelona, Spain, 05-10, July (2015).
- [28] Kyoung-Woong Moon, **Duck-Ho Kim**, Sang-Cheol Yoo, Soong-Geun Je, Byong Sun Chun, Wondong Kim, Byoung-Chul Min, Chanyong Hwang, and Sug-Bong Choe, “Skyrmion-like-Magnetic-Bubblecade Memory Based on Chiral Domain Walls”, International Colloquium on Magnetic Films and Surfaces 2015, 0038, Cracow, Poland, 12-17, July (2015).
- [29] **Duck-Ho Kim**, Sang-Cheol Yoo, Dae-Yun Kim, Byoung-Chul Min, and Sug-Bong Choe, “Measuring the Dzyaloshinskii-Moriya interaction based on angular dependence of asymmetric magnetic domain-wall motion”, International Colloquium on Magnetic Films and Surfaces 2015, 0041, Cracow, Poland, 12-17, July (2015).
- [30] **Duck-Ho Kim**, Kyoung-Woong Moon, Sang-Cheol Yoo, Dae-Yun Kim, Byoung-Chul Min, Chanyong Hwang, and Sug-Bong Choe, “Dynamics of Magnetic Bubblecade in Creep Regime”, International Colloquium on Magnetic Films and Surfaces 2015, 0037, Cracow, Poland, 12-17, July (2015).
- [31] **Duck-Ho Kim**, Kyoung-Woong Moon, Sang-Cheol Yoo, Dae-Yun Kim, Byoung-Chul Min, Chanyong Hwang, and Sug-Bong Choe, “Optimization of skyrmion-like magnetic bubblecade speed via strength and angle of magnetic field adjustments”, The 9th International Conference on Advanced Materials and Devices, Po-SP15-005, Jeju, Korea, 07-09, Dec. (2015).

- [32] **Duck-Ho Kim**, Sang-Cheol Yoo, Dae-Yun Kim, Byoung-Chul Min, and Sug-Bong Choe, “Universality of chiral-domain-wall motion by the Dzyloshinskii-Moriya interaction in the creep and flow regimes”, 2016 Joint MMM & Intermag Conference, EC-15, San Diego, California, 11-15, Jan. (2016). oral presentation
- [33] Dae-Yun Kim, **Duck-Ho Kim**, Joon Moon, and Sug-Bong Choe, “Determination of Néel-type domain-walls induced by Dyzaloshinskii Moriya interaction via observation of contrasting domain expansion patterns”, 2016 Joint MMM & Intermag Conference, BV-03, San Diego, California, 11-15, Jan. (2016).

## Presentation Lists (Domestic Conferences)

- [1] 김준서, 김덕호, 유천열, 곽금철, 추가 반사층을 가진 새로운 구조의 초해상 ROM 광디스크에서 재생 신호의 연구, 2007년 정보저장 시스템학회 하계 학술대회, 1-D-3, 연세대학교 8월 30일 (2007).
- [2] 김덕호, 김준서, 최혁철, 유천열, 곽금철, 얇은 박사막 층을 추가한 새로운 구조에서 초해상 ROM 광디스크의 재생 신호 연구, 2007년 추계 한국물리학회, Ep-104, 174 제주 국제컨벤션센터 18-19 Oct. (2007).
- [3] 김덕호, 유천열, 무반사 코팅 기판에 형성된 나노구조에서 MOKE 신호의 증가, 2008년 춘계 한국물리학회, Dp-021, 101, 대전 컨벤션 센터, 17 Apr. (2008).
- [4] 김덕호, 유천열, 무반사 층 기판을 이용한 광자기 Kerr 효과 신호의 증대 기법, F05 2008 한국자기학회 하계학술 연구발표회, 온양관광호텔, 12-14 June (2008).
- [5] 신용확, 김덕호, 유천열, Vector network analyzer를 이용한 Py 박막의 강자성 공명연구, 한국자기학회 동계학술 연구발표회 T07, 덕산스파캐슬, 6-8 Dec. (2009).

- [6] 김덕호, 유천열, 벡터 네트워크 분석기를 이용한 강자성 공명 감도 증가연구, 2010년 춘계 한국물리학회, 대전 컨벤션 센터, Dp-I-012, 21-23 Apr. (2010).
- [7] 김덕호, 유천열, 벡터 네트워크 분석기를 이용한 Py 박막의 강자성 공명 감도 증가 연구, 2010년 한국자기학회 하계 학술 연구발표회, S11, 99, 원주 인터볼고 호텔, 10-12 June (2010).
- [8] 조재훈, 박승영, 조영훈, 윤정범, 김덕호, 유천열, Study of the magnetic properties on Py films by ferromagnetic resonance effect, 2010년 한국자기학회 하계 학술 연구발표회, S16, 108, 원주 인터볼고 호텔, 10-12 June (2010).
- [9] 김덕호, 김홍현, 유천열, "Nano-Oxide층을 포함한 Py/Pd 이중층에서의 Spin-pumping 효과", 2010년 추계 한국물리학회, 보광 휘닉스파크, Dp-III-095, 20-22 Oct. (2010).
- [10] 김덕호, 김홍현, 유천열, "나노 산화층을 포함한 Pd/Ni<sub>81</sub>Fe<sub>19</sub> 이중층에서 스핀 펌핑 효과 억제". 2011 춘계 한국물리학회, 대전 컨벤션 센터, Dp-III-103, 14 Apr. (2011). Best poster award
- [11] 김남희, 김덕호, 유천열, 최경민, 민병철, 신경호, "열 처리된 CoFeB 층의 결정화와 자기이방성에 대한 연구". 2011 춘계 한국물리학회, 대전 컨벤션 센터, Dp-III-090, 14 Apr. (2011).
- [12] 김남희, 김덕호, 유천열, 최경민, 민병철, 신경호, "열처리된 CoFeB 층의 결정화와 자기이방성에 대한 연구", 2011년 한국자기학회 하계 학술 연구발표회, S20, 63, 천안상록리조트, 9~11 June, (2011).
- [13] 김덕호, 문경웅, 유상철, 민병철, 신경호, 최석봉, "온도에 따른 자기장 인가 자구벽 이동의 보편성", 2012년 추계 한국 물리학회, 보광 휘닉스파크, P4-D135, 26 Oct. (2012).

- [14] 김덕호, 문경웅, 유상철, 민병철, 신경호, 최석봉, “전류 인가 자구벽 이동의 줄 효과 보정”, 2012년 하계 한국 자기학회, 보광 휘닉스파크, ST02 30 Nov. (2012).
- [15] 김덕호, 문경웅, 유상철, 민병철, 신경호, 최석봉 “A Method for Compensating Joule-Heating Effect in Current-Induced Domain-Wall Motion”, 6th BK Young Physicists Workshop, 서울대학교 상산수리관, 27 Dec. (2012). Best poster award
- [16] 김덕호, 문경웅, 유상철, 김진욱, 민병철, 신경호, 최석봉 “Pt/Co/Pt 박막의 Pt 두께에 따른 자구벽 이동성”, 2013 춘계 한국물리학회, 대전 컨벤션센터, P2-D057, 25 Apr. (2013).
- [17] 김진욱, 문경웅, 김덕호, 최석봉 “마그논의 스핀 돌림힘 전달에 의한 스핀 파동 인가 자구벽 이동”, 2013 춘계 한국물리학회, 대전 컨벤션센터, P2-D056, 25 Apr. (2013).
- [18] 황현석, 김덕호, 유상철, 민병철, 신경호, 최석봉 “Ta/Pt/Co/Pt 구조에서의 Ta 두께에 따른 광자기 Kerr 효과 증가”, 2013 춘계 한국물리학회, 대전 컨벤션센터, P2-D058, 25 Apr. (2013).
- [19] 김덕호, 유상철, 문경웅, 김진욱, 민병철, 신경호, 최석봉 “Pt/Co/Pt 구조에서 Pt두께에 따른 자구벽 속도 변화”, 2013 하계 한국자기학회, SP-III-4, 안동리첸호텔, 01 June (2013).
- [20] 김덕호, 유상철, 문경웅, 김대연, 민병철, 최석봉 “Pt/Co/Pt 박막에서 이방성 에너지 변화에 따른 자구벽 이동성”, 2013 추계 한국물리학회, P4D168, 창원 컨벤션 센터, 01 Nov. (2013). Best poster award
- [21] Soong-Geun Je, Duck-Ho Kim, Sang-Cheol Yoo, Byoung-Chul Min, Kyung-Jin Lee, Sug-Bong Choe “Detection of Dzyaloshinskii-Moriya Inter-

action and Chiral Domain Wall Dynamics driven by Spin-Orbit Torque”, 2014 춘계 한국물리학회, DF-24, 대전 컨벤션 센터, 25 Apr. (2014). Best presentation award

- [22] 김덕호, 제승근, 유상철, 민병철, 이경진, 최석봉 “Pt/Co/Pt 구조에서 Pt 두께에 따른 Dzyaloshinskii-Moriya Interactions 크기 변화”, 2014 춘계 한국물리학회, P1-D003, 대전 컨벤션 센터, 23 Apr. (2014). Best poster award
- [23] 문준, 조정구, 김덕호, 최석봉 “High Domain Wall Mobility in Pd/Co/Pt Films with thin Pd Layers”, 2014 춘계 한국물리학회, P1-D002, 대전 컨벤션 센터, 23 Apr. (2014).
- [24] 김덕호, 제승근, 유상철, 김대연, 민병철, 이경진, 최석봉 “Pt/Co/Pt 수직 자기이방성 박막에서 위아래 Pt층 두께에 따른 Dzyaloshinskii-Moriya Interactions(DMI) 크기 변화”, 2014 하계 한국자기학회, ST02, 부산 한화리조트 해운대티볼리, 31 May (2014).
- [25] 유상철, 김덕호, 제승근, 민병철, 최석봉 “Pd/Co/PD 박막의 Pd/Co 경계면에 Pt 삽입을 통한 전류인가 자구벽 이동 방향 제어”, 2014 하계 한국자기학회, ST03, 부산 한화리조트 해운대티볼리, 31 May (2014).
- [26] 김덕호, 유상철, 김대연, 문경웅, 제승근, 조정구, 민병철, 최석봉 “Pt/Co/Pt 박막에서 자기 비등방성 에너지 조절을 통한 자구벽 속도 제어”, 2014 하계 한국자기학회, O-IV-3, 부산 한화리조트 해운대티볼리, 30 May (2014).
- [27] 제승근, 김덕호, 유상철, 김주성, 민병철, 이경진, 최석봉 “DMI 측정법: DMI에 의한 비대칭적 자구벽 운동 및 스핀-오비탈 토크에 의한 자구벽 운동”, 2014 하계 한국자기학회, O-IV-6, 부산 한화리조트 해운대티볼리, 30 May (2014).

- [28] 김덕호, 유상철, 김대연, 문경웅, 제승근, 조정구, 민병철, 최석봉 “Pt/Co/Pt 박막에서 자기 비등방성 에너지 조절을 통한 자구벽 속력 최대화”, 2014 추계 한국물리학회, P3-E066, 광주 김대중컨벤션센터, 23, Oct. (2014).
- [29] 문경웅, 김덕호, 제승근, 유상철, 전병선, 김원동, 민병철, QIU Z. Q., 최석봉, 황찬용 “비대칭적 자구벽이동현상을 이용한 2차원 메리소자 구현”, 2014 추계 한국물리학회, EF-16, 광주 김대중컨벤션센터 24, Oct. (2014).
- [30] 문경웅, 김덕호, 유상철, 제승근, 전병선, 김원동, 민병철, 최석봉, 황찬용 “Unidirectional motion of bubble domains in magnetic film”, 2014 하계 한국자기학회, O-III-3, 무주군 덕유산무주리조트 28, Nov. (2014).
- [31] 김덕호, 유상철, 김대연, 문경웅, 제승근, 조정구, 민병철, 최석봉 “Maximizing domain-wall speed via magnetic anisotropy adjustment in Pt/Co/Pt films”, 7th BK21+ Young Physicists, YPW 07-PS9, 서울대학교 56동, 06, Feb. (2015). Best poster award
- [32] 김대연, 김덕호, 문준, 최석봉 “Determination of domain-wall configuration by observing domain pattern”, 7th BK21+ Young Physicists, YPW 07-PS7, 서울대학교 56동, 06, Feb. (2015). Best poster award
- [33] 김덕호, 문경웅, 유상철, 제승근, 김대연, 전병선, 김원동, 민병철, 황찬용, 최석봉 “나선형 자구벽 기반 2차원 자기 bubblecade 메모리”, 2015 춘계 한국물리학회, D4-06, 대전 컨벤션센터 24, Apr. (2015). Best presentation award
- [34] 김덕호, 유상철, 김대연, 민병철, 최석봉 “비대칭적 자구벽 이동현상을 이용한 거대 Dzyaloshinskii–Moriya 상호작용 측정기”, 2015 춘계 한국물리학회, P3-co.001, 대전 컨벤션센터 23, Apr. (2015). Best poster award

- [35] 김대연, **김덕호**, 문준, 최석봉 “Distinct magnetic-domain-pattern induced by Dzyaloshinskii-Moriya interaction”, 2015 춘계 한국물리학회, P3-co.004, 대전 컨벤션센터 23, Apr. (2015).
- [36] 조정구, 김대연, 황현석, 윤상준, **김덕호**, 제승근, 문준, 최석봉, 오영완, 박병국 “3d, 4d, 5d 전이금속을 이용한 Co 수직 자성 초박막의 스핀궤도 돌림힘과 Dzyaloshinskii-Moriya 상호작용”, 2015 춘계 한국물리학회, A7.03, 대전 컨벤션센터 22, Apr. (2015).
- [37] 문경웅, **김덕호**, 제승근, 전병선, 김원동, 최석봉, 황찬용 “교류자기장에 의한 스커미온 이동 특성연구”, 2015 하계 한국자기학회, O-I-2, 부산 한화리조트 해운대티볼리 28, May (2015).
- [38] 김대연, **김덕호**, 문준, 최석봉 “자구벽 확장 패턴 분석을 통한 자구벽 형태 결정”, 2015 하계 한국자기학회, SS02, 부산 한화리조트 해운대티볼리 28, May (2015).
- [39] 조정구, 황현석, 김대연, 윤상준, **김덕호**, 문준, 제승근, 최석봉, 오영완, 박병국 “3d, 4d, 5d 전이금속을 이용한 Co 수직 자성 초박막의 스핀궤도 돌림힘과 Dzyaloshinskii-Moriya 상호작용”, 2015 하계 한국자기학회, SS02, 부산 한화리조트 해운대티볼리 28, May (2015).
- [40] **김덕호**, 김대연, 유상철, 민병철, 최석봉 “Creep과 Flow 영역에서 Dzyaloshinskii-Moriya 상호작용에 의한 Chiral 자구벽 운동의 보편성”, 2015 추계 한국물리학회, E1.04, 경주 화백 컨벤션 센터 22, Oct. (2015). Best presentation award
- [41] **김덕호**, 문경웅, 유상철, 김대연, 민병철, 황찬용, 최석봉 “자기장 각도와 세기 조절을 통한 자기 Bubblecade 속력 최적화”, 2015 추계 한국물리학회, C6.05 경주 화백 컨벤션 센터 23, Oct. (2015). Best presentation award

- [42] 김대연, **김덕호**, 문준, 최석봉 “비대칭 자구 확장 패턴 분석을 통한 자구벽 형태 결정”, 2015 추계 한국물리학회”, 2015 추계 한국물리학회, E1.02, 경주 화백 컨벤션 센터 22, Oct. (2015).
- [43] Sug-Bong Choe, Soong-Geun Je, Kyoung-Woong Moon, Sang-Cheol Yoo, **Duck-Ho Kim**, Joo-Sung Kim, Joon Moon, Byoung-Chul Min, Chanyong Hwang “Huge negative spin-transfer torque in atomically thin Co layers and demonstration of magnetic Bubblecade memory” 2015 추계 한국물리학회, C5.03, 경주 화백 컨벤션 센터 22, Oct. (2015).

## 초록

차세대 메모리 소자에 응용 가능성으로 자구벽 운동에 대한 연구가 널리 수행되어 왔다. 자구벽은 자기장 혹은 전류로 구동을 시켜 여러가지 형태의 메모리가 제안되었는데, 그 중 racetrack memory가 가장 활발하게 연구되어 왔다. 메모리 소자로서 구현하기 위해서는 적은 구동힘으로 자구벽을 이동시키는 것이 중요하다. 최근 chiral 구조를 가진 자구벽에서 구동힘이 전류일 때 높은 효율을 가져 높은 자구벽 운동이 보고되었다. 이에따라 chiral 구조의 자구벽 운동에 대한 심도 깊은 이해가 필요하다.

본 논문은 크게 4가지 연구를 수행하였다. 첫째 시료의 구조적인 특성을 변화시켜 자구벽 운동을 최적화 시키는 연구를 수행하였다. 자구벽운동에 가장 큰 역할을 하는 층은 자성층으로, 기존 연구에서는 자성층이 얇을 때 높은 속력을 가진다는 것이 보고되었다. 본 연구에서는 자성 성질을 가지는 가장 얇은 자성층 두께에서 인접한 금속물질(Pt) 두께를 바꿔가며 자구벽 속력의 변화를 조사해 보았다. 이 연구에서, 아래층 Pt이 얇을 수록 위쪽 Pt층이 두꺼울 수록 자구벽이 빠른 속력으로 움직이는 것을 관찰하였다. 이 현상을 광자기 Kerr 현미경을 이용해 관찰하였고, 원인을 파악하기 위해, 자기성질을 측정하여 자기 이방성 에너지와 자구벽 속력 사이에 상관 관계가 있음을 발견하였다. 이 현상은 creep 이론을 이용하여 두 물리량 사이에 관계식을 얻어, 실험으로 관찰한 현상을 설명할 수 있었다. 이 연구를 통해 자구벽 속력을 최적화 시킬 수 있는 방법을 제공하였고, 관련 현상을 이론적으로도 잘 이해할 수 있었다.

두번째 연구는 chiral구조 자구벽 운동에 대한 연구를 수행하였다. chiral 구조 자구벽은 전류인가 자구벽 운동에서 매우 중요한 역할을 하는데, 특히 수직 자기 이방성 물질에서 Dzyaloshinskii-Moriya (DM) 상호작용이 이런 구조를 만드는데 중요한 역할을 한다. DM상호작용과 관련된 자기장 인가 자구벽운동은 기존에

Creep영역에서 활발히 연구되었다. 이러한 연구로 자구벽 운동에 DM상호작용으로 비대칭 자구벽 운동이 일어남을 잘 이해할 수 있었다. 그러나 최근 chiral damping이라는 새로운 이론적인 모델로 비대칭적 자구벽 운동이 발생할 수 있음이 제안되었다. 본 연구에서는 chiral damping이 일어나지 않는 flow영역에서 비대칭적 자구벽 운동을 관찰하였다. 이 영역에서도 수평방향의 자기장에 따라 (수직방향 자기장은 고정: 구동힘은 고정) 자구벽 속력이 달라졌는데, 이런 현상은 기존에 제안된 방법으로 설명이 되지 않았다. 본 연구에서는 1차원 자구벽 모델을 이용하여 해석적인 식을 유도, 이를 통해 관련 현상을 정성적으로 이해할 수 있었다. 특히 이런 모델에서 자구벽 속력의 최소 지점이 DM상호작용에 의한 자기장 값을 나타내어 실험적으로 속력 최소값을 잘 설명하고, DM상호작용 값을 측정하는 모델을 제시하였다.

세번째 연구는 DM상호작용에 대한 새로운 측정법을 제시하였다. 기존 연구에서는 DM상호작용을 측정하기 위해서는 수평방향 자기장크기에 따라 자구벽 속력을 측정한 다음, 최저속력 지점에 해당하는 자기장 값으로 DM상호작용을 측정하였다. 그러나 이 방법은 DM상호작용 크기가 측정 자기장 범위보다 큰 경우, 즉 측정범위 안에서 최저 속력이 관찰이 되지 않으면 사용 할 수 없었다. 본 연구에서는 자구벽 각도를 바꿔가며, 각각의 각도에서 수평방향 자기장 크기에 따른 자구벽 속력을 관찰하였다. 관찰한 결과 최저 속력에 해당되는 수평 자기장 값이 자구벽 각도가 바뀔에 따라 변함을 확인하였다. 놀라운점은 둘 사이의 관계가 cosine함수 형태로 바뀔을 확인 할 수 있었다. 이런 현상은 DM상호작용에 의한 자기장은 자구벽에 수직으로 작용하는데, 자구벽 각도가 달라지게 되면 수평 자기장 방향으로 작용하는 DM상호작용에 의한 유효 자기장 성분값이 계속 다르게 작용하기 때문에 일어나는 것이다. 이러한 결과를 이용하여 큰 자구벽 각도에서 DM상호작용에 의한 자기장값이 측정 범위보다 큰 경우에도 측정할 수 있었다. 이러한 방법은 기존 DM상호작용 측정기의 한계를 극복하여, 더 큰 값을 측정하는 방법으로 유용하게 이용될 수 있었다.

마지막으로 chiral 자구벽을 이용하여 새로운 메모리 소자를 구현하였다. 기

존에 자구벽을 구동하기 위한 방법으로 전류를 많이 사용하였는데, 이런 방법은 전류 인가시 시료의 온도 증가가 발생하고, 공정작업이 수반되어 연구를 하는데 많은 어려움이 있다. 본 연구는 기울인 자기장을 교류로 인가하게 되면 자구벽이 이동하는 새로운 현상을 제안하고, 현상을 관찰하여 보고하였다. 특히 임의의 구조의 원형 자구 배열을 만들어 수 mm까지 잘 이동함을 실험적으로 보여주었고, 4비트 메모리 소자도 구현하였다. 이러한 새로운 메모리를 자기 Bubblecade라 명명하였다.

본 연구들을 통해 자기장 인가 자구벽 운동에 대한 물리적인 이해를 높일 수 있었고, 관련 현상은 DM상호작용 chiral 자구벽 운동에 많은 도움이 될 것으로 생각이 된다. 특히 이러한 연구는 차세대 메모리 소자를 구현하는데 많은 도움이 될 것이다.

**주요어:** Domain Wall, Dzyaloshinskii-Moriya Interaction, Flow regime, Creep regime, Magneto-Optical Kerr Effect Microscope

**학번:** 2011-30121